Copyright Warning & Restrictions

The copyright law of the United States (Title 17, United States Code) governs the making of photocopies or other reproductions of copyrighted material.

Under certain conditions specified in the law, libraries and archives are authorized to furnish a photocopy or other reproduction. One of these specified conditions is that the photocopy or reproduction is not to be "used for any purpose other than private study, scholarship, or research." If a, user makes a request for, or later uses, a photocopy or reproduction for purposes in excess of "fair use" that user may be liable for copyright infringement,

This institution reserves the right to refuse to accept a copying order if, in its judgment, fulfillment of the order would involve violation of copyright law.

Please Note: The author retains the copyright while the New Jersey Institute of Technology reserves the right to distribute this thesis or dissertation

Printing note: If you do not wish to print this page, then select "Pages from: first page # to: last page #" on the print dialog screen

NJIT
New Jersey's Science & Technology University

The Van Houten library has removed some of the personal information and all signatures from the approval page and biographical sketches of theses and dissertations in order to protect the identity of NJIT graduates and faculty.

ABSTRACT

CANTILEVER BEAM MICROACTUATORS WITH ELECTROTHERMAL AND ELECTROSTATIC DRIVE

by
Murat M. Okyar

Microfabrication provides a powerful tool for batch processing and miniaturization of mechanical systems into dimensional domain not accessible easily by conventional machining. CMOS IC process compatible design is definitely a big plus because of tremendous know-how in IC technologies, commercially available standard IC processes for a reasonable price, and future integration of micromachined mechanical systems and integrated circuits. Magnetically, electrostatically and thermally driven microactuators have been reported previously. These actuators have applications in many fields from optics to robotics and biomedical engineering.

At NJIT cleanroom, mono or multimorph microactuators have been fabricated using CMOS compatible process. In design and fabrication of these microactuators, internal stress due to thermal expansion coefficient mismatch and residual stress have been considered, and the microactuators are driven with electro-thermal power combined with electrostatical excitation. They can provide large force, and in- or out-of-plane actuation. In this work, an analytical model is proposed to describe the thermal actuation of in-plane (inchworm) actuators. Stress gradient throughout the thickness of monomorph layers is modeled as linearly temperature dependent $\Delta\sigma$. The nonlinear behaviour of out-of-plane actuators under electrothermal and electrostatic excitations is investigated. The analytical results are compared with the numerical results based on Finite Element Analysis. ANSYS, a general purpose FEM package, and IntelliCAD, a FEA CAD tool specifically designed for MEMS have been used extensively. The experimental results accompany each analytical and numerical work.

Micromechanical world is three dimensional and 2D world of IC processes sets a limit to it. A new micromachining technology, *reshaping*, has been introduced to realize 3D structures and actuators. This new 3D fabrication technology makes use of the advantages of IC fabrication technologies and combines them with the third dimension of the mechanical world. Polycrystalline silicon microactuators have been reshaped by Joule heating. The first systematic investigation of reshaping has been presented. A micromirror utilizing two reshaped actuators have been designed, fabricated and characterized.

Blank Page

CANTILEVER BEAM MICROACTUATORS WITH ELECTROTHERMAL AND ELECTROSTATIC DRIVE

by
Murat M. Okyar

A Dissertation
Submitted to the Faculty of
New Jersey Institute of Technology
in Partial Fulfillment of the Requirements for the Degree of
Doctor of Philosophy

Department of Electrical and Computer Engineering

January 1998

Copyright © 1998 by Murat M. Okyar

ALL RIGHTS RESERVED

APPROVAL PAGE

CANTILEVER BEAM MICROACTUATORS WITH ELECTROTHERMAL AND ELECTROSTATIC DRIVE

Murat M. Okyar

Dr. William N. Carr, Dissertation Advisor — Date
Professor of Electrical and Computer Engineering, NJIT

Dr. Edip Niver, Committee Member — Date
Associate Professor of Electrical and Computer Engineering , NJIT

Dr. Robert B. Marcus, Committee Member — Date
Professor of Electrical and Computer Engineering, NJIT

Dr. Kenneth R. Farmer, Committee Member — Date
Associate Professor of Physics, NJIT

Dr. Hakan Ozdemir, Committee Member — Date
Member of Technical Staff, SGS Thomson, San Jose, CA

BIOGRAPHICAL SKETCH

Author: Murat M. Okyar

Degree: Doctor of Philosophy

Date: January 1998

Undergraduate and Graduate Education:

- Doctor of Philosophy in Electrical Engineering,
  New Jersey Institute of Technology, Newark, NJ, 1998
- Master of Science in Electronics and Telecommunications Engineering,
  Istanbul Technical University, Istanbul, Turkey, 1994
- Bachelor of Science in Electronics and Telecommunications Engineering,
  Istanbul Technical University, Istanbul, Turkey, 1992

Major: Electrical Engineering

Presentations and Publications:

Murat Okyar, Xi-Qing Sun, William N. Carr
"Thermally excited inchworm actuators and stepwise micromotors: Analysis and fabrication," presented at *SPIE Micromachining and Microfabrication*, Austin TX, Sep 1997. Published in Proc. SPIE vol. 3224 pp. 372-279.

Murat Okyar, Xi-Qing Sun, William N. Carr
"Electrostatic and thermal control of a micromirror: Simulation and fabrication," submitted to International Conference on Modeling and Simulation of Microsystems, Semiconductors, Sensors and Actuators (MSM98).

Murat Okyar, Xi-Qing Sun, William N. Carr
"Reshaping as a 3D actuator fabrication technique" to be submitted to Solid-State Sensor and Actuator Workshop, Hilton Head 98.

Murat Okyar, Xi-Qing Sun, William N. Carr
"Reshaping of polycrystalline structures with in-situ rapid thermal processing" to be submitted to Journal of Micromechanics and Microengineering.

Murat Okyar, Xi-Qing Sun, William N. Carr
"Cantilever beam actuators using thermal and electrostatic excitation: Modeling vs. experiment" to be submitted to Journal of Micromechanics and Microengineering.

TABLE OF CONTENTS

Chapter | Page

1 INTRODUCTION 1

1.1 Background Information 2

1.1.1 Microactuators 2

1.1.2 Micromirrors 4

1.2 Objective of this Research 5

1.3 Organization of this Dissertation 7

2 MECHANICAL PROPERTIES OF THIN-FILMS AND STRESS 9

2.1 Strength of Materials 10

2.1.1 Stress and Strain 10

2.1.2 Elastic Deformation and Hooke's Law 12

2.2 Stress in Thin Films 14

2.3 Origin of Stress in Thin Films 16

2.4 Stress Gradient in Monomorph Films 18

2.5 Process-Dependent Residual Stress 22

2.5.1 Silicon Nitride 22

2.5.2 Polysilicon 24

2.6 Stress Measurement Techniques 24

3 INCHWORM (IN-PLANE) ACTUATOR 28

3.1 Device Description 29

3.2 Analytical Model 33

3.2.1 1D Cantilever Beam 33

3.2.2 Validity of the Analytical Model 36

3.3 Finite Element Modeling of the In-Plane Actuator 39

3.3.1 Solid Model and Boundary Conditions 39

TABLE OF CONTENTS
(Continued)

Chapter | Page

3.3.2 Simulation Results 40

3.4 Two-segment Bimorph Structure 46

4 OUT-OF-PLANE ACTUATOR 62

4.1 Thermal Design 62

4.2 Electromechanical Design 68

4.3 Application 71

5 RESHAPING AS A NEW MICROMACHINING AND SELF-ASSEMBLY TOOL 82

5.1 Fabrication 83

5.2 Recrystallization of Polysilicon and Grain Growth 83

5.3 Reshaping Process 86

5.3.1 Description of the Reshaping Process 86

5.3.2 Experimental Results 87

5.4 Application: Reshaped Micromirror 108

5.5 A Proposed System Application: Microscanner for Barcode Readers . 122

6 SUMMARY AND CONCLUSION 125

APPENDIX A NEWTON-RAPHSON PROCEDURE 127

APPENDIX B PROCESS STEPS OF MICROSTRUCTURES DISCUSSED IN THIS THESIS 133

APPENDIX C MATLAB CODE FOR ELECTROMECHANICAL CALCULATIONS OF PULL-IN VOLTAGE FOR OUT-OF-PLANE ACTUATOR USING NEWTON-RAPHSON METHOD 136

APPENDIX D NUMERICAL MODELING AND SIMULATION OF MEMS 143

REFERENCES 146

LIST OF TABLES

Table **Page**

3.1 Thin film dimensions and stress properties 35

3.2 Material Properties of candidate materials for two-segment actuator . . . 49

3.3 Material information, dimensions of the simulated two-segment bimorph cases. 49

3.4 Simulation results for the two-segment cantilever beam. 53

3.5 Simulation results of the two-segment full actuator structure. 53

3.6 Simulated modal frequency values. (l_1=l_2=430μm) 54

4.1 Dimensions and properties of the analyzed out-of-plane actuator 67

5.1 Three sets of samples used for investigation of the reshaping process. . . . 94

5.2 The simulated modal frequencies of the reshaped micromirror. 121

LIST OF FIGURES

Figure		Page
2.1	(a) Tensile force applied to plate. (b) Arbitrary free-body section revealing spatial distribution of stress through plate. Both tensile and shear stresses exist on exposed plane. (c) Distortion in plate due to applied shear stress.	12
2.2	Load-Deformation curve	13
2.3	Sequence of events leading to (a) residual tensile stress in film; (b) residual compressive stress in film	15
2.4	Stress analysis of film-substrate combination: (a) composite structure; (b) free-body diagrams of film and substrate with indicated interfacial forces and end moments; (c) elastic bending of beam under applied end moment.	17
2.5	Schematic of released monomorph beams with internal stress (a) uniform internal stress, (b) positive stress gradient throughout the thickness, (c) negative stress gradient throughout the thickness.	19
2.6	A structural member with the coordinate system.	19
2.7	Cross-sectional TEM micrograph of columnar grains grown out of a transition layer of small grains at the SiO_2 interface.	20
2.8	Calculation of the displacement from the circle with a radius r.	22
2.9	Calculated shape of a polysilicon cantilever with a stress gradient (1.7 MPa/μm) throughout the thickness. The beam was divided into 100 small elements for the following numerical pull-in calculations discussed in Section 4.3. (Dimensions 1 mm X 30 μm X 1.5 μm)	23
2.10	Layered solid model for FEA. Stress gradient throughout the thickness is modeled with thermal expansion gradient ($\alpha_1 \neq \alpha_2 \neq \alpha_3 ...$).	23
2.11	Schematic diagram of two-laser film stress measurement technique.	26
2.12	Schematic diagram of circular-plate film stress measurement technique.	27
3.1	AFIT's thermal actuator.	29
3.2	A schematic view of up-bowed actuator	30
3.3	Actuation sequence illustration	31
3.4	Schematic view: (a) top, (b) side.	32

LIST OF FIGURES
(Continued)

Figure		Page
3.5	1D Cantilever beam model.	34
3.6	Cross-section of the bimorph cantilever beam.	34
3.7	The 2D shape of the up-bowed actuator at room temperature constructed from the analytical model (dimensions are in micron).	37
3.8	The 3D shape of the up-bowed actuator at room temperature constructed from the analytical model	38
3.9	Solid model of the inchworm actuator, meshed and with displacement boundary conditions applied.	41
3.10	The questionable result set of linear FEA analysis	42
3.11	The displacement in horizontal direction throughout the cantilever at room temperature	43
3.12	The displacement in vertical direction throughout the cantilever at room temperature.	44
3.13	Tip displacement of the inchworm actuator vs. normalized temperature: Calculated and FEA results.	45
3.14	SEM picture of the up-bowed actuator.	46
3.15	Measured lateral tip displacement as a function of input power for thermal actuation without electrostatic excitation (V_b)	47
3.16	The calculated horizontal and vertical force at the tip of the actuator as a function of temperature . When temperature increases, the actuator flattens out and the tip moves forward. (T_o=625°)	50
3.17	Two-segment bimorph actuator: (a) Before sacrificial layer release, (b) After sacrificial layer release	51
3.18	Solid model of the two-segment actuator with the mesh and displacement boundary conditions.	52
3.19	Simulation results of the two segment bimorph cantilever beam: Case # 1.	54
3.20	Simulation results of the two segment bimorph cantilever beam: Case # 2.	55

LIST OF FIGURES
(Continued)

Figure **Page**

3.5 1D Cantilever beam model. 34

3.6 Cross-section of the bimorph cantilever beam. 34

3.7 The 2D shape of the up-bowed actuator at room temperature constructed from the analytical model (dimensions are in micron). 37

3.8 The 3D shape of the up-bowed actuator at room temperature constructed from the analytical model 38

3.9 Solid model of the inchworm actuator, meshed and with displacement boundary conditions applied. 41

3.10 The questionable result set of linear FEA analysis 42

3.11 The displacement in horizontal direction throughout the cantilever at room temperature 43

3.12 The displacement in vertical direction throughout the cantilever at room temperature. 44

3.13 Tip displacement of the inchworm actuator vs. normalized temperature: Calculated and FEA results. 45

3.14 SEM picture of the up-bowed actuator. 46

3.15 Measured lateral tip displacement as a function of input power for thermal actuation without electrostatic excitation (V_b) 47

3.16 The calculated horizontal and vertical force at the tip of the actuator as a function of temperature . When temperature increases, the actuator flattens out and the tip moves forward. (T_o=625°) 50

3.17 Two-segment bimorph actuator: (a) Before sacrificial layer release, (b) After sacrificial layer release 51

3.18 Solid model of the two-segment actuator with the mesh and displacement boundary conditions. 52

3.19 Simulation results of the two segment bimorph cantilever beam: Case # 1. . 54

3.20 Simulation results of the two segment bimorph cantilever beam: Case # 2. . 55

LIST OF FIGURES
(Continued)

Figure **Page**

3.21 Simulation results of the two segment bimorph cantilever beam: Case # 3. . 56

3.22 Simulation results of the two segment bimorph actuator: Case # 1. 57

3.23 Simulation results of the two segment bimorph actuator: Case # 2. 58

3.24 Simulation results of the two segment bimorph actuator: Case # 3. 59

3.25 The deformed shape of the two-segment bimorph actuator at the first modal frequency (l_1=l_2) 60

3.26 The deformed shape of the two-segment bimorph actuator at the first modal frequency (l_1=l_2) 61

4.1 (a) Schematic of the bimetallic cantilever, (b) forces and moments acting on the cross-sections of a segment along the length of the composite beam 63

4.2 Released, bimorph, out-of-plane actuator. 64

4.3 The bimorph, out-of-plane actuator can be driven thermally and/or electrostatically 65

4.4 Loading of the cantilever beam and its 1D lumped model. 66

4.5 Tip displacement of the bimorph cantilever vs. temperature. 67

4.6 Calculated deformed shape of the out-of-plane actuator at room temperature.. 69

4.7 3D shape of the out-of-plane actuator reconstructed from the vertical and horizontal displacement data. 70

4.12 (a) 1D lumped parallel plate capacitor model (b) Visualization of the 2D problem. 70

4.13 Pull-in voltage vs. vertical tip position of the $TaSi_2$-LTO out-of-plane actuator. 72

4.14 Layout of the micromirror designed using Mentor Graphics; LTO (blue) and $TaSi_2$ heater (pink) mask. 74

LIST OF FIGURES
(Continued)

Figure		Page
4.15	Schematic view of the bimorph actuator, (a) top, (b) cross-section.	75
4.16	Schematic view of the micromirror with combined thermal and electrostatic drive.	75
4.17	Released micromirror actuated by two out-of-plane actuators.	76
4.18	Meshed solid model of the micromirror (IntelliCAD).	77
4.19	Simulated vertical tip displacement vs. temperature difference (without electrostatic drive).	78
4.20	Simulated vertical tip displacement vs. temperature difference for the out-of-plane actuator (with V_b=30V).	79
4.21	Measured tip displacement vs. thermal input power without electrostatic drive.	80
4.22	Measured tip displacement vs. thermal input power for the out-of-plane actuator with electrostatic drive (V_b=30).	81
5.1	Setup for reshaping process	84
5.2	Plastically deformed and modified regions of the reshaped arm.	85
5.3	Reshaping with a special probe.	87
5.4	Fabricating dimple as a base to make an ohmic contact with the tip.	88
5.5	An alternative reshaping setup.	89
5.6	Setup for three-dimensional reshaping with many probes.	89
5.7	Released actuators and mirror platform before reshaping.	90
5.8	The edge of the mirror platform was lifted ~350μm before applying thermal power.	90
5.9	Laser-Photodiode setup to measure micromirror deflection	91
5.10	Actuators and mirror platform reshaped at 45°.	92

LIST OF FIGURES
(Continued)

Figure **Page**

5.11 Actuators and mirror platform reshaped at 90° 92

5.12 Actuators and mirror platform reshaped at 120° 93

5.13 SEM photograph of a micromirror reshaped at 45°. 94

5.14 Bimorph micromirror after release. 94

5.15 Deformation vs. input power. Pulse duration=1 sec. 96

5.16 Deformation vs. input current. Pulse duration=1 sec. 97

5.17 Input power vs. Deformation. Polysilicon layer was doped at 950°C and annealed at 1100°C. Comparison of incremental annealing with one step annealing. Pulse duration=1sec 98

5.18 Deformation vs. input current. Polysilicon layer was only doped at 950°C. Comparison of incremental annealing with one step annealing. Pulse duration=1sec 99

5.19 Deformation vs. input power. Pulse duration=4 sec 100

5.20 Deformation vs. input current. Pulse duration=4 sec. 101

5.21 Deformation vs. input power. Pulse duration=10 sec. 102

5.22 Deformation vs. input current. Pulse duration=10 sec. 103

5.23 I-V characteristics of the actuators under investigation. 105

5.24 Deformation versus anneal time of the samples in group A for four different current values. 106

5.25 Deformation versus anneal time of the samples in group B for four different current values. 107

5.26 Required input power versus annealing time of the samples in group A to obtain four different deformation amounts. 108

5.27 Required input power versus annealing time of the samples in group B to obtain four different deformation amounts. 109

LIST OF FIGURES
(Continued)

Figure **Page**

5.28 Application # 1 for 45° tilted micromirror. 111

5.29 Application # 2 for 45° tilted micromirror. 111

5.30 Application for a vertical micromirror. 112

5.31 Application for a 135° tilted micromirror. 112

5.32 Schematic of the measurement setup for the scan angle of the micromirror. . 113

5.33 Frequency response of the reshaped micromirror with bimorph actuators driven with 10 V ac signal superimposed on 10 V dc voltage. 114

5.34 The photodiode response to the reflected laser beam at 10 Hz. 115

5.35 The photodiode response to the reflected laser beam at 166 Hz. 115

5.36 Solid model and mesh used to do modal FEA of the reshaped micromirror. . 116

5.37 The deformed shape of the reshaped micromirror at the 1st mode. 117

5.38 The deformed shape of the reshaped micromirror at the 2nd mode. 118

5.39 The deformed shape of the reshaped micromirror at the 3rd mode. 119

5.40 The deformed shape of the reshaped micromirror at the 4th mode. 120

5.41 Normalized tip position (t/t_{max}) 122

5.42 A prototype design for an integrated barcode-scanner module on a silicon substrate. 123

A.1 Newton-Raphson method of iterative locating zeros. 129

A.2 FEA Newton-Raphson Solution. 131

CHAPTER 1

INTRODUCTION

During the past thirty years, a continuing series of advances have carried microelectronics to ever higher levels. Monolithic logic chips, operational amplifiers, memory, microprocessors, data converters, digital signal processors, microcomputers, and a wide variety of ASICs have been the focus, which has produced a worldwide explosion in the processing and communication of information. Most of this information is now entered by typing, optical scanning, or voice. Looking ahead, however, many of the functions needed for future systems involve enhancing the ability to gather information and use it for control. Thus a major emphasis will be on microsystems that can gather information from the non-electronic world and/or use it to control the environment which surrounds us. The key devices for these microsystems are the sensors and actuators that perform the transductions function.

Today the successful fabrication and operation of microactuators and micro mechanical parts by merely IC-based micromachining technology enabled us to produce MEMS. The three characteristic features or the three "M"s of the technology are: *Miniaturization, multiplicity, microelectronics.*[1] Miniaturization is clearly essential. However, the mere miniaturization of macroscopic machines is not possible because of the scaling effect. Like a swarm of ants carrying large food, cooperative work of many micro elements can perform a large task, even when one single device can only produce small force or perform simple motion. Multiplicity is the key to successful micro systems. The integration of microelectronics is essential for micro moving elements to cooperate with each other and to perform a given task. In order to realize MEMS with above mentioned features, fundamental technological issues are materials, machining processes and devices. There are two kinds of machining

processes: one is based on semiconductor technologies and the other on mechanical means.

Microstructures fabricated by surface micromachining are planar by nature and have thickness of up to 10 μm in most cases. Some applications require thicker structures or three-dimensional-complicated structures. LIGA process [2] utilizes deep X-ray lithography [3], electroplating and molding to fabricated thick devices. UV-lithography with special resist, and deep RIE have also been used to make high aspect ratio microstructures and mold. If plated metals are used to make replicas, resulted structures are called HARMS, meaning high aspect ratio metallic structures. Wafer bonding technologies have been developed to build 3-D structures.

Modifications of surface micromachining have been introduced, too. One approach is to fold up micromachined plates from the substrate to construct a 3-D structure. The plate is released from the substrate and reconnected by hinges, flexible films or even active hinges. In other trials, overhanging structures were made.

Mechanical processes such as electro discharge machining (EDM), and ultrasonic machining [4] for microstructures have also been demonstrated. Unfortunately there is a trade-off between batch fabrication capabilities and 3-D complicated machining capability.

1.1 Background Information

1.1.1 Microactuators

A microactuator is the key device for MEMS to perform physical functions. Because of the scaling considerations [5], electromagnetic force [6, 7] which is most commonly used in the macro actuators is not the only driving force for microactuators. Many microactuators utilize other driving principles such as the electrostatic force [8, 9,

10, 11, 12], piezoelectric force [13, 14], shape memory alloys [15], thermal expansion [16, 6, 17], and pneumatical actuation [18, 19].

Each actuation principle has its own advantages and disadvantages. The choice and the optimization should be made according to the requirements of applications. Generally speaking, the electrostatic actuator can be completed within a chip (positioning of devices/heads/probes, sensors with servo feedback, light deflection and modulation etc.) since it is easily integrated on a chip, easily controlled and consumes little power. On the contrary, the other types of actuators are more robust, produce large force and are suitable to perform external tasks (propulsion, manipulation of objects, etc.)

Linear and rotary micromotors driven by electrostatic force have been improved over the last decade to reduce the friction, increase the speed, and driving voltage value, which can be still considered high and not IC compatible.

One way to reduce the effect of friction is utilizing elastic supports. The most popular example is a comb-drive actuator [11, 20]. It is supported by double fold-beams and actuated by interdigitating comb-like structures. The electrostatic force to increase the overlapping is generated when voltage is applied between suspended and fixed comb. The typical displacement is 10 μm and the force is 10 μN.

Microactuators utilizing other driving principles as piezoelectric, thermal expansion and electromagnetic move, in terms of reducing friction, elastically with some exceptions. The ultrasonic micromotor/actuator utilizes the standing wave to drive the rotor/slider. Vibrations of cantilevers can carry objects. Levitation by repulsive force between the permanent-magnet and superconducting material, by air pressure from small holes and controlled electrostatic force was demonstrated. Micromachined STM (scanning tunneling microscope) composed of piezoelectrically driven cantilever was successfully operated to take atomic images [13].

Shape memory alloys (TiNi etc.) undergo a crystalline phase change when heated or cooled above ambient. This phase change is accompanied by a change in Young's modulus. The premier application of these microactuators lies in microvalves, but other potential applications include microconnecters, switches, and end effectors for microrobotic manipulators [21].

If we want to have MEMS to perform a macroscopic task, the key idea is to coordinate simple motions of many microactuators [22, 23]. Even when each moving step is small, actuation of many steps covers large distance. A heavy load can be distributed among many actuators, which produce only small force. Friction in micro scale prohibits us from using gears and joints. Suspended actuators do not suffer from friction, but their motion range is limited. If many such actuators are arranged in series or in parallel, the overall structure can produce larger force and displacement and perform more complicated functions than each simple actuator. Arrays of cantilever actuators which vibrate in synchronization [24] and convey objects, an in-plane conveyance system using controlled air flow from arrayed nozzles on the substrate were operated successfully [25]. A projection display based on arrayed movable micromirrors is commercialized.

1.1.2 Micromirrors

In 1977, Petersen demonstrated deflecting light beams by small cantilevers driven by electrostatic force [26]. Since then, many implementations of micro-opto-electro-mechanical systems (MOEMS) for a variety of applications have been demonstrated. Such applications go beyond single devices to include whole optical systems on a chip, comprising mirrors, gratings, Fresnel lenses, shutters, and actuators. Now MOEM structures are reaching commercialization.

First micromirrors were planar micromachined structures and they needed manually to be lifted up and locked with hinges in place to 90°. Recently, micromirrors actuated electrostatically [27] and electrothermally [28] were reported.

Many optical devices, especially micromirrors have been developed for communication systems, especially for fiber communication networks. MEMS displays based on movable mirrors [29] utilizing Digital Micromirror Devices (DMD) were developed. DMD is TI's commercialized micromirror device, which is an aluminum mirror, suspended over an air gap by two thin torsion hinges that permit a mirror rotation of ±10°.

An integrated external-cavity-laser module, which incorporates a silicon-micromachined micromirror with on-chip actuators [30]. Another possible application of micromirrors is microscanners for barcode readers [27].

1.2 Objective of this Research

The goal of this research has been to understand the nonlinear actuation behavior of thermally and electrostatically driven microactuators, and to propose a novel microfabrication technology to realize 3D microstructures and actuators.

The ability of actuators to produce large displacements in all three dimensions with small power consumption makes them very desirable for MEMS applications. Mono- or multimorph cantilever beam actuators promise large in- and out-of-plane actuation by employing stress gradient, residual stress in the layers, or thermal expansion coefficient mismatch between the layers.

Deflection of released monomorph beams due to the stress gradient throughout the thickness has been observed and reported before. In this work, for the first time, a linear model is proposed to describe this linearly temperature dependent deflection, by employing thermal expansion coefficient gradient throughout the thickness of monomorph beams.

Thermally driven bimorph microactuators were first discussed by Benecke and Riethmuller in 1988. Recently, bimorph inchworm in-plane actuators were fabricated in NJIT. In this work, a linear analytical model, which considers the temperature dependent residual stress, is proposed, and results obtained are compared with numerical FEA results, where the residual stress is included in the solid model as thermal load. To improve the inchworm, a novel two-segment bimorph actuator is proposed, and nonlinear FEA simulation results for three cases with different MEMS material combinations are presented.

The actuation of bimorph out-of-plane actuators have been described with linear analytical models, and the validity of these models have never been questioned. In this work, the results based on these models are compared to numerical results obtained from FEA and experimental measurements due to fabricated devices, and it is shown that nonlinearities need to be considered while designing actuators with large displacements, and accurate results are obtained by using iterative numerical methods or FEA.

A novel technique, *reshaping*, is introduced to fabricate 3D actuators. In this technique reshaping is achieved through introduction of elastic stresses in polysilicon structures compensated by annealing due to Joule heating. A similar approach was proposed by Fujita and his group, but no further analysis has been done. In this Ph.D. work, a detailed investigation of the reshaping process is presented, experimental results to understand the physical fundamentals are given and discussed. Reshaped actuators to realize a micromirror system are introduced. The actuation mechanisms are studied on the fabricated devices and successful demonstration of the proposed approach is presented.

1.3 Organization of this Dissertation

The introductory concepts about microactuators and micromirrors are presented in this chapter. Chapter 2 deals with mechanical properties of thin films, origin and characteristics of stresses in thin film materials utilized in MEMS fabrication. Furthermore in the same chapter, a model is proposed, which takes temperature dependent stress gradient observed in monomorph materials popular in MEMS into account.

Chapter 3 is devoted to in-plane cantilever (inchworm) actuators. The temperature dependent residual stress is used in order to obtain large in-plane displacement. An analytical model is proposed to explain the thermal behavior of the inchworm actuator, and the validity conditions of this linear model are discussed. The numerical results obtained from this model are compared with the simulation data and test results. It is shown, that the friction between the tip of the actuator and the surface may cause a degradation in the performance of the actuator. To overcome this problem the design of a novel two-segment bimorph actuator is discussed.

Chapter 4 deal with the analysis, design and fabrication of out-of-plane actuators. The thermal mismatch is utilized to obtain large displacements at the tip of these bimorph cantilever actuators. It is shown, that well known analytical equations for linear thermal models are not valid, when nonlinearities start dominating. Models for numerical methods are discussed and the numerical results of nonlinear Finite Element Analysis (FEA) are compared with the test results measured from fabricated devices. Also, the electrostatic drive of out-of-plane actuators is discussed. An analytical 2D model is compared with the FEA and test results. Finally in this chapter, design, fabrication and test results of a micromirror are reported. Two out-of-plane bimorph actuators are utilized to

position this micromirror, which is driven combined with thermal and electrostatic excitation.

In Chapter 5, a new 3D micromachining technology, reshaping, is introduced into MEMS technology. The fabrication and detailed experimental results are presented. A novel reshaped micromirror is reported as an example of the reshaping technology, and an MOEM system, *Microscanner for Barcode Readers* is proposed.

Finally, Chapter 6 includes conclusion and discussions.

CHAPTER 2

MECHANICAL PROPERTIES OF THIN-FILMS AND STRESS

Interest in mechanical-property effects in thin films has focussed on two major issues. The primary concern has been with the deleterious effects that stress causes in films. This has prompted much research to determine the type, magnitude, and origin of stress as well as means to minimizing and controlling stresses. A second important concern is related to enhancing the mechanical properties of hardness and wear resistance in assorted coating applications.

The topic of stress in films has historically generated the greatest attention. It is virtually always the case that stresses are present in thin films. Nucleation conditions and high deposition rates which are typical in physical and chemical vapor-deposited films produce high stress which can be measured. However, their origins are not known with certainty. What must be appreciated is that stress (stray stress [31]) exists even though film is not externally loaded. Stresses directly affect a variety of phenomena, including adhesion, generation of crystalline defects, perfection of epitaxial deposits, and formation of film surface growths such as hillocks and whiskers. Film stresses that tend to increase with thickness are a prime limitation to the growth of very thick films because they promote film peeling.

Integrated circuit (IC) technologies employ substrates which are decorated with a variety of thin films. As device sizes continue to shrink, various material properties, which were acceptable, can cause problems, at smaller geometries. When high strain fields are present, electronic device performance degrades. For example, increase in leakage currents leads to severe problems in dynamic MOS circuits which increase with size reduction. Increased etch and diffusion rates in strained regions are common and reduce yield. Mechanical stress induced dislocation generation and cracking cause device yield problems, too. Even slight bowing of silicon wafers in

IC technology presents significant problems in maintaining precise tolerances in the definition of device features.

The developing field of micro-electro-mechanical systems (MEMS) utilizes processes developed for ICs and employs micron scale thin film structures that are totally or partially freed from substrate. High stress is undesired for mechanical structures, because upon release, the large stress present in thin films can cause device failure by instability, curling, or fracture. In addition, stress affects device performance by, for example, altering the resonance of resonant microstructures and thin film diagrams. In mechanical sensors, small stray stresses are manifested as noise signals that are detected by the sensor yielding incorrect results.

As seen from the discussion above stress has been harmful in both ICs and MEMS. However, in this work, it is shown that controlled stress in thin films can be put to use in a constructive way with the generation of electro-thermal actuation. In this chapter, some basic mechanical concepts, measurement techniques of mechanical properties of thin films towards understanding origin of stress and mechanical behavior of thin films is discussed.

2.1 Strength of Materials

2.1.1 Stress and Strain

Stress is a basic concept used to denote the intensity of internal force. It is a convenient basis for analyzing the internal resistance of a structure subjected to load. If the plate in Figure 2.1(a) is stretched by equal and opposite axial tensile forces F, then it is both in mechanical equilibrium and in a state of stress. Since the plate is in static equilibrium, it can be cut as shown in Figure 2.1(b), revealing that internal forces must act on the exposed surface to keep the isolated section from moving. Regardless where and at what orientation the plate is cut, balancing forces are required to sustain equilibrium. These internal forces distributed throughout the

plate constitute a state of stress. In the example shown, the normal force F divided by the area A defines the tensile stress σ_x.

$$\sigma_x = \frac{F}{A} \tag{2.1}$$

Similarly, normal stresses in the remaining two coordinate directions, σ_y and σ_z, can be imagined under more complex loading conditions. If the force is directed into the surface, a compressive stress arises. Convention assigns it a negative sign, in contrast to the positive sign for a tensile stress. In addition, mechanical equilibrium on internal surfaces cut an arbitrary angle will generally necessitate forces and stresses (shear stress, τ) resolved in the plane itself. Two subscripts are generally required to specify a shear stress: the first to denote the plane in which the shear occurs,a nd the second to identify the direction of the force in this plane (Figure 2.1(c)).[32]

All bodies undergo deformation when subjected to load. The deformation may be a constant for a given load, or it may be progressive and cumulative, depending upon the magnitude of load, and perhaps upon the manner in which the load is applied. A basic unit to represent the deformation in a relative sense is needed. *Strain* is such a unit, defined as the deformation per unit length.

$$\epsilon_x = \frac{\delta l}{l_o} \tag{2.2}$$

In a similar way, the unit angular deformation, shearing strain, can be given as:

$$\gamma_{xy} \approx tan\alpha \tag{2.3}$$

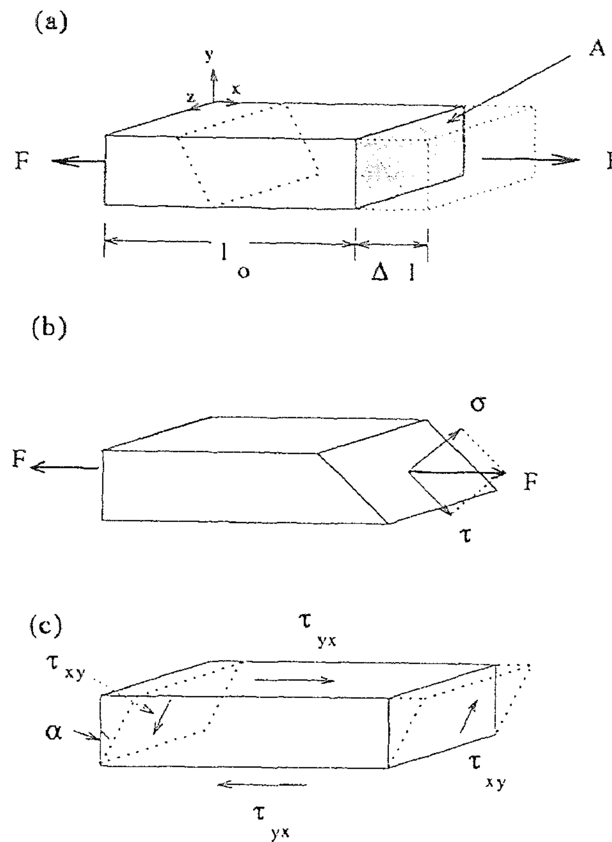

Figure 2.1 (a) Tensile force applied to plate. (b) Arbitrary free-body section revealing spatial distribution of stress through plate. Both tensile and shear stresses exist on exposed plane. (c) Distortion in plate due to applied shear stress.

2.1.2 Elastic Deformation and Hooke's Law

All materials deform when subjected to load. For most materials a change in load results in a corresponding, but not necessarily linear, change in deformation. Furthermore, most materials tend to regain their original shape after the removal of a load, if the load and temperature are not excessive. If, upon the removal of the load, a body returns to its original size and shape, the body has undergone elastic deformation. The ability of a body to regain its original shape is known as elasticity. The elastic regime is at one extreme. At the other extreme are the irreversible plastic effects induced at stress levels above the limit of the elastic response (i.e. the yield

stress). Figure 2.2 gives the typical shape of the load-deformation (or stress-strain) relationship for many materials.

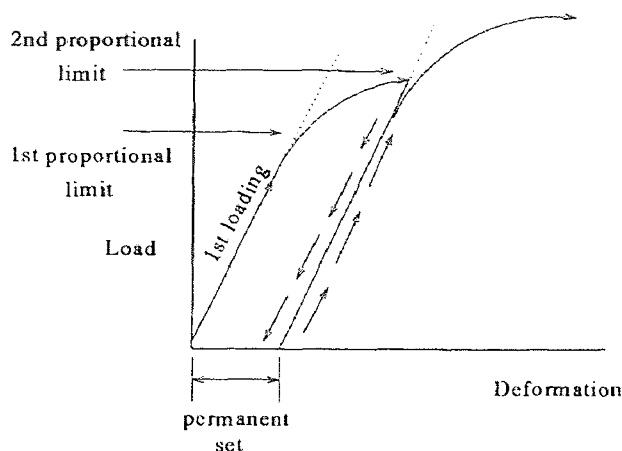

Figure 2.2 Load-Deformation curve

Robert Hooke recognized a definite relationship between elastic deformation and load[1]. Generalized in its simplest form Hooke's law says that stress is proportional to strain. Thomas Young introduced a constant of proportionality, *the modulus of elasticity*, or *Young's modulus* (designated by E), which is a measure of stiffness of the material [33].

$$E = \frac{\sigma}{\epsilon} \tag{2.4}$$

For shear stresses and strains, the proportionality constant is G (sometimes called the modulus of rigidity).

$$G = \frac{\sigma}{\epsilon} \tag{2.5}$$

Axial elongation is always accompanied by a lateral contraction (or vice versa). The ratio of lateral strain to the axial strain is expressed by a constant known as the *Poisson's ratio*, after a French mathematician, Simeon Poisson. Represented by ν, the Poisson ratio is

[1]In his 1678 treatise *Ut tensio sic vis*

$$\nu = \frac{lateral strain}{axial strain} = \frac{-\epsilon_{lateral}}{\epsilon_{axial}} \tag{2.6}$$

The Poisson ratio for the <100> bulk silicon is 0.28. [31]

2.2 Stress in Thin Films

A variety of thin film materials is available for the construction of sensors and actuators. High quality insulators such as silicon dioxide or silicon nitride, conductors such as aluminum, and semiconductors such as silicon are a few examples. It is known that the thin film materials can have properties which differ from their bulk counterparts. Thin films exhibit stray stress, and this internal stress is strongly process dependent. Other materials are metals, piezoelectrics, polyimides. Some of the thin film deposition techniques are low-pressure chemical vapor-deposition (LPCVD), plasma-enhanced chemical vapor-deposition (PECVD), sputtering, spin-on coating, and evaporation.

There are two major sources of stray stresses: thermal stresses and residual stresses. Thermal stresses are the product of mismatches in the thermal expansion coefficients of different films. In thin films, thermal stresses develop because these films are grown at higher than ambient temperature. Typically thermal strains in the order of $5x10^{-4}$ are observable in silicon micromachined structures. Thermal stresses also develop at microdevice- package interface. Stress isolation techniques that use soft buffer layers [34] and stress relaxation [35, 36] structures are essential for the proper operation of microstructures.

A much larger component of stray stress is residual stress. Residual stresses develop because as-deposited thin films are not in the most favorable energetic configuration. Residual stresses can be compressive, which make the film expand, or tensile, which makes the film shrink. A model for the generation of residual stress during

the deposition of films is illustrated in Figure 2.3. Origin of the process dependent residual stress in a variety of thin film materials will be discussed later in this chapter.

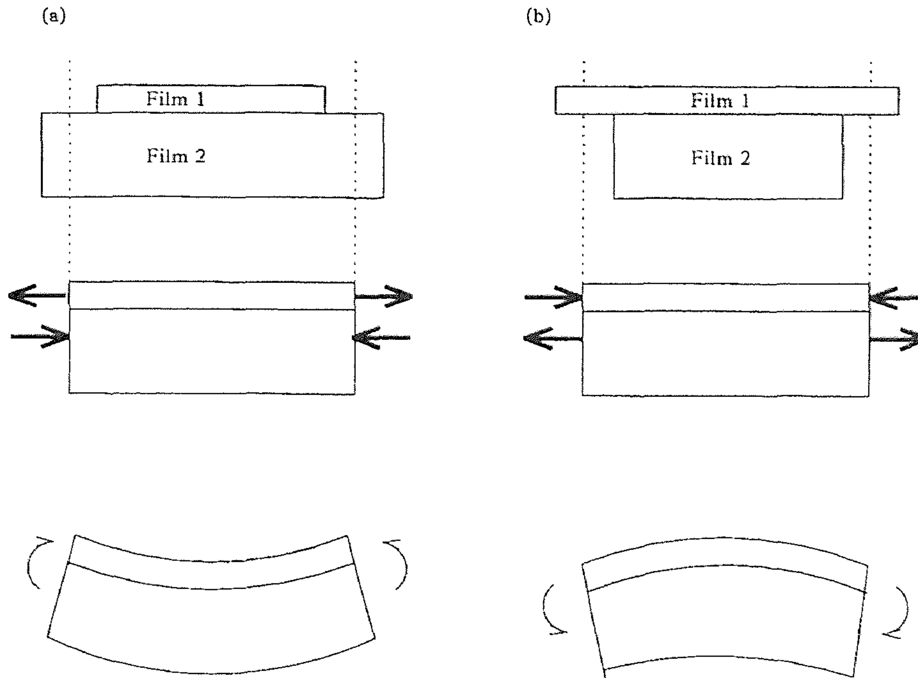

Figure 2.3 Sequence of events leading to (a) residual tensile stress in film; (b) residual compressive stress in film

Since these films are firmly attached to the substrate, the internal strain cannot be relaxed, hence causing mechanical deformation. Residual stresses can be relaxed by high temperature anneals; however, the anneal temperatures are quite high and may not be practically applicable for particular structures.

Regardless of the stress distribution that prevails, maintenance of mechanical equilibrium requires that the net force (F) and bending moment (M) vanish on the film-substrate cross section. Thus

$$F = \int \sigma \, dA = 0 \tag{2.7}$$

$$M = \int \sigma \, y \, dA = 0 \tag{2.8}$$

where A is the sectional area and y is the moment lever arm.

The formulas that have been used in almost all experimental determinations of film stress are variants of an equation first given by Stoney [37]. It makes use of (2.7) and (2.8). The equation can be derived with reference to Figure 2.4, which shows a composite film-substrate combination of width w. The film thickness and Young's modulus are d_f and E_f, respectively, and corresponding substrate values are d_s and E_s. In the free-body diagrams of Figure 2.4(b) each set of interfacial forces can be replaced by the statically equivalent combination of a force and moment: F_f and M_f in the film, F_s and M_s in the substrate, where $F_s = F_s$. Assuming that d_s is normally much larger than d_f, the film stress σ_f is, to a good approximation, given by Stoney's formula [32]:

$$\sigma_f = \frac{F_f}{d_f w} = \frac{1}{6R}\frac{E_s d_s^2}{(1-\nu_s)d_f} \tag{2.9}$$

In order to convert the measured deflection into film stress, the curvature-beam displacement relationship (i.e. $1/R = d^2y(x)/dx^2$) is used. After integration, $y(x) = x^2/2R$. For a cantilever of length l. if the free-end displacement is δ, then $\delta = l^2/2R$, and Stoney's formula yields

$$\sigma_f = \frac{\delta E_s d_s^2}{3l^2(1-\nu_s)d_f} \tag{2.10}$$

2.3 Origin of Stress in Thin Films

Over the years, many investigators have sought universal explanations for the origin of the constrained shrinkage that is responsible for the residual stress. Buckel [38] classified the conditions and processes conductive to internal stress generation into the following categories:

- Differences in the expansion coefficients of film and substrate
- Incorporation of atoms (e.g. residual gases) or chemical chemical reactions

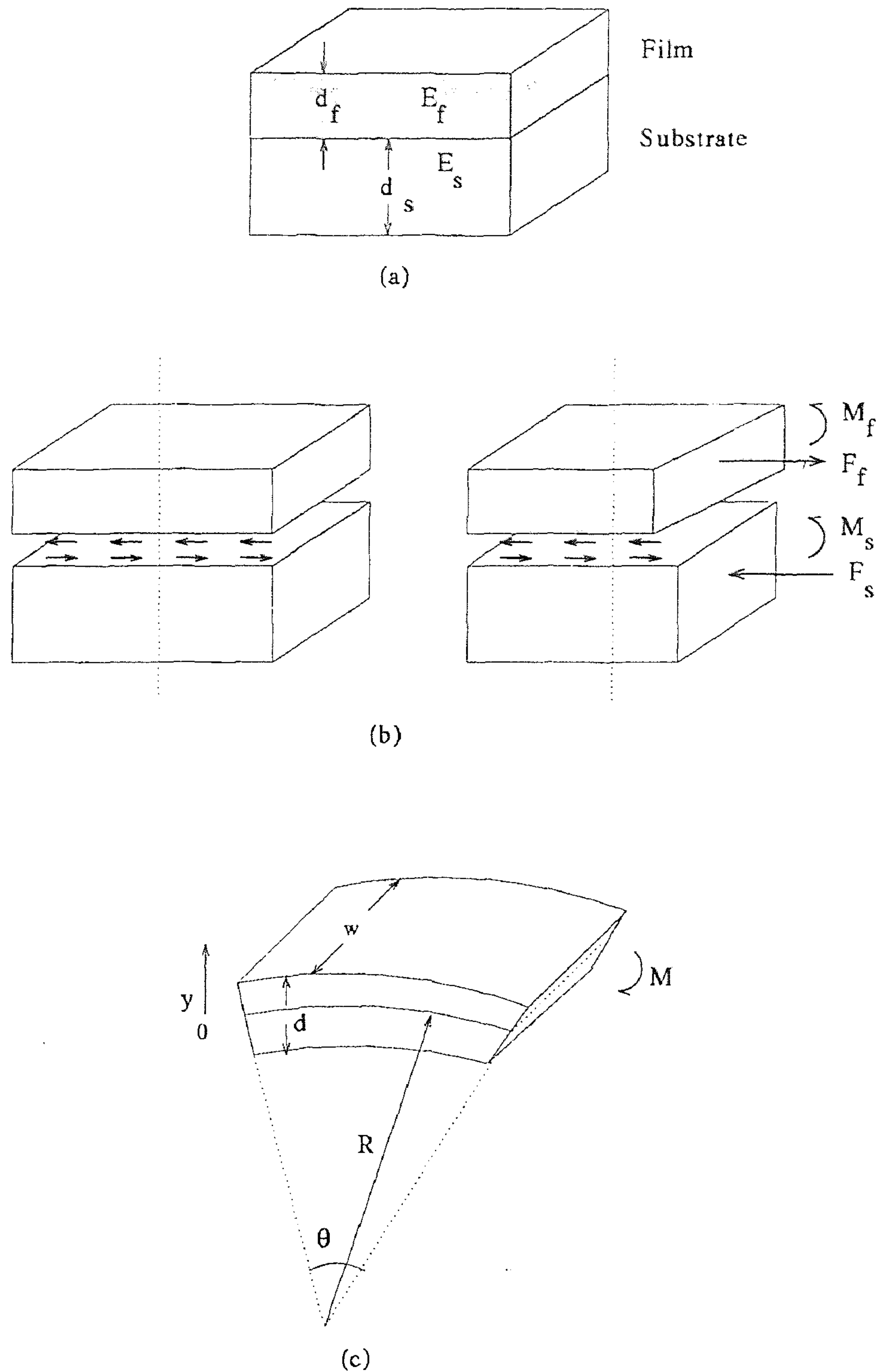

Figure 2.4 Stress analysis of film-substrate combination: (a) composite structure; (b) free-body diagrams of film and substrate with indicated interfacial forces and end moments; (c) elastic bending of beam under applied end moment.

- Differences in the lattice spacing of monocrystalline substrates and the film during epitaxial growth
- Variation of the interatomic spacing with the crystal size
- Recrystallization processes
- Microscopic voids and special arrangements of dislocations
- Surface quality
- Phase transformations

2.4 Stress Gradient in Monomorph Films

It is almost always the case, that stresses exist in thin films. When a surface-micromachined monomorph beam or diaphragm is released from the substrate, it curls up or down (Figure 2.5). The cause of this deformation is the gradient of the in-plane residual stress throughout the thickness of the film. The variation of internal stress through the thickness of a film leads to an internal bending moment. To analyze this, consider a structural member having width w, thickness t and residual stress $\sigma(y)$ (Figure 2.6). There will be an internal bending moment M_1 which is given by

$$\begin{aligned} M_1 &= \int_0^t \sigma(y) w (y - \frac{t}{2}) dy \ , \\ \sigma(y) &= \overline{\sigma} + \Delta\sigma(y). \end{aligned} \qquad (2.11)$$

where $\overline{\sigma}$ is the average stress. $y = 0$ is the middle of the film. From Eq. 2.11, the moment is zero unless $\sigma(y)$ varies with y. A linear variation of stress is assumed throughout the film thickness.

When a polycrystalline thin film is deposited on top of another layer, a transition layer of small grains is expected to form at the interface. Columnar grains grow out of this transition layer (Figure 2.7) [39]. This structural change of the

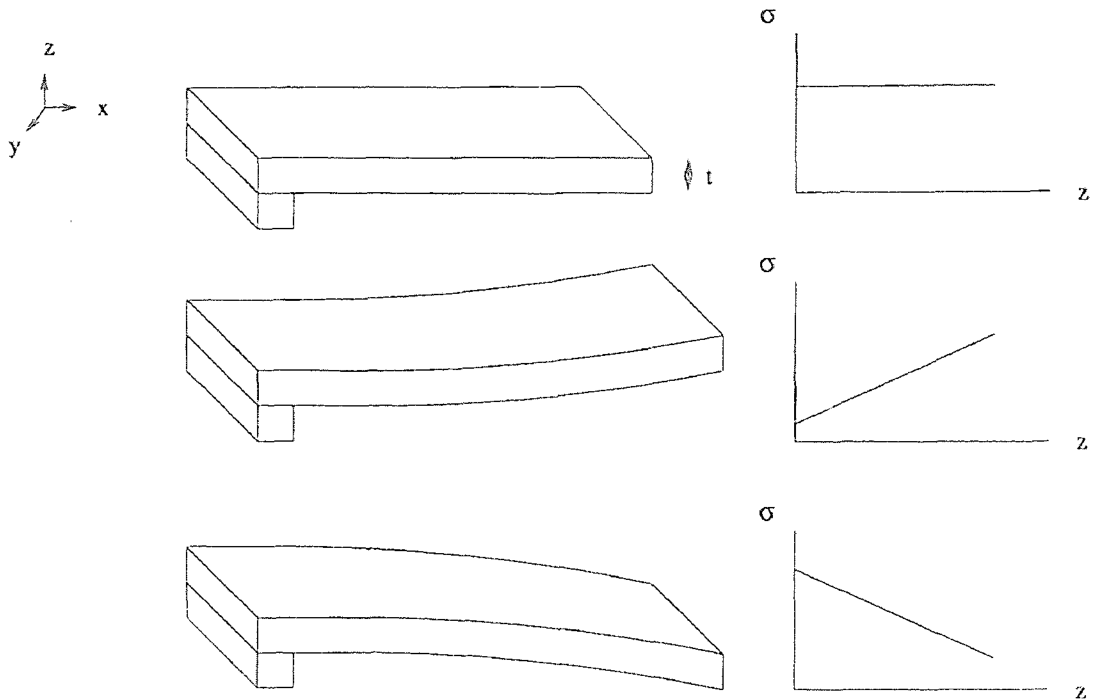

Figure 2.5 Schematic of released monomorph beams with internal stress (a) uniform internal stress, (b) positive stress gradient throughout the thickness, (c) negative stress gradient throughout the thickness.

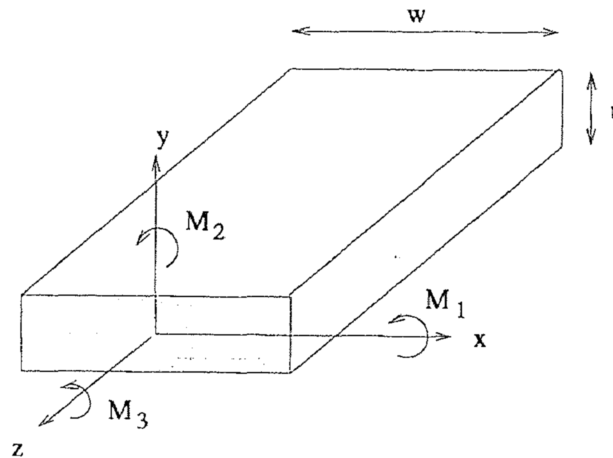

Figure 2.6 A structural member with the coordinate system.

film is modeled with thermal expansion coefficient, which varies uniformly through the thickness of the film. According to this proposed model, $\Delta\sigma(y)$ is temperature dependent and it given as

$$\Delta\sigma(y,T) \;=\; \Upsilon\;\Delta T\;E(y-\frac{t}{2}) \qquad (2.12)$$

where Υ is thermal expansion coefficient gradient, and ΔT is the temperature difference with respect to the process high temperature, where the film is stress free.

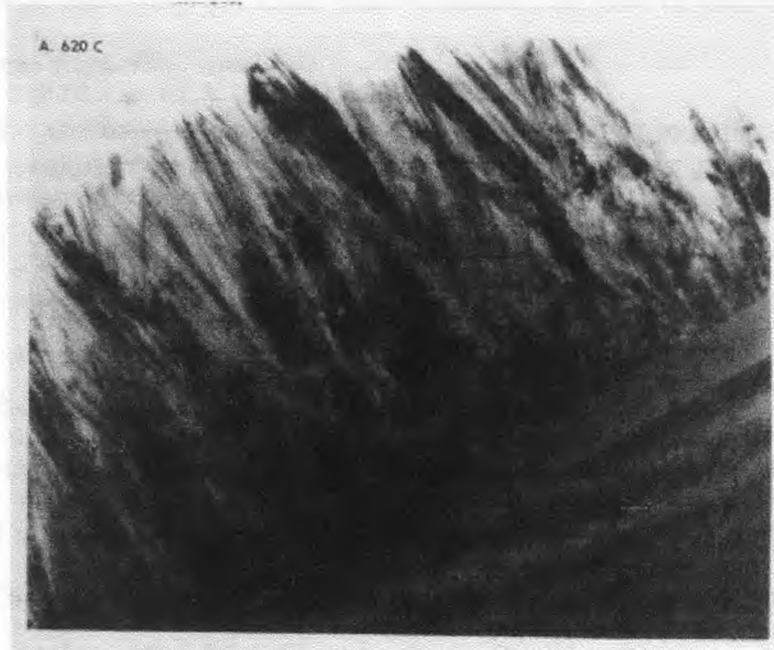

Figure 2.7 Cross-sectional TEM micrograph of columnar grains grown out of a transition layer of small grains at the SiO_2 interface.

Inserting Eq. 2.12 into Eq. 2.11 and integrating, the moment is obtained as

$$M_1 \;=\; \frac{\Upsilon\;\Delta T\;Ewt^3}{12}. \qquad (2.13)$$

For small stress values (i.e. small displacements), the vertical deflection δ at any point of the cantilever is found to be

$$\delta = \int \frac{M}{EI} x dx \qquad (2.14)$$

where I is the moment of inertia and it is equal to $wt^3/12$ for the cantilever beam with a rectangular cross-section. The displacement at the tip of the beam ($x = L$) due to stress gradient is

$$\delta(L) = \frac{\Upsilon \, \Delta T \, L^2}{2} \qquad (2.15)$$

Eq. 2.15 is valid only for small displacements. In case of large displacements, one needs to use numerical methods.

Under the assumption, that the curled cantilever beam is perfectly circular the radius of curvature can be written as

$$r = \frac{E}{\frac{\Delta\sigma}{\Delta y}} \qquad (2.16)$$

where $\Delta\sigma/\Delta y$ is stress gradient per μm. Once the radius is calculated, the displacement throughout the beam can be calculated from trigonometry (Figure 2.8). The shape of a poly cantilever with a stress gradient of 1.7 MPa/μm is shown in Figure 2.9. The dimensions of the beam is $1mmX30\mu mX1.5\mu m$. The gap between the cantilever beam and the substrate at the fixed end is 1 μm.

In FEA, stress gradient is included into the model as a load as follows. The solid model is meshed with layered elements or created in a layered manner (Figure 2.10). The thermal expansion coefficients are calculated in such a way that the internal stress varies throughout the thickness according to the experimental stress gradient value. This value is calculated from the displacement of the released, up- or down-curled test cantilever beams.

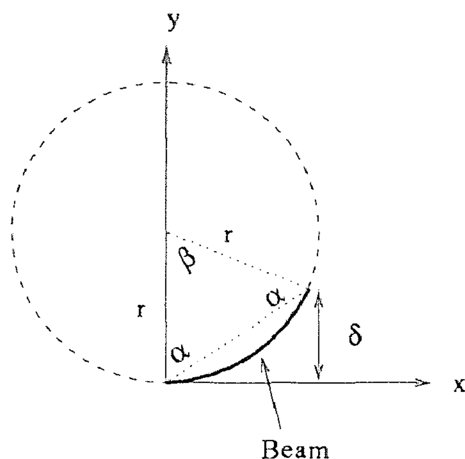

Figure 2.8 Calculation of the displacement from the circle with a radius r.

2.5 Process-Dependent Residual Stress

2.5.1 Silicon Nitride

Silicon nitride is normally formed by chemical vapor deposition, either from mixtures of ammonia and silane (at atmospheric pressure, APCVD), or from ammonia and dichlorosilane (at low pressure, LPCVD). The thermal expansion coefficient is slightly larger than that of silicon. This implies that there will be a small component of tensile stress resulting from cooling to room temperature from typical deposition temperatures. However, Tamura and Sunami have shown [40] that the thermal mismatch stress accounts for only a small fraction of the total observed tensile stress.

The mechanism for this additional stress component is not well understood, although it is clearly sensitive both to deposition temperature and to composition variations induced by modification of the silane or dichlorosilane to ammonia ratio during deposition [41, 42]. The stress is not strongly dependent on post-deposition annealing, even though it is observed [41] that residual Si-H and N-H bonds are present immediately after deposition, but can be removed by high temperature anneal.

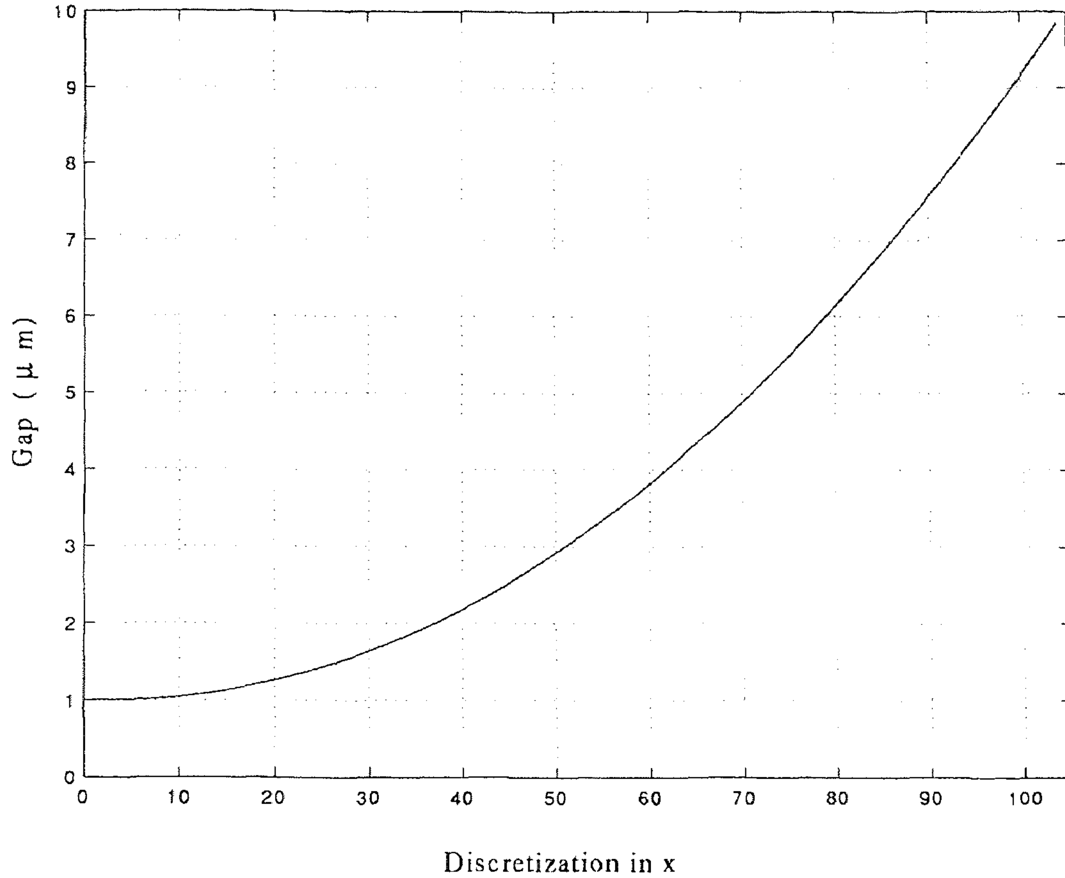

Figure 2.9 Calculated shape of a polysilicon cantilever with a stress gradient mbox(1.7 MPa/μm) throughout the thickness. The beam was divided into 100 small elements for the following numerical pull-in calculations discussed in Section 4.3. (Dimensions 1 mm X 30 μm X 1.5 μm)

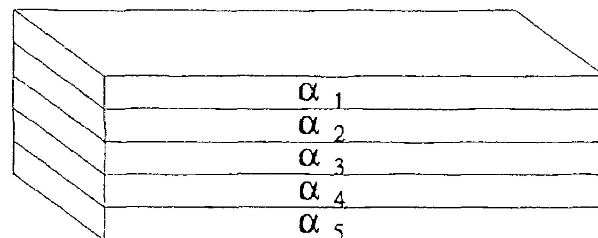

Figure 2.10 Layered solid model for FEA. Stress gradient throughout the thickness is modeled with thermal expansion gradient ($\alpha_1 \neq \alpha_2 \neq \alpha_3 ...$).

2.5.2 Polysilicon

Either tensile and compressive stress can occur in polysilicon layers depending on the process temperature and process conditions. The origin of large tensile and compressive intrinsic stresses can be discussed in relation to the evolution of the polysilicon microstructure. Undoped polysilicon films deposited by LPCVD near 600°C consist of more or less equi-axed grains and are tensile, due to an amorphous to crystalline solid state transformation that occurs during the film deposition. At deposition temperatures exceeding 630°C, the grains are columnar and the stress is compressive. The source of compression is still uncertain, but was shown to be related to a transition layer of small grains at the film/substrate interface. [39]

Doping [43] and annealing [44] can affect the stress profile. It was shown that a 2-hour annealing step in N_2 environment at 1100°C can decrease the internal stress significantly [44].

Stress profile throughout a polysilicon film can change sign (from tensile at the bottom to compressive at the top) [39]. Different researchers tried to explain this phenomena. One explanation is the plastic deformation of the top surface, while oxidation and doping [45]. According to a recent work, the varying stress profile is related to oxygen diffusing in polysilicon during doping [46].

2.6 Stress Measurement Techniques

There are a large number of techniques for the determination of stress in thin films. The goal may differ: a technique for average stress determination or one for local stress measurement.

The first method is a simple one to measure average stress. It utilizes two lasers and a mirror and a full wafer (a test wafer cover with the film whose internal stress is to be measured) is required. Figure 2.11 Two laser beams, directed towards the wafer, are reflected from the surface and creates two spots on the millimetric scale.

The distance between these spots gives information about the warpage of the wafer only if it is compared with the distance between two spots obtained from the same wafer without the particular film. (2.17) gives the residual stress in the thin film in MPa,

$$\sigma_{residual} = \frac{12.3\ .\ (d_a - d_b)}{t_f} \tag{2.17}$$

where t_f is the film thickness in μm and d_a and d_b represent the distances between the two spots on the scale obtained with and without the film, respectively. In this work, this method was utilized to obtain residual stress value in thin films.

A precise technique for local rather than average stress determination is based on X-ray diffraction method. By measuring the lattice spacing in the stressed film $\bar{a}_o$ as well as unstressed bulk lattice (a_o) with X-rays, film stress can be determined from the following equation.

$$\sigma_f = -\frac{E}{2\nu}\frac{\bar{a}_o - a_o}{a_o} \tag{2.18}$$

Even though of X-ray techniques are highly accurate, requirement of special equipment is an important drawback.

Another technique employs circular plates of the substrate with the particular film on top of it. Equation (2.10) describes the resultant stress, where l is now the plate radius and δ represents the center deflection. a typical arrangement for stress measurement of plates is shown in Figure 2.12, where the change in the optical fringe pattern between the film-substrate and an optical flat is used to measure the deformation. Alternatively, a calibrated optical microscope can be used to measure the extent of bowing. [47]

In another film-substrate configuration, the substrate is fashioned into the shape of a cantilever beam. With the film deposited on one surface, the deflection of the free end of the beam is then determined utilizing Stoney's formula. Elongation

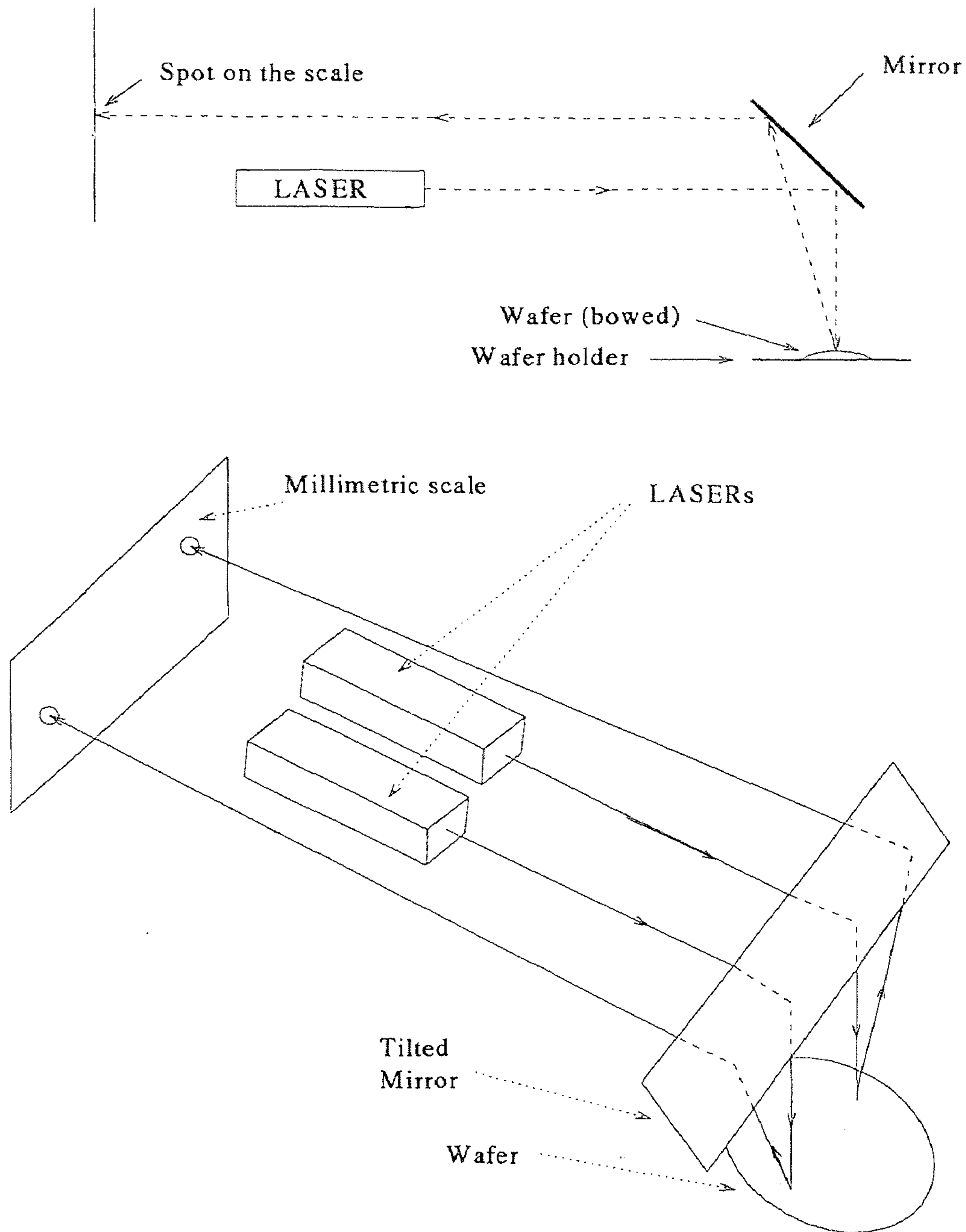

Figure 2.11 Schematic diagram of two-laser film stress measurement technique.

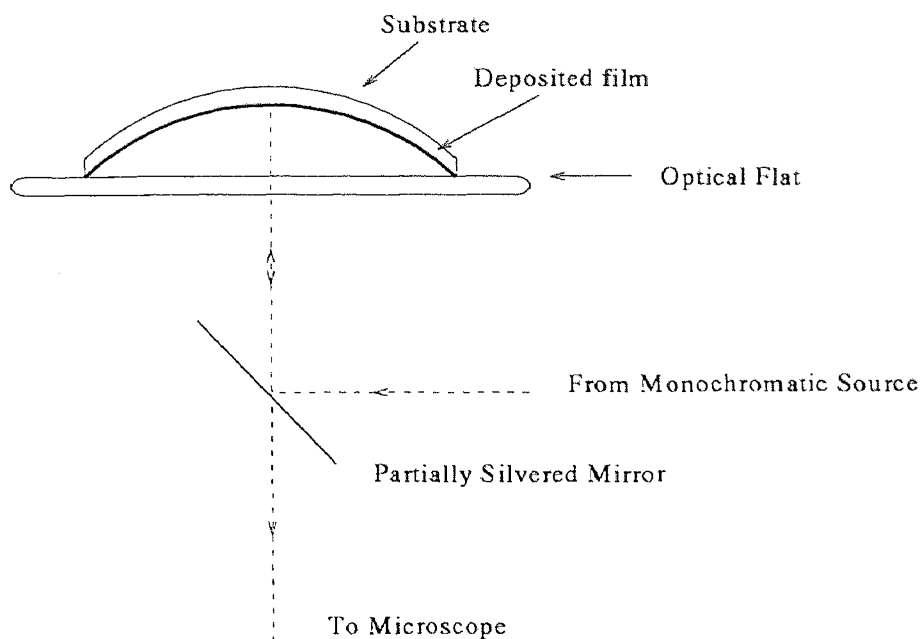

Figure 2.12 Schematic diagram of circular-plate film stress measurement technique.

measurements of clamped beams overhangs are acceptable but require destructive measurement techniques.

Buckling offers an alternative for the accurate determination of compressive stress in thin films. This technique involves the fabrication of doubly supported beams. It requires one step photolithography, after release of the beams local film strain can be easily found out. Beams with identical cross sections but changing lengths were found to be perfectly straight and free of bowing below a critical length and buckled above this cutoff point [48].

As the double-beam type structures are not susceptible, for buckling at tensile stress another shape of structure is necessary. A 'diamond beam' structure, which converts tensile strain to compressive strain, was proposed [49].

Other techniques with more complicated structures for the measurement of residual stress and Young's modulus of thin films with a better accuracy exist [50].

CHAPTER 3

INCHWORM (IN-PLANE) ACTUATOR

The driving principles of microactuators were reviewed in the first chapter. LIGA type processes have a monopoly on magnetic applications and until recently, large vertical dimensions. In the recent years, reactive ion etching has been an important alternative. However, electromagnetic force, which is most commonly used in the macro actuators is not the only driving force.

Electrostatic attraction force has been considered since 1960s [51]. The use of this force as a driving force has been studied for both in-plane and out-of-plane actuators. It has been demonstrated that interdigitated finger (comb) structures are very effective for exciting electrostatically the resonance of polysilicon microstructures parallel to the plane of the substrate [11]. Another electrostatically actuated structure is a curved electrode actuator [52]. Although the typical driving voltage required has been reduced from 100's of volts to a few 10's of volts [53], these values are still above the CMOS compatibility limit. The driving power is very small, so is the output torque (or force), which is in [pN-m] range [54].

In 1992, Guckel et al. proposed a thermo-magnetic metal flexure actuator, which was driven by magnetic forces and thermal expansion [6]. A so called SLIGA (deep x-ray lithography, metal plating coupled with sacrificial etch) process was required to fabricate very high aspect ratio structures. Air Force Institute of Technology (AFIT) adapted the thermal drive part of this idea to a surface micromachining process, which was utilizing thick polysilicon as the actuator material [55]. The thermal actuation was based on the deflection of a U-shaped actuator because of the temperature difference between the actuator arms with different widths (Figure 3.1).

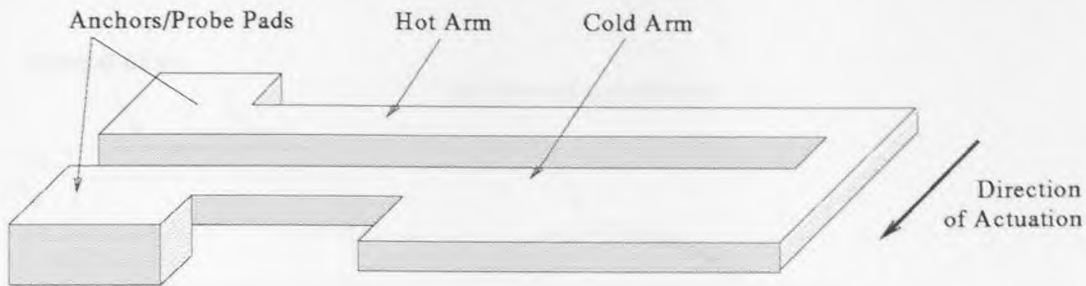

Figure 3.1 AFIT's thermal actuator.

Keller and Howe demonstrated another type of thermally actuated structures, namely nickel-filled hexsil tweezers. These in-plane actuators were molded micromachines consisting of a high aspect-ratio CVD polysilicon shell with electroless nickel for the conductive regions. The process was totally an unconventional one. [16]

Many thermally excited microactuator structures based on bimorph structures [56] and their applications [17] were proposed by Benecke and Riethmüller.

The main advantage of electro-thermally driven actuators is the significant increase in force (or torque). However, the power dissipation increases, too.

3.1 Device Description

In this chapter the design, fabrication and test of an in-plane actuator will be discussed. The actuator is a bimorph cantilever and the structure is in balance at high temperature. Following the sacrificial etch at room temperature, the cantilever bows upwards due to internal stress. The actuator exhibits an actuation similar to an *inchworm* to achieve a lateral in-plane displacement of its tip along the underlying surface (Figure 3.2).

The actuator can be driven by either thermal or electrostatic force or both. At least one layer needs to be metal or highly doped semiconductor, which serves as the heater. When thermal voltage V_a is applied, I_a passes through the heater, the

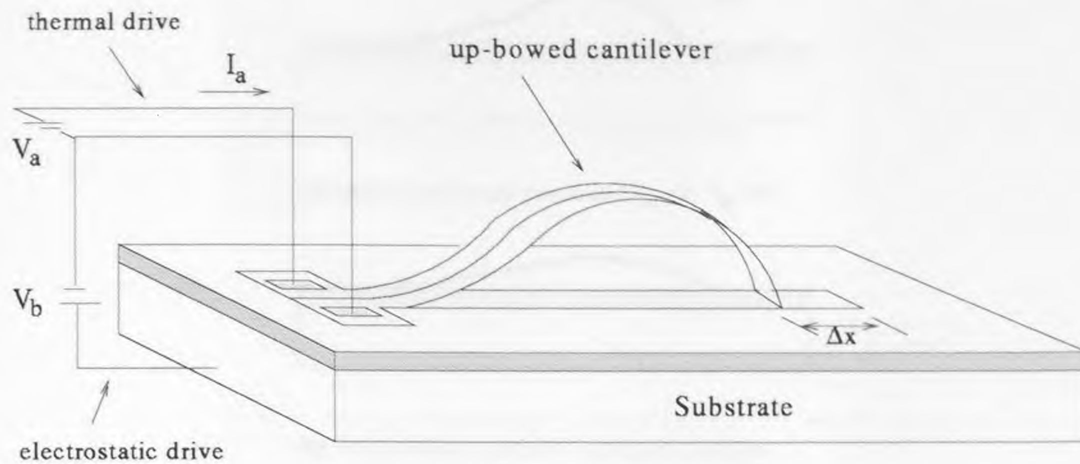

Figure 3.2 A schematic view of up-bowed actuator

up-bowed cantilever beam heats up and stretches out. During electrostatic drive, V_b causes the actuator to be attracted towards the substrate, the tip is pushed laterally along the substrate, and the actuator reaches its closed position. Its actuation sequence is shown in Figure 3.3.

The internal stress can be the product of mismatches in the thermal expansion coefficients of different films or residual stress in either or both of the layers as discussed in Section 2.2. Usually both stress components can exist simultaneously, but in many cases one of them dominates.

The inchworm actuator can be designed using either type of internal stress. However, one should keep certain design constraints in mind. To obtain large tip displacements, either the thermal expansion coefficient mismatch must be large (for the first case) or the residual stress in either layer must be large (for the second case). In both cases, both layers, which the bimorph beam consists of, must be stiff enough to handle the large actuation, and to overcome high forces.

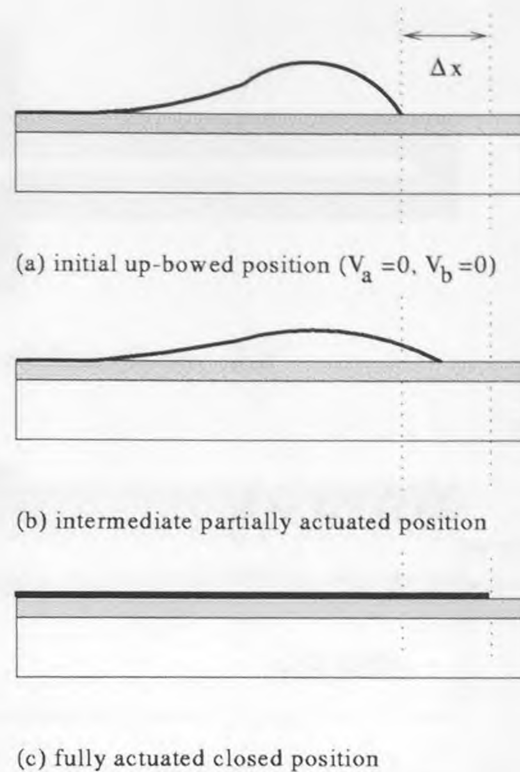

Figure 3.3 Actuation sequence illustration

To fulfill the first requirement for the first case one needs a material with high thermal expansion coefficient. Metals, even in thin film forms, usually have high thermal expansion coefficients, but thin films of almost all metals lack high stiffness.

Silicon nitride films are known to have high tensile residual stress. Although, as discussed in Section 2.4, the stress mechanism and the origin of this high stress are not understood well, one can control the stress in LPCVD silicon nitride layer, as long as the process parameters (temperature, gas flow rates etc.) are under control, and the deposition tube is clean. It was also shown that the residual stress in LPCVD nitride layers is temperature dependent and this dependence is linear in a large range of temperature [57].

In the rest of this chapter, an actuation based on temperature dependent residual stress will be discussed.

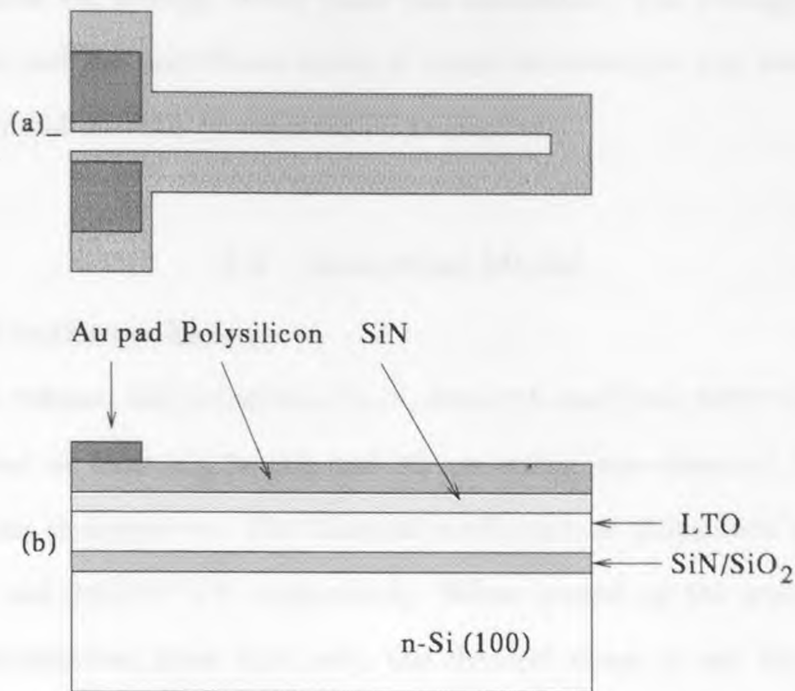

Figure 3.4 Schematic view: (a) top, (b) side.

The inchworm actuator under study, consists of a 1 μm thick, high doped polysilicon layer, which serves as the heater, and a 300 nm thick silicon nitride layer. The schematic view of the bimorph structure is shown in Figure 3.4. The insulation and HF-resistant layer consists of Si_3N_4/SiO_2 and 2 μm thick LTO serves as the sacrificial layer. The final release step is done by dipping the wafers into 49% HF for over 15 min.

The fabrication flow of the inchworm actuator is given in Appendix B.

The average stress in the thin films were measured from the warpage of 4" test wafers using the two-laser stress measurement technique as discussed in Section 2.5. First the warpage of the test wafer with the layer of interest was measured. Then that particular layer was removed chemically, The chemical etch process is believed to make only a small contribution to the stress level of the wafer. Finally, the warpage of the wafer was measured again and from the difference between the first and second

measured values the average stress value was calculated. The average stress in the silicon nitride and the polysilicon layers at room temperature was measured as 700 MPa (tensile) and 50 MPa (compressive), respectively.

3.2 Analytical Model

3.2.1 1D Cantilever Beam

Following the release, the polysilicon/Si_3N_4 bimorph cantilever bows up, and the tip of the actuator of 1000 μm length and 30 μm width was observed to move back 30 μm at room temperature. The thermal coefficients of polysilicon and Si_3N_4 are $2.3X10^{-6}/K$ and $2.6X10^{-6}/K$ respectively. When heated up the actuators became flat. The calculations show that only the thermal stress is not large enough to cause such a large displacement. (Detailed calculations for the tip displacement of a bimorph beam due to the thermal mismatch will be given in Chapter 4.)

A model to describe the thermal actuation is given here, where 1D beam equations are utilized. Internal stresses are assumed to be linearly dependent to temperature. It has been demonstrated that for the nitride layer with the dominating stress value, the stress is linearly temperature dependent over a wide temperature range, while for polysilicon layer, this is an approximation [57, 58]. With this assumption, the average stress is defined by

$$\sigma(T) = \frac{\sigma_o\, T}{T_o - 25} - \frac{\sigma_o\, T_o}{T_o - 25} \quad [MPa], \tag{3.1}$$

where σ_o is the stress value measured at room temperature, and T_o is the temperature, where the average stress is zero. From the orange color of the polysilicon beam, the temperature was estimated as 625°C. Using these numerical values, we obtain the following equations for polysilicon and nitride layers:

$$\sigma_{poly}(T) = \frac{-50\ T}{600} + 52.08 \quad [MPa], \tag{3.2}$$

$$\sigma_{nitride}(T) = \frac{700\ T}{600} - 729.17 \quad [MPa]. \tag{3.3}$$

The 1D model of the bimorph actuator is shown in Fig. 3.5, where the principle of superposition can be used as long as the problem is linear. (How to deal with nonlinearities will be discussed later in this section.) Then the total tip deflection is the algebraic sum of the tip deflection in both cases.

Figure 3.5 1D Cantilever beam model.

The cross-section of the cantilever beam is shown in Fig 3.6. The device dimensions and material properties of the cantilever are summarized in Table 3.1.

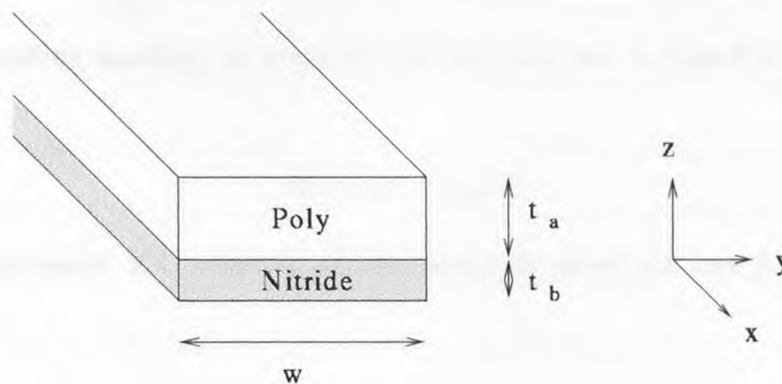

Figure 3.6 Cross-section of the bimorph cantilever beam.

The geometric centroid (z_c) and force centroid (z_{cc}) (the point where an equivalent force can be applied without inducing a rotational moment) can be computed as follows:

Table 3.1 Thin film dimensions and stress properties

Layer name	Width (μm)	Thickness (μm)	Thermal expansion coefficient [10^{-6}/K]	Young's modulus [MPa]	Residual stress [MPa]
Polysilicon	50	1	2.4	160	50 (comp.)
Si_3N_4	50	0.3	2.6	300	700 (ten.)

$$z_c = \frac{(w\ t_a\ (\frac{t_a}{2} + t_b)) + (\frac{E_b}{E_a}\ w\ t_b\ \frac{t_b}{2})}{(w\ t_a) + (t_b\ w\ \frac{E_b}{E_a})}, \tag{3.4}$$

$$z_{cc} = \frac{\frac{\sigma_{poly}}{2}\ w\ {t_a}^2 + \frac{\sigma_{nitride}}{2}\ w\ {t_b}^2}{F}, \tag{3.5}$$

where F is force for the cross-section of the beam, and is defined by [59]

$$F = \int_A \sigma\ z\, dA = (\sigma_{poly}(T)\ w\ t_a) + (\sigma_{nitride}(T)\ w\ t_b). \tag{3.6}$$

The resulting bending moment for the cross-section is therefore

$$M = (z_c - z_{cc})\ F \tag{3.7}$$

The equivalent EI property of the bimorph structure can be calculated as follows: [60]

$$EI = \frac{w\ t_b^3\ t_a\ E_a\ E_b\ K}{12\ t_a\ E_a + t_b\ E_b}, \tag{3.8}$$

where the stiffness factor K is defined by

$$K = 4 + 6\ \frac{t_a}{t_b} + 4\ \left(\frac{t_a}{t_b}\right)^2 + \frac{E_a}{E_b}\left(\frac{t_a}{t_b}\right)^3 + \frac{E_b}{E_a}\frac{t_a}{t_b}. \tag{3.9}$$

Using the equivalent EI, the displacement of any point on the cantilever beam in the x and z direction can calculated by the following equations:

$$u_x(x) = \frac{M^2\ (\frac{x^3}{3} - \frac{0.75\ x^4}{L} + \frac{0.45\ x^5}{L^2})}{8\ EI^2}, \tag{3.10}$$

$$u_z(x) = \frac{M\ (\frac{x^2}{2} - \frac{x^3}{2\ L})}{2\ EI}. \tag{3.11}$$

The equation for the vertical force at the tip is as follows:

$$R = F_z = \frac{3\ M}{2\ L}, \tag{3.12}$$

The horizontal force at the tip can be calculated from $F_z(L)$ and rotation at the tip $\theta(L)$:

$$F_x = \frac{F_z}{\tan\ \theta}\ , \tag{3.13}$$

$$\theta(L) = \frac{-M\ L}{4\ EI}. \tag{3.14}$$

The calculated values (according to the analytical model given in this section) for x and y displacement of the inchworm actuator were used to construct the up-bowed actuator at room temperature (Figure 3.7). These values can be extrapolated to obtain a 3D shape (Figure 3.8). The calculated lateral tip displacement variation with temperature is compared with the results obtained from FEA simulations Figure 3.13. The $\pm$ 5% uncertainty from the stress measurement setup was included into the calculated results by errorbars.

3.2.2 Validity of the Analytical Model

The 1D formulas used in this model are based on some assumptions, which are listed in Ref [60] in detail. The one, which assumes that the beam is straight or nearly so, must be considered very carefully. If the beam is curved, the curvature must be in the plane of bending and the radius of curvature must be at least 10 times the depth.

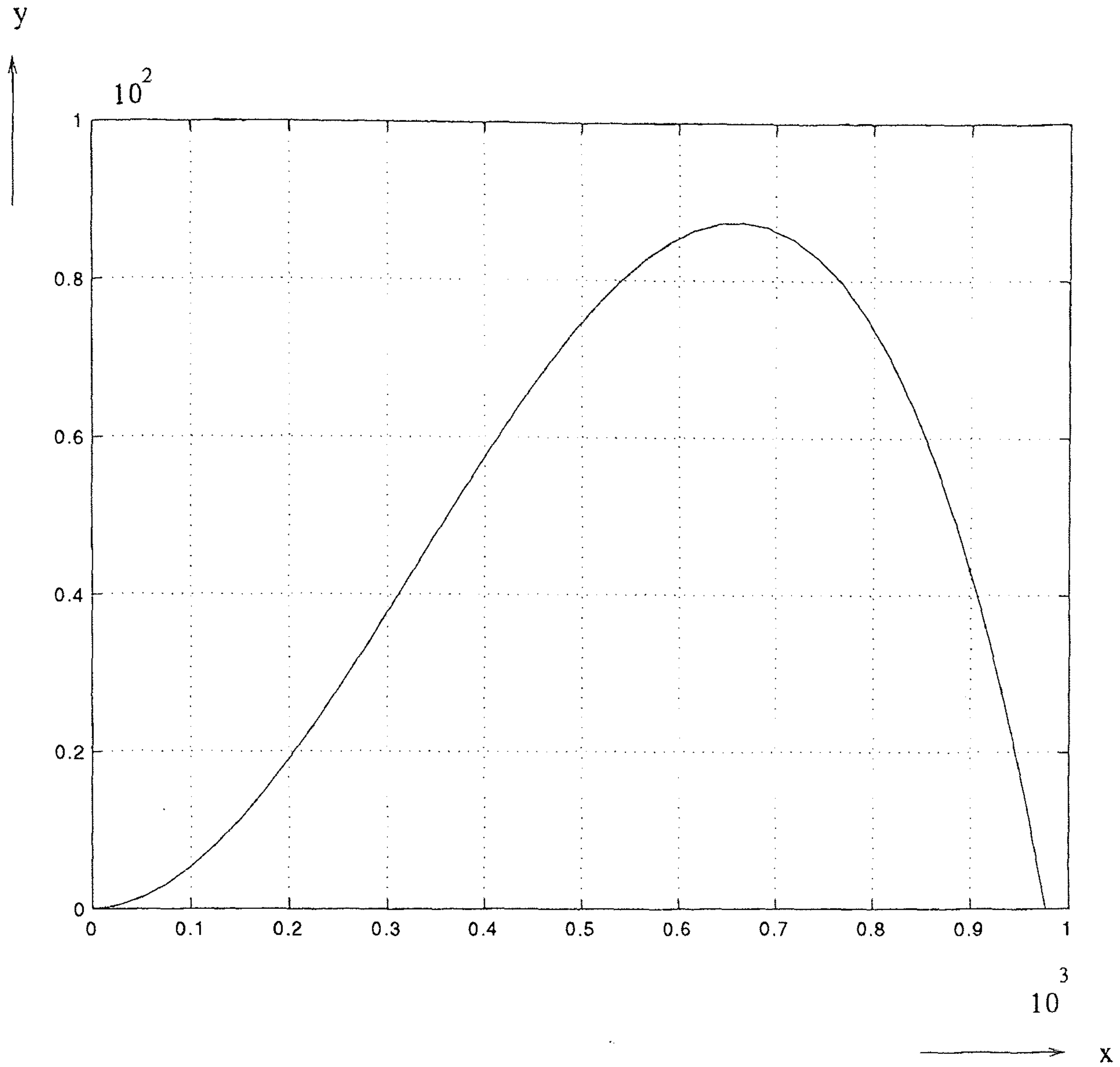

Figure 3.7 The 2D shape of the up-bowed actuator at room temperature constructed from the analytical model (dimensions are in micron).

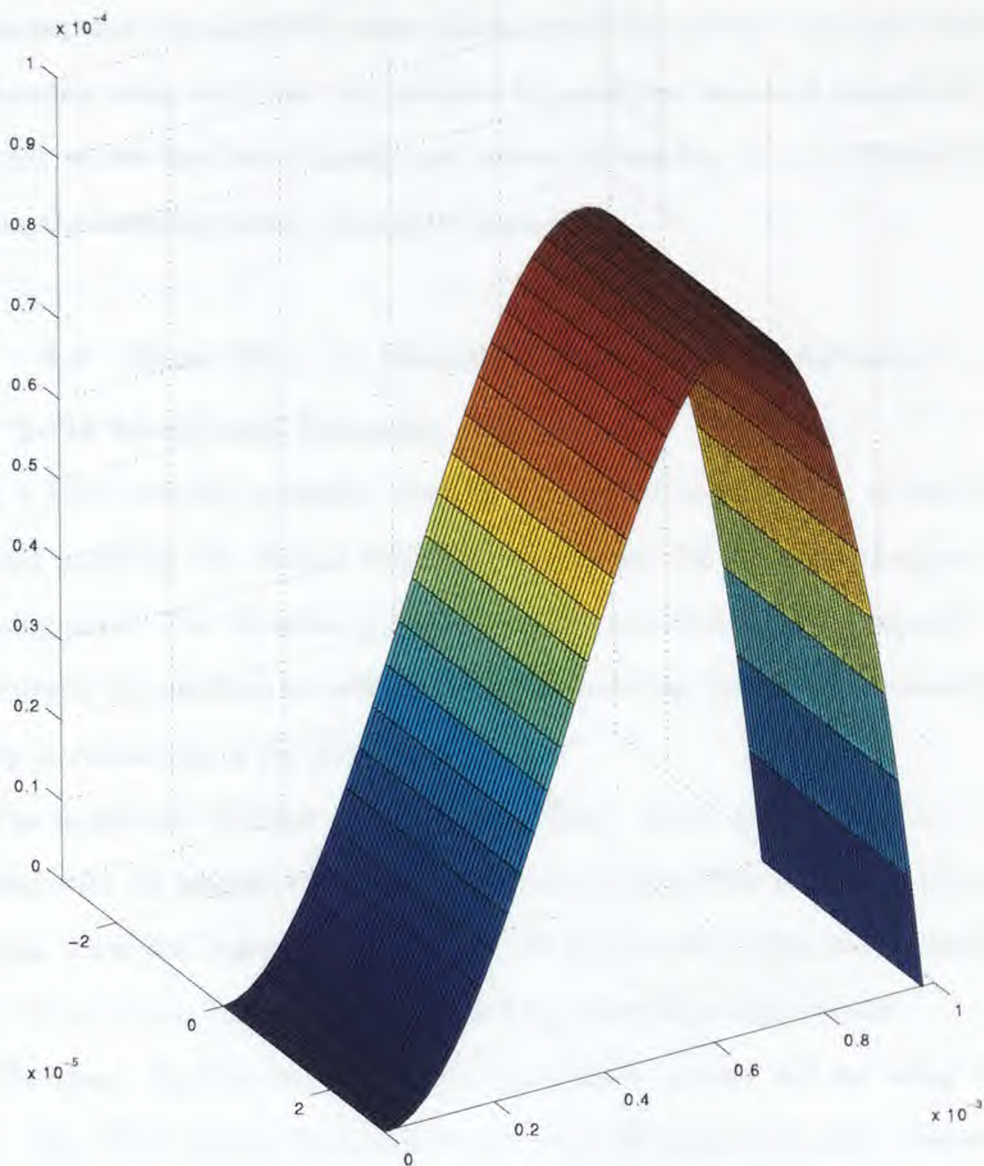

Figure 3.8 The 3D shape of the up-bowed actuator at room temperature constructed from the analytical model

The inchworm problem discussed in this work is at the limit of this assumption, any decrease in the layer thicknesses or any increase in internal stresses will cause such a curvature, that the cantilever beam cannot be considered as a straight beam.

Another case, which can not be modeled with the proposed analytical model, is the one, where the beam buckles up instead of bending in a controlled way. In this case, the buckling theory should be applied.

3.3 Finite Element Modeling of the In-Plane Actuator

3.3.1 Solid Model and Boundary Conditions

During a finite element analysis, creating a complete solid model, an appropriate mesh and applying the correct boundary conditions are the most designer's time consuming parts. The duration of the next step, computation time, depends on the complexity of the problem as well as on the platform the simulation is running. The last step is evaluation of the simulation results.

The inchworm actuator is a cantilever beam, whose total thickness (1.3 μm) compared with its length (1 mm) is very small (almost 1000 times), so the error is negligible, when the beam is represented with a 2D model. The width-length ratio is 1:33, which means that even a 1D model can give reasonable results.

The static thermal and structural simulations carried out by using ANSYS ver5.3. The FEA results of a solid model with 3D structural solid element with rotations SOLID73, and with 2D structural layered element SHELL91, didn't show any significant difference, so the remaining simulations are carried out with 2D model. Although SHELL91 is 2D element, layer thicknesses has to be included into the model as *Real Constants* (zero-thickness layers are not allowed), and it allows nonlinear analysis, which is another advantage of this element type. This element has 6 degrees of freedom at each node: transitions in x, y, and z directions and rotations about the nodal x, y and z axes.

Applying the displacement boundary conditions is straight forward. The cantilever beam is clamped at one end. All the nodes at this end have zero-displacement and zero-rotation constraints. When the $1\mu m$ thick sacrificial oxide layer is removed at room temperature, the tip touches the substrate and moves on it all the way till the rest point. The nodes at the tip are constraint in y direction and have a fix displacement value -1 μm. The mesh of the model with displacement boundary conditions applied is shown in Figure 3.9.

Internal stress needs to be introduced at the next step. The limitations of applying internal stress to the solid model directly is discussed in Appendix D. Indirect way, of applying internal stresses to the solid model, is to apply both the thermal and residual stresses as thermal stress to the model.

If the thermal expansion coefficient mismatch causes the internal stress, the designer just needs to apply the temperature, which brings the structure into balance (zero stress condition), as a boundary condition to the model.

If the residual stress is dominating, which is the case here in the inchworm actuator, again the internal stress is introduced as thermal stress [61], but the fictive thermal expansion coefficients need to be calculated. The fictive thermal expansion coefficients were chosen so that 1 °C change corresponded to 1 MPa of thermal stress in polysilicon layer. The applied thermal stress in the freed structure corresponds to a stress in the not yet freed structure that is a factor $1/(1\text{-}\nu)$ larger, and that was taken into account. The Poisson's ratio for both polysilicon and Si_3N_4 was chosen as ν = 0.25. The calculated fictive thermal expansion coefficients are α_{poly}=3.53X10^{-6} 1/°C and $\alpha_{Si_3N_4}$=32.3X10^{-6} 1/°C.

3.3.2 Simulation Results

After the internal stress was included into the model, the model was solved. When the results were examined, the displacement in x direction at the tip was found

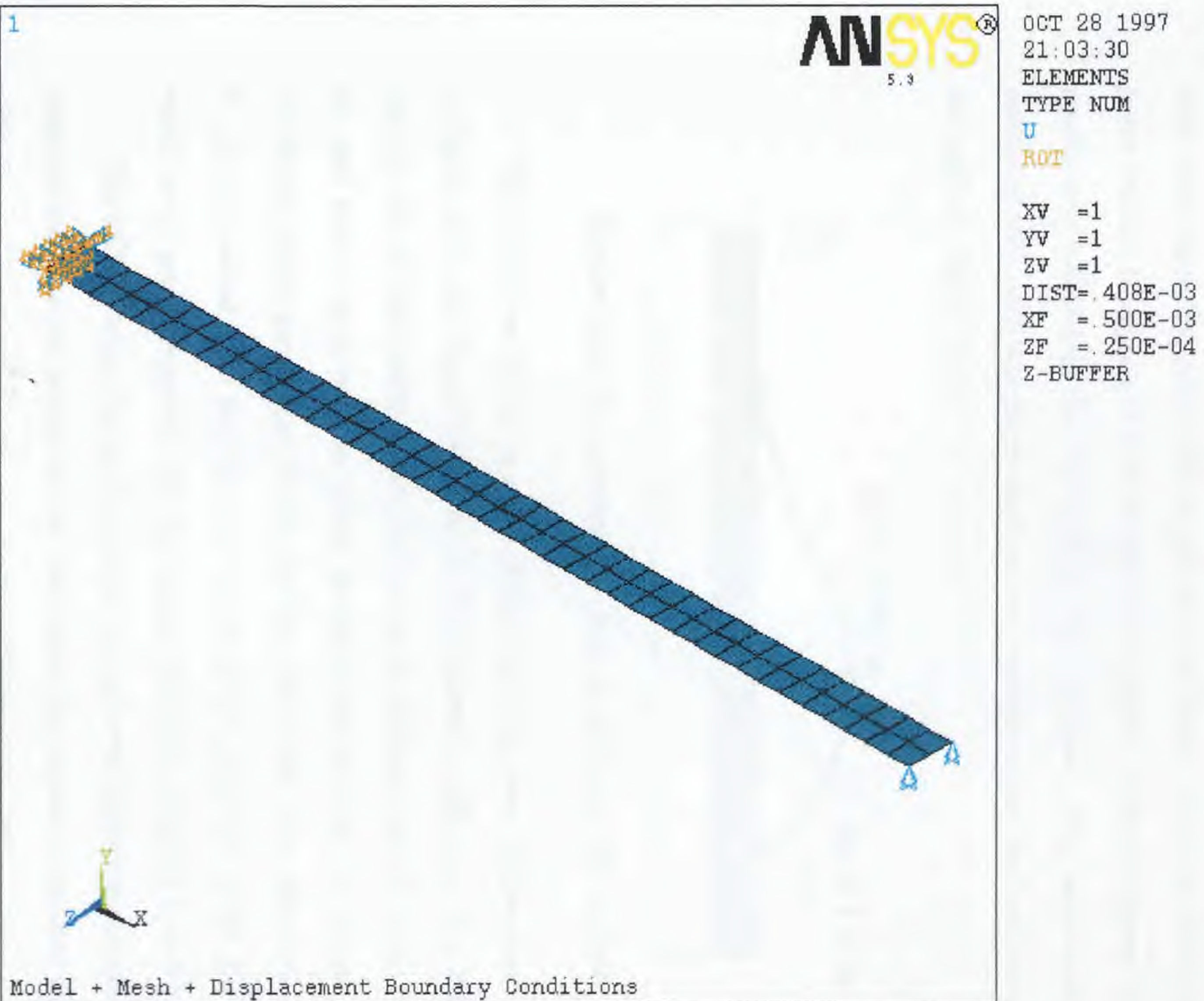

Figure 3.9 Solid model of the inchworm actuator, meshed and with displacement boundary conditions applied

to be less than 1 μm, while the curvature of the beam was very large and the maximum displacement in y direction was more than 400 μm, which was indicating a questionable result set (Figure 3.10). Simple calculations showed that the beam must have expanded about 20% to get the final shape. The huge expansion of the beam couldn't be explained with the thermal expansion coefficients given above. The results were indicating, that the problem was nonlinear. The same model was re-simulated with nonlinear (large displacement) option on, and the load (temperature) was applied step by step.

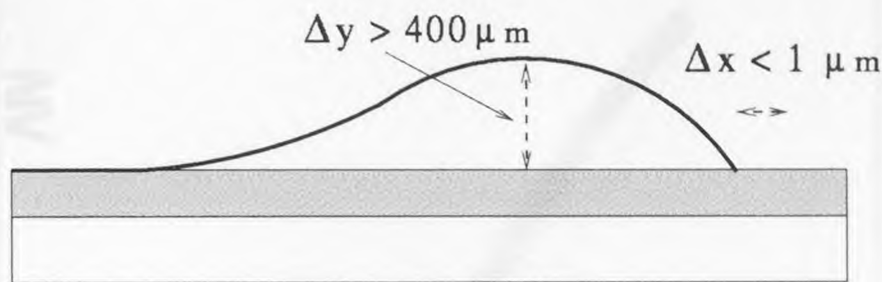

Figure 3.10 The questionable result set of linear FEA analysis

The simulation results (x and y displacements at room temperature) are given in Figure 3.11 and Figure 3.12. The 1D FEA showed a difference of $< 2\%$ between the 1D and 2D simulation results, and it can be inferred that 1D beam model can be used with a small error to model the inchworm actuator. In Figure 3.13, the calculated results are compared with the FEA 2D results. The difference is ≈ 5 % . It can be inferred, that for this case the proposed analytical model gives results, which are in good agreement with the numerical results obtained from FEA.

The SEM picture (Figure 3.14) shows the upbowed inchworm actuator at room temperature. The test results for the case, where the inchworm actuator was excited with thermal input power only, are shown in Figure 3.15. [62].

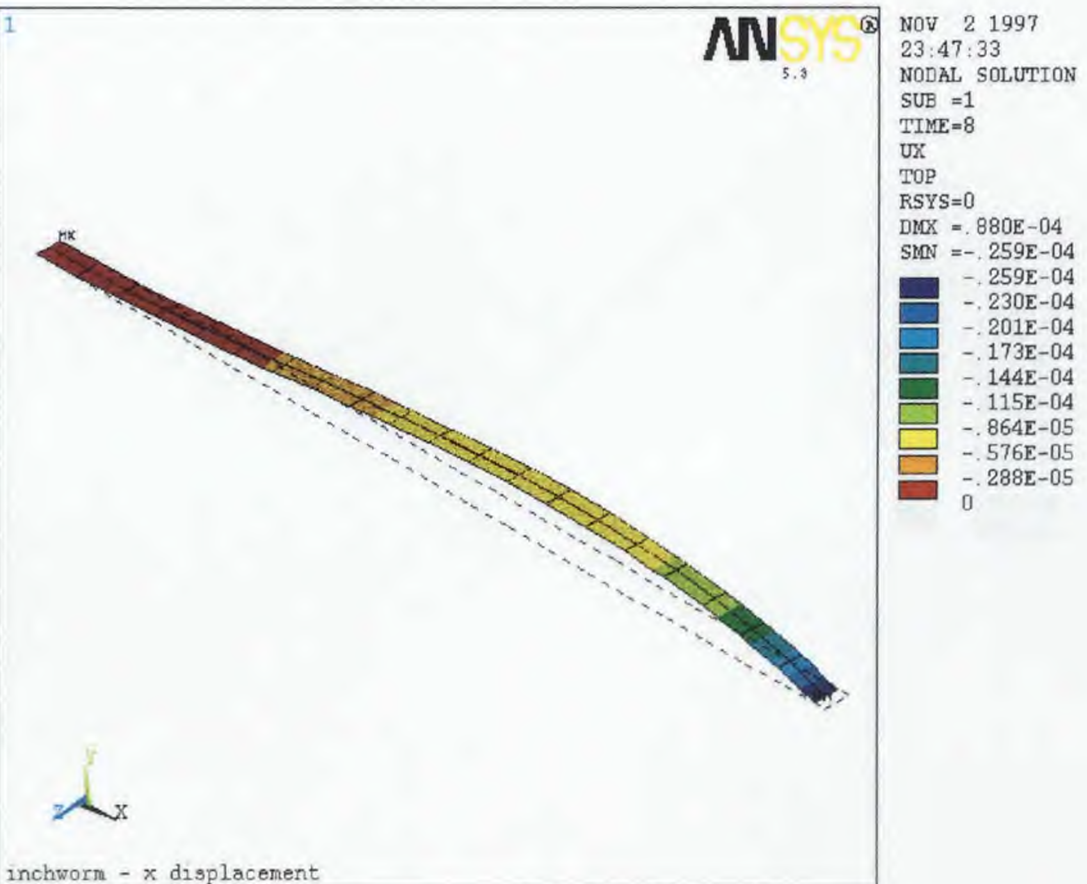

Figure 3.11 The displacement in horizontal direction throughout the cantilever at room temperature.

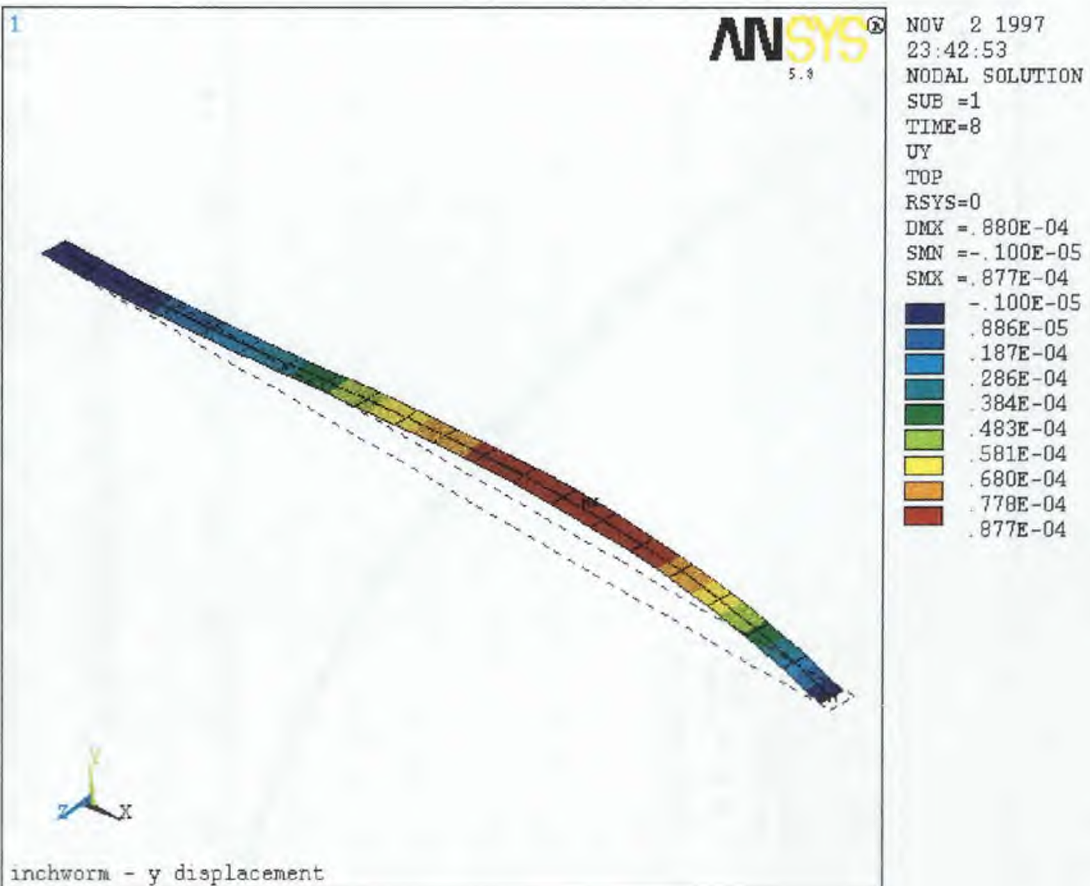

Figure 3.12 The displacement in vertical direction throughout the cantilever at room temperature.

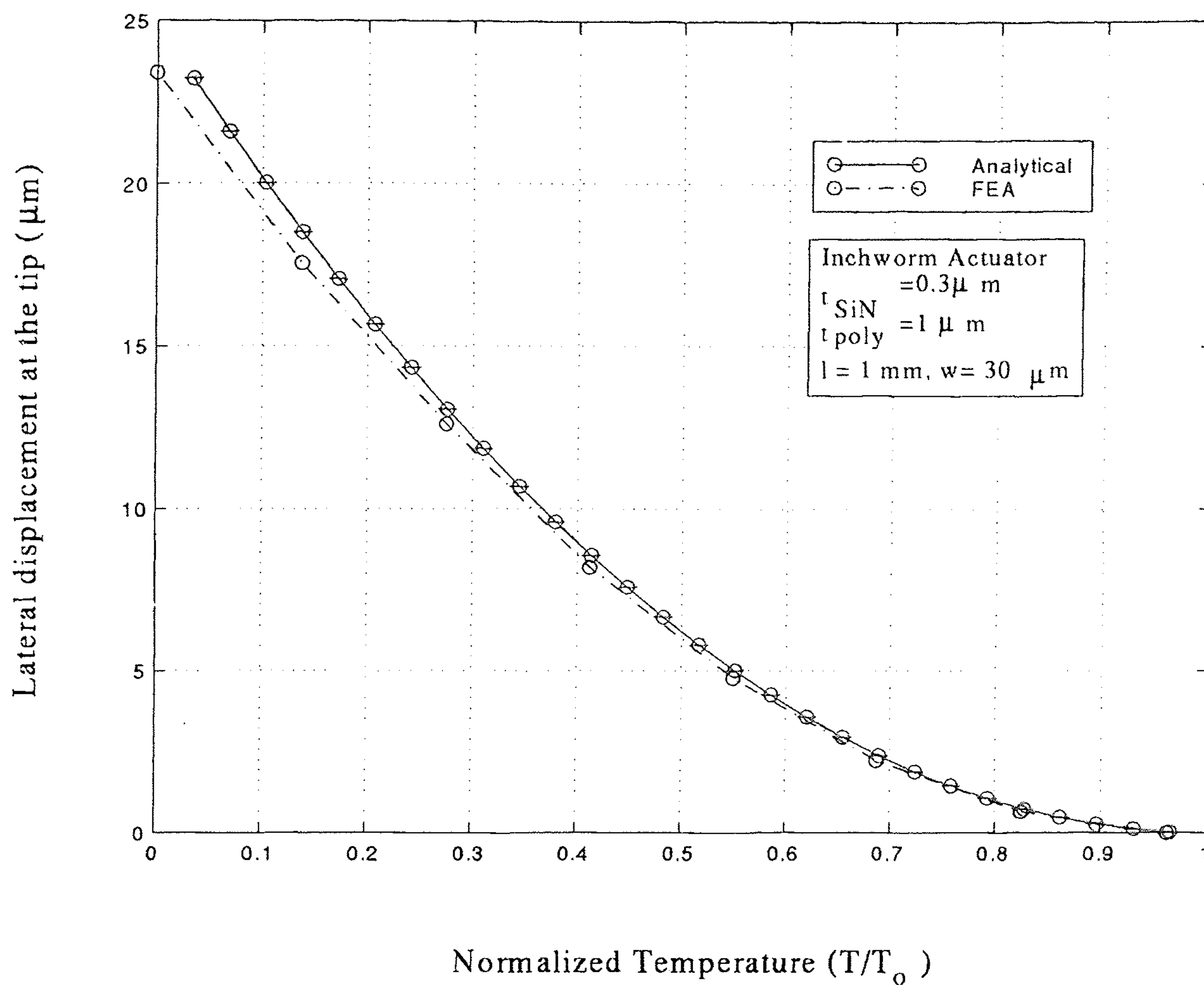

Figure 3.13 Tip displacement of the inchworm actuator vs. normalized temperature: Calculated and FEA results.

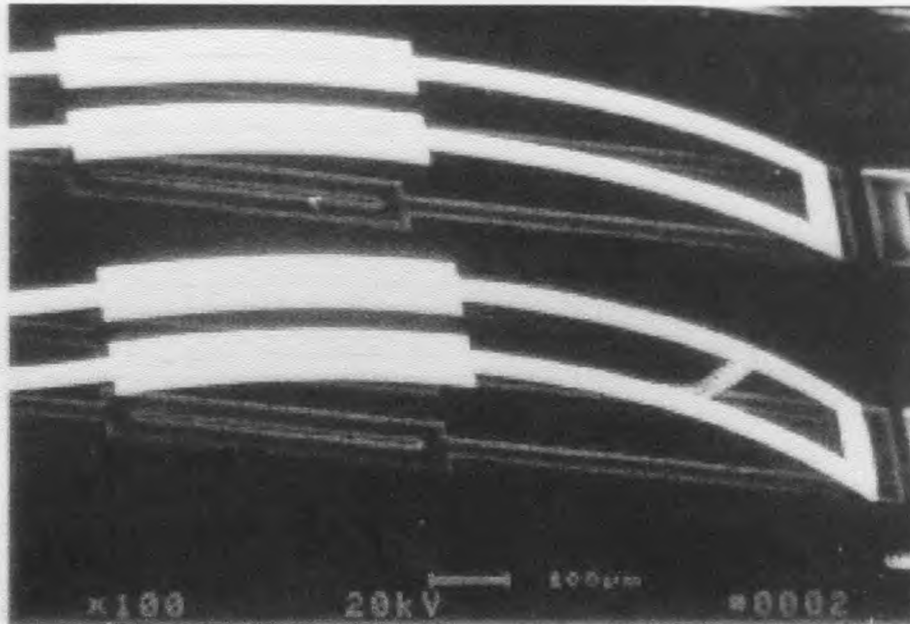

Figure 3.14 SEM picture of the up-bowed actuator.

3.4 Two-segment Bimorph Structure

Neither the FEA, nor the analytical model given in the previous sections includes the friction at the tip. This friction occurs due to the vertical force at the tip, which pushes the tip towards the substrate. The test results for the case, where the inchworm actuator was excited with thermal input power only, are shown in Figure 3.15. [62]. It can be seen from this figure clearly, that the differing nature of the friction at the tip during back and forth movement of the tip causes hysteresis. The surface topology may effect the lateral actuation. Test have shown that a rough surface like the one of a polysilicon layer can alter the actuation dramatically and even prevent a smooth motion. The variation of the calculated horizontal and vertical force with temperature is shown in Figure 3.16. If the vertical force at the tip is minimized or the interaction of the tip with the substrate is prevented, the friction can be avoided. To do so, a 2-segment bimorph actuator design can be used. As shown in Figure 3.17 (a), the cantilever beam is made of 3 types of materials. The cantilever

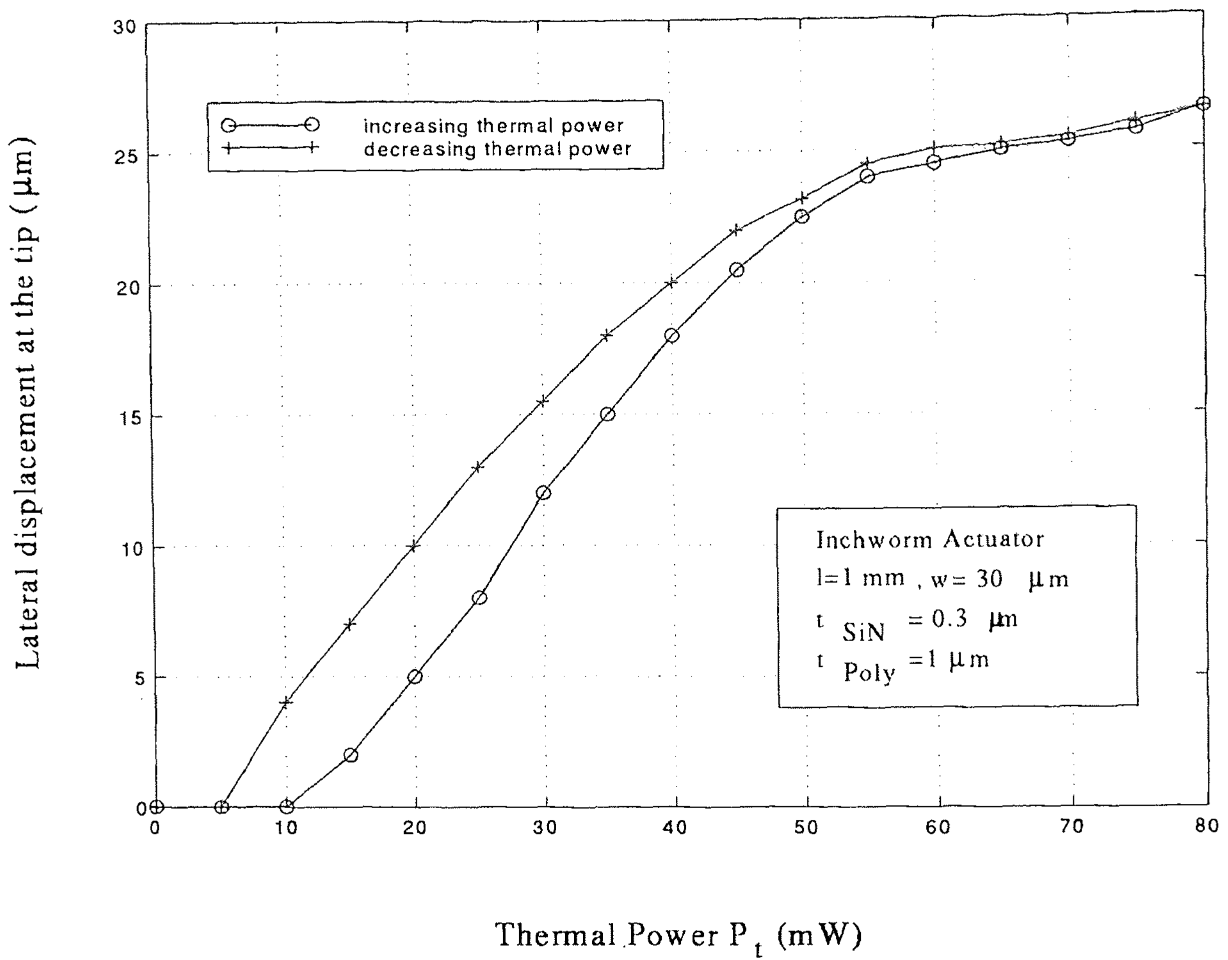

Figure 3.15 Measured lateral tip displacement as a function of input power for thermal actuation without electrostatic excitation (V_b)

is balanced at high temperature and when it is released at room temperature, it gets the shape shown in Figure 3.17 (b). The materials, the layer thicknesses and the length of each segment (l_1 and l_2) can be chosen in such a way, that there is a small separation (h) between the tip of the actuator and the substrate. As an example, metals with a large thermal expansion coefficients can be chosen as material # 1 and # 3 and LTO as material # 2. In this case, the stray stresses in the structure are mainly due to the thermal expansion coefficient mismatch (this topic will be discussed in detail in Chapter 4). The material properties of candidate materials are given in Table 3.2 [1]. The meshed solid model of the two-segment actuator is shown in Figure 3.18. The segment lengths l_1 and l_2 are both 430 μm and the width of each beam is 8 μm. The blue elements are bimorph structures consisting of material # 1 and # 2, the purple elements are bimorph structures consisting of material # 2 and # 3, and the red elements are monomorph and have the material properties of material # 2. The two-segment simple cantilever and the two-segment full actuator structure were simulated for three cases with varying l_2/l_1 ratio ($l_1+l_2=860\mu m$). The material information and the dimensions are summarized in Table 3.3. The simulation results for the cantilever beam are summarized in Table 3.4, and are plotted in Figure 3.19, Figure 3.20, and Figure 3.21. Negative g in the table means, that the tip is below the surface under these particular simulation conditions. The tip displacements of the full two-segment actuator structure (Figure 3.18) with varying l_2/l_1 ratio ($l_1+l_2=860\mu m$) obtained from FÈA are summarized in Table 3.5 and plotted in Figure 3.22, Figure 3.23, and Figure 3.24. (The temperature difference ΔT was 200°C.)

The gap between the tip and the surface (g) is a very important parameter. Its value has to be as close to zero as possible. The designer has to pick the l_2/l_1

[1]Thermal expansion coefficients and Young's Moduli listed in Table 3.2 have been taken from MEMS Clearinghouse, MEMS Material Database (http://mems.isi.edu), except the values for $TaSi_2$, which have been taken from [63]

ratio from the g vs. l_2/l_1 curves where g is zero, if he wants to minimize the friction between the tip and the surface. The segments can be driven separately. A dc voltage can be applied to the first segment of the actuator. when the first segment heats up and the tip comes close to the surface. Then by applying a signal to the second segment of the actuator, the horizontal actuation at the tip is obtained.

The frequency analysis of the two-segment bimorph actuator with the segment lengths $l_1=l_2$ was performed using ANSYS. The deformed shaped at the first and second modal frequencies are given in Figure 3.25 and Figure 3.26, respectively. The modal frequencies for three cases are given in Tabel 3.6.

Table 3.2 Material Properties of candidate materials for two-segment actuator

Layer name	Thermal expansion coefficient [10^{-6}/K]	Young's modulus [MPa]	Poisson's Ratio
Polysilicon	2.4	160	0.22
LTO	0.4	74	0.22
Aluminum	23	69	0.3
$TaSi_2$	8.8	111	0.3
Gold	14.3	80	0.3

Table 3.3 Material information, dimensions of the simulated two-segment bimorph cases.

Case # 1		Case # 2		Case # 3	
M_1: Gold	t_1= 0.5 μm	M_1: Al	t_1= 0.4 μm	M_1: $TaSi_2$	t_1= 0.5 μm
M_2: LTO	t_2= 1.5 μm	M_2: LTO	t_2= 1.5 μm	M_2: LTO	t_2= 1.5 μm
M_3: Gold	t_3= 0.5 μm	M_3: Gold	t_3= 0.5 μm	M_3: Gold	t_3= 0.5 μm

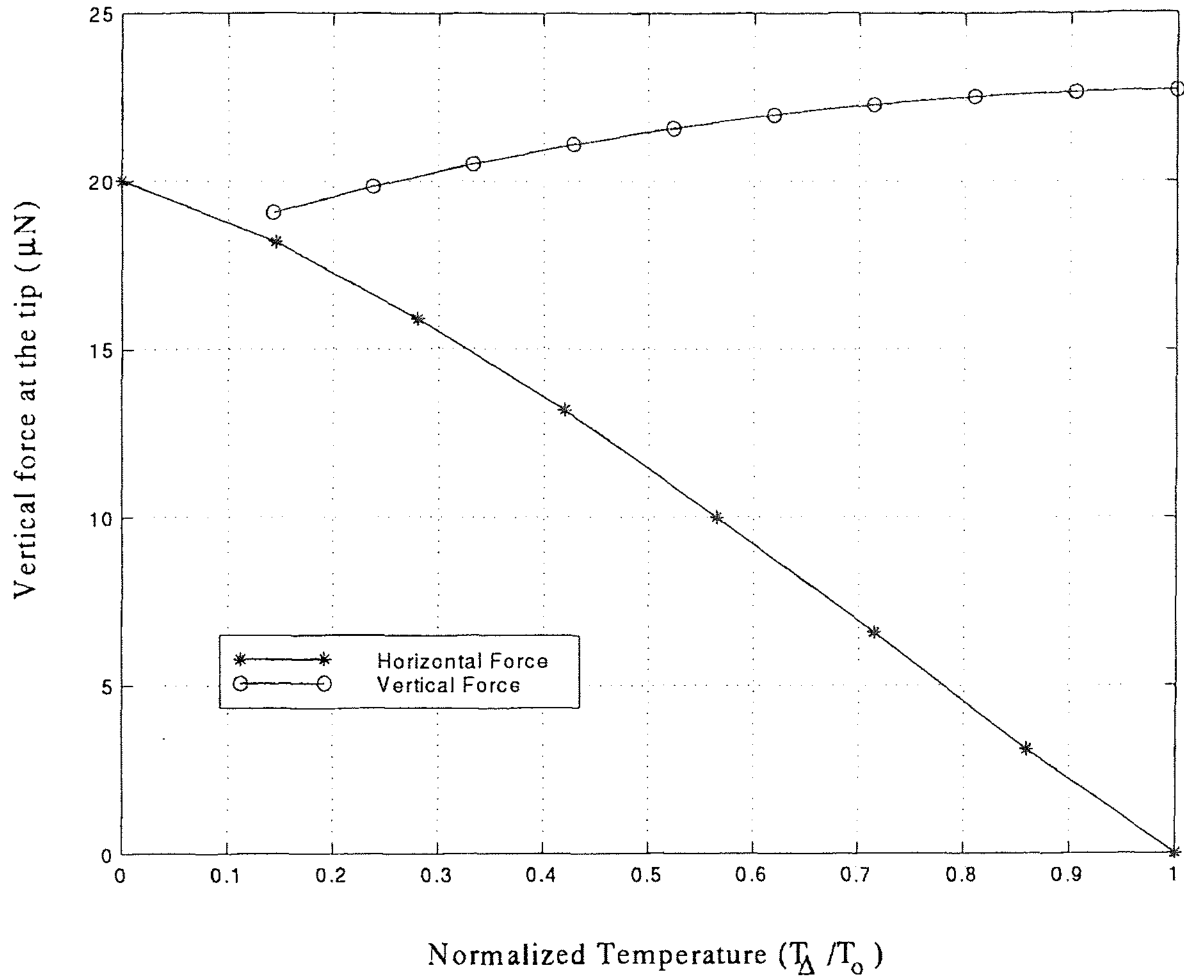

Figure 3.16 The calculated horizontal and vertical force at the tip of the actuator as a function of temperature. When temperature increases, the actuator flattens out and the tip moves forward (T_o=625°).

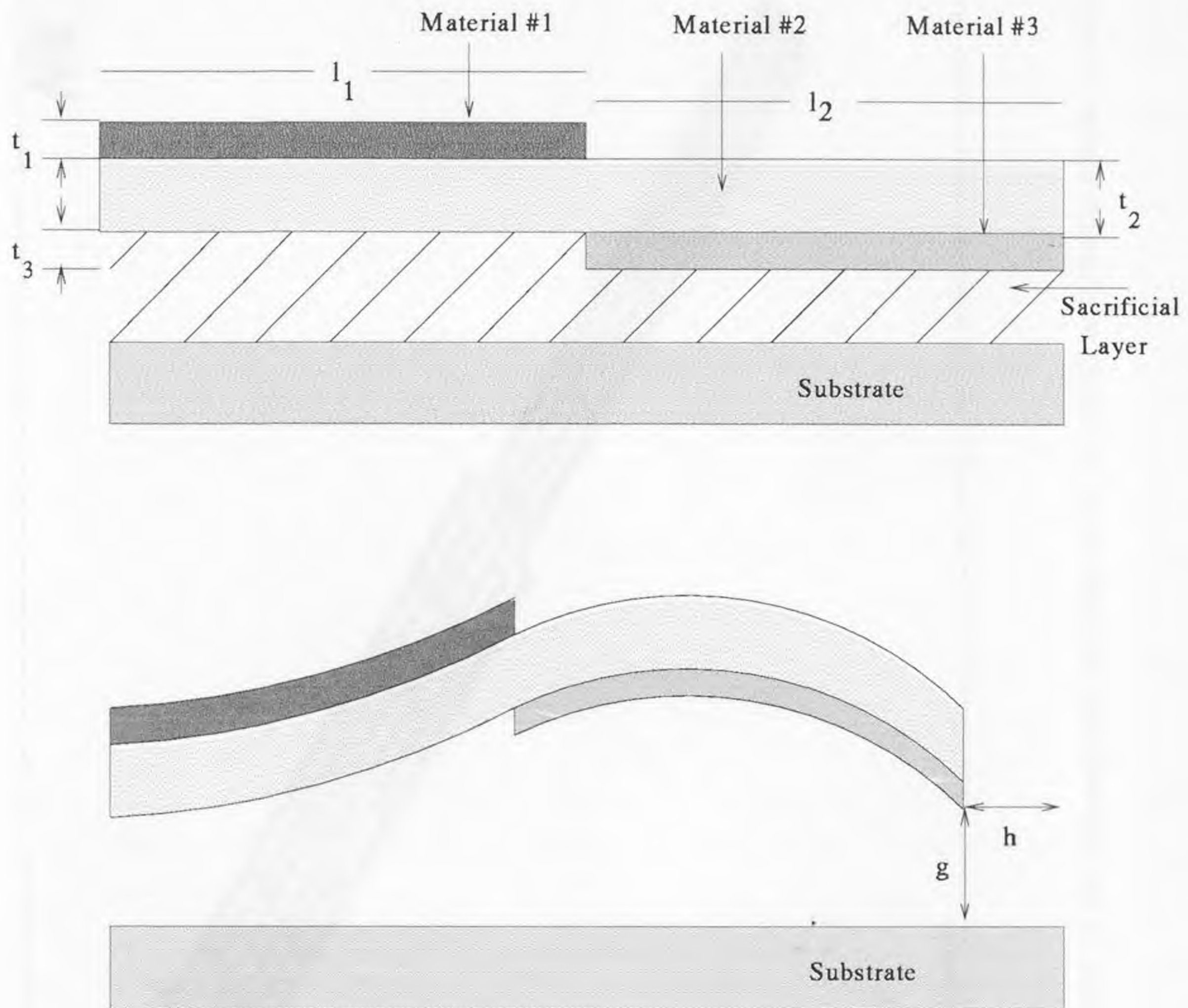

Figure 3.17 Two-segment bimorph actuator: (a) Before sacrificial layer release (b) After sacrificial layer release.

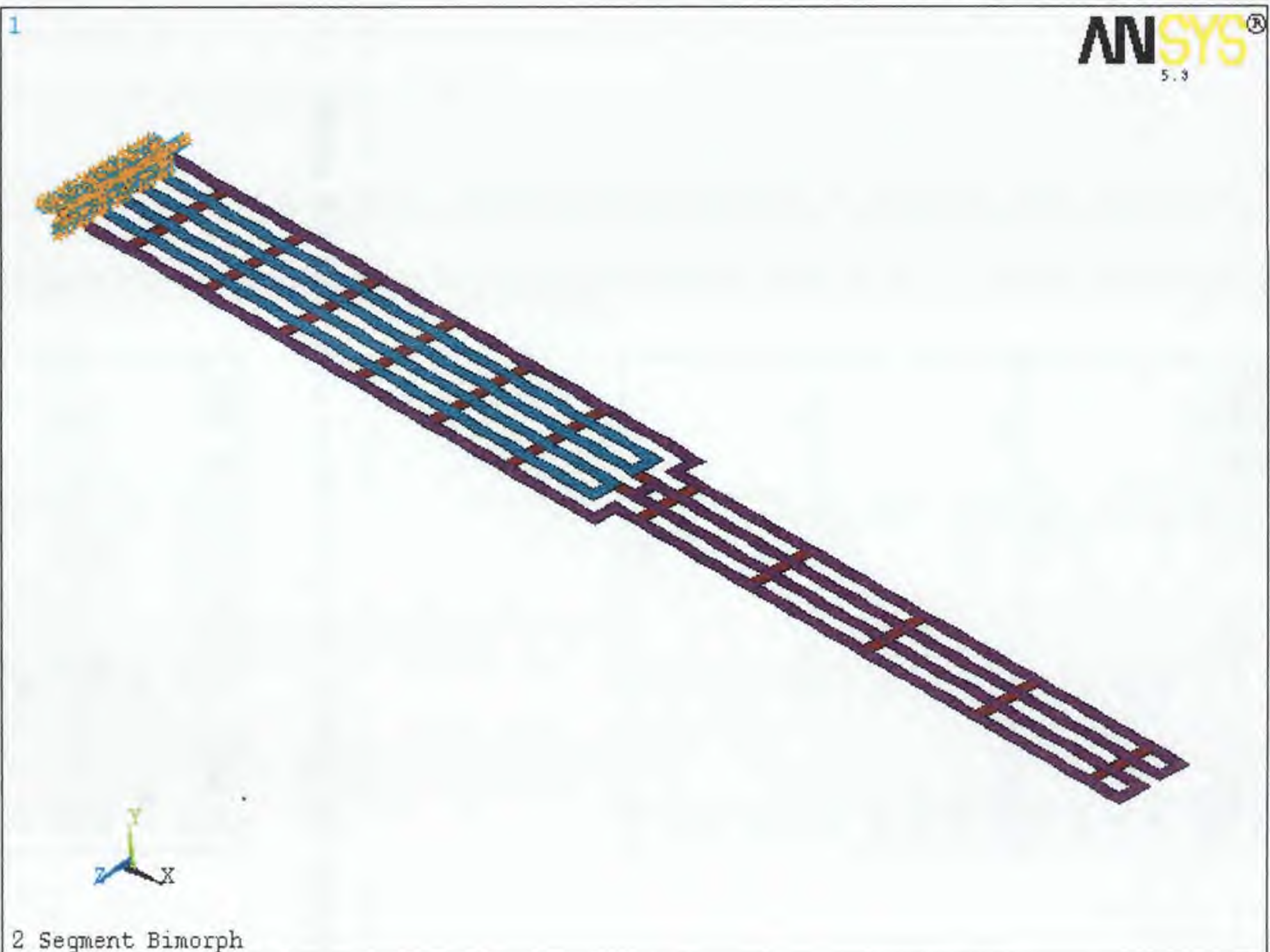

Figure 3.18 Solid model of the two-segment actuator with the mesh and displacement boundary conditions

Table 3.4 Simulation results for the two-segment cantilever beam.

Case #	l_2/l_1	g (μm)	h (μm)
1	0	511	256
	0.33	474	192
	1	292	70
	1.87	92	32
	2.58	-17	36
2	0	612	480
	0.33	612	390
	1	462	170
	3	46	39
	3.53	-15	42
3	0	362	112
	0.33	312	75
	1	138	26
	1.87	-28	30
	2.07	-57	34

Table 3.5 Simulation results of the two-segment full actuator structure.

Case #	l_2/l_1	g (μm)	h (μm)
1	0.55	-84	10
	1	-41	16.7
	1.83	-165	50
2	0.55	174	26
	1	16	14
	1.83	-123	40
3	0.55	-8	-7
	1	-108	-25
	1.83	-217	65

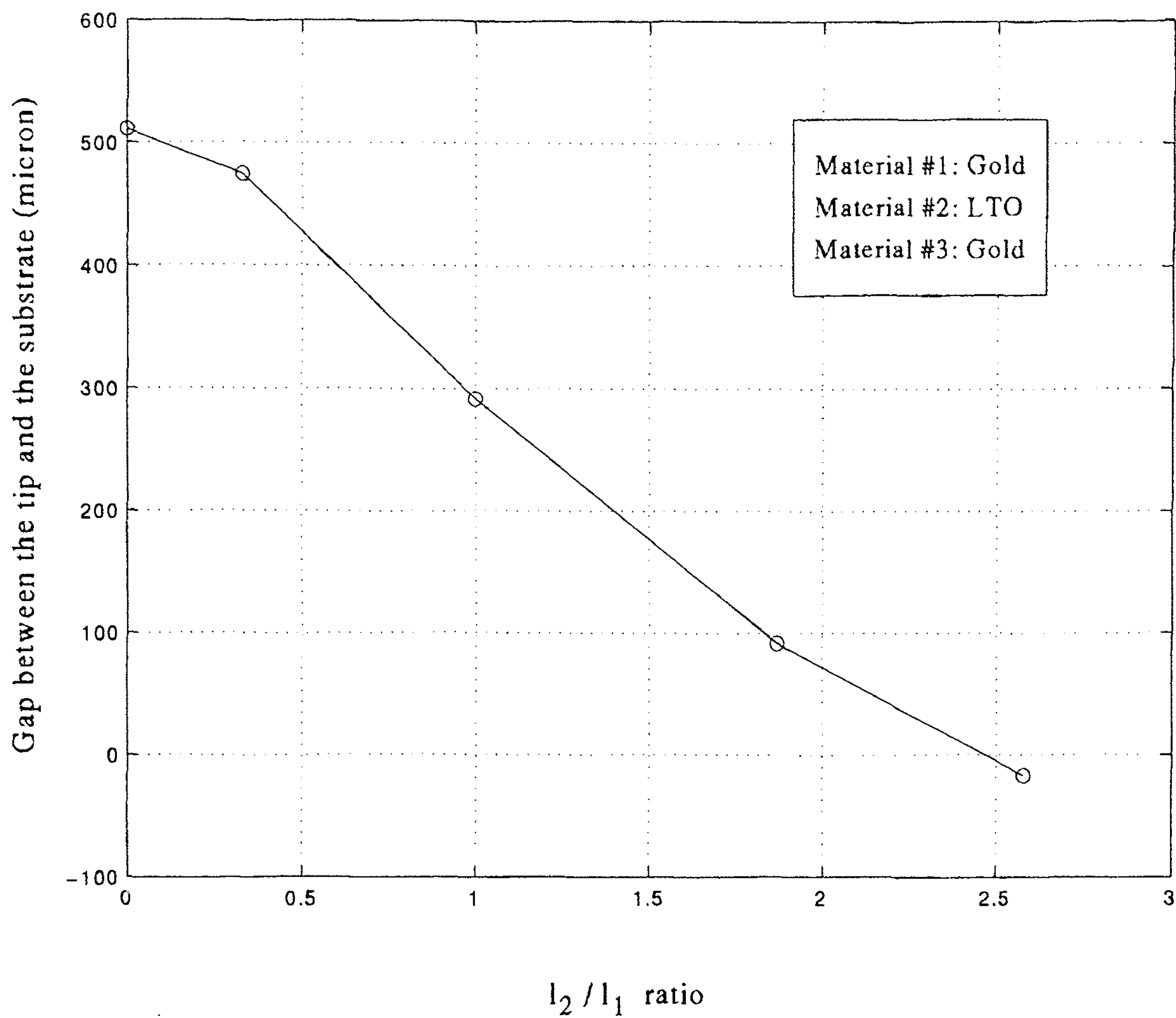

Figure 3.19 Simulation results of the two segment bimorph cantilever beam: Case # 1

Table 3.6 Simulated modal frequency values. (l_1=l_2=430μm)

Case #	Mode # 1 (Hz)	Mode # 2 (Hz)
1	2213	11504
2	2116	12124
3	2295	12386

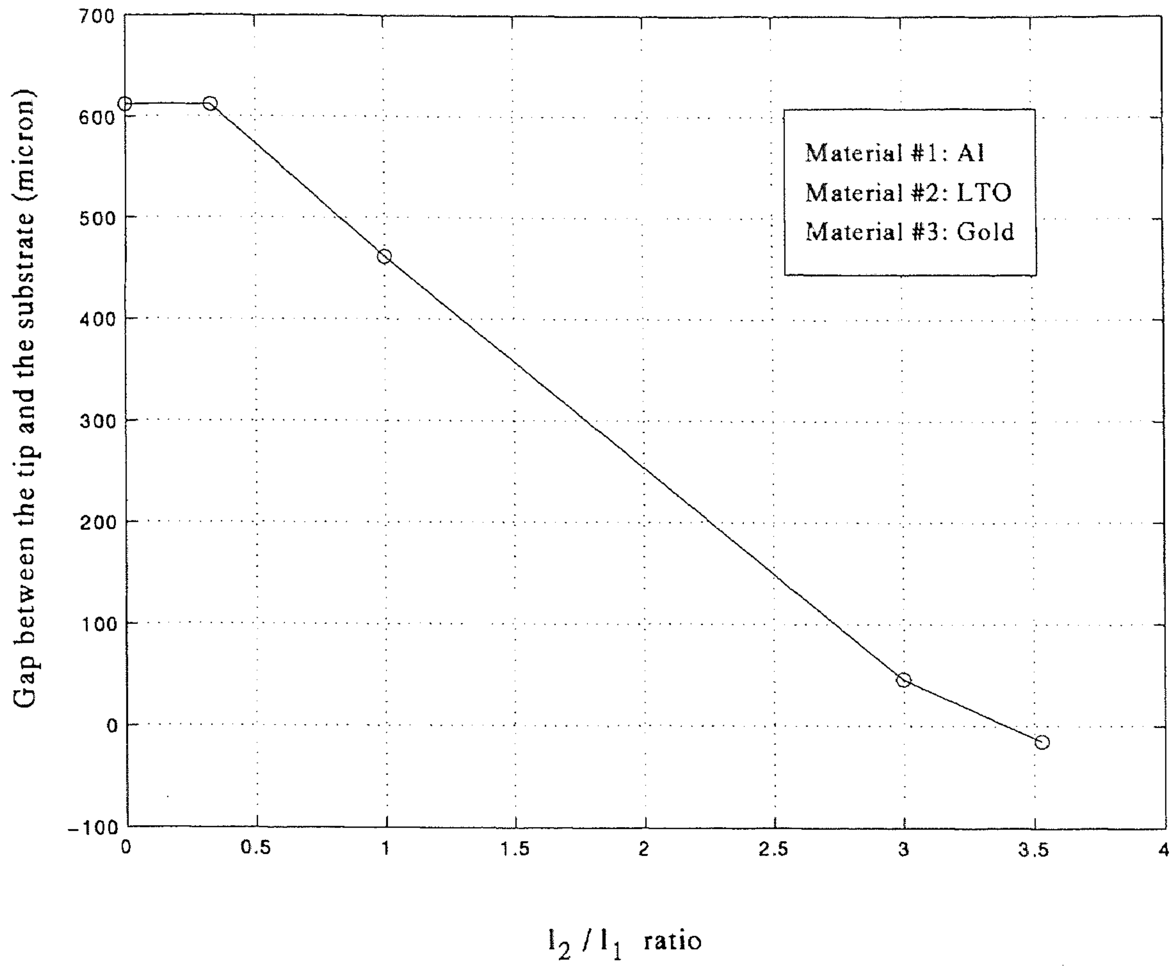

Figure 3.20 Simulation results of the two segment bimorph cantilever beam: Case # 2

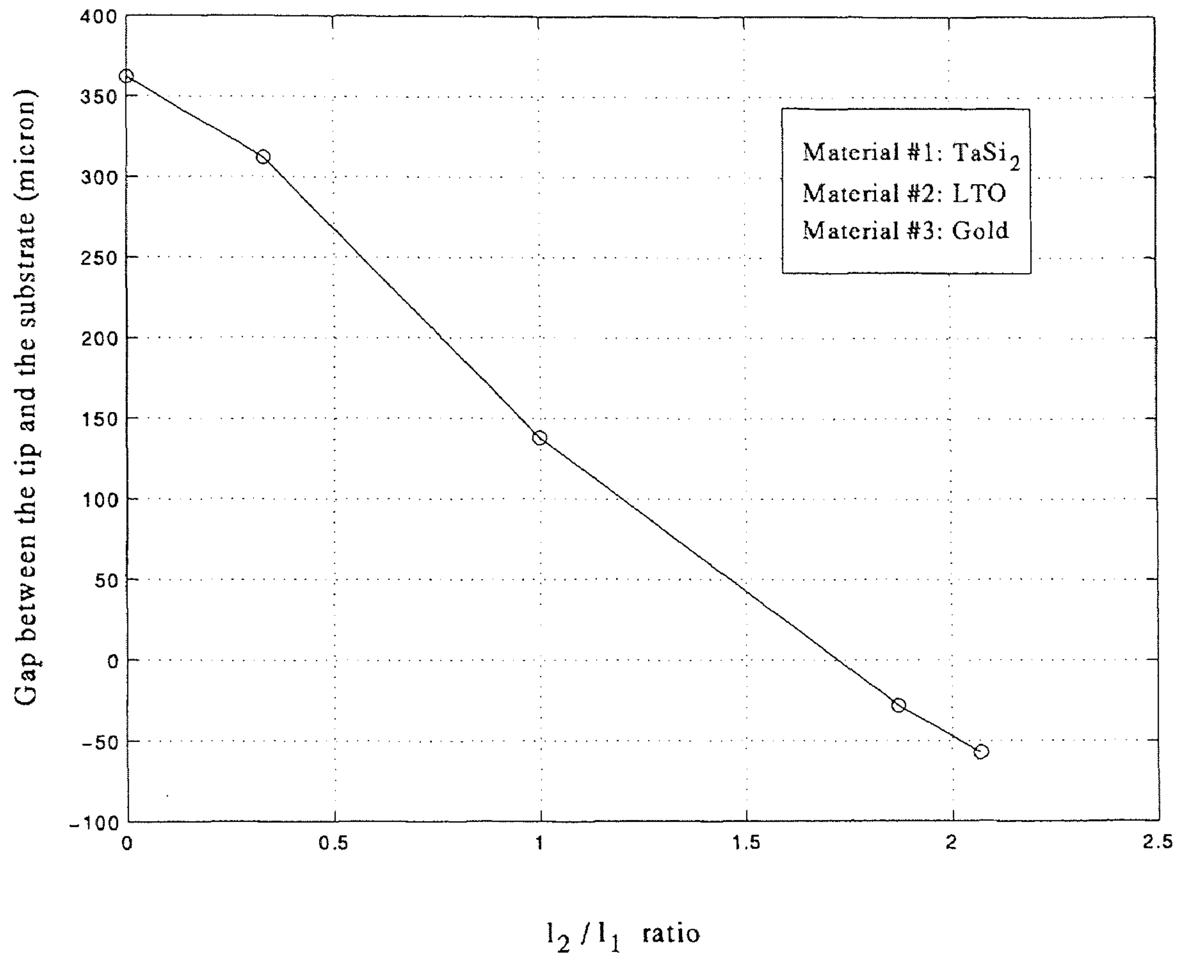

Figure 3.21 Simulation results of the two segment bimorph cantilever beam: Case # 3

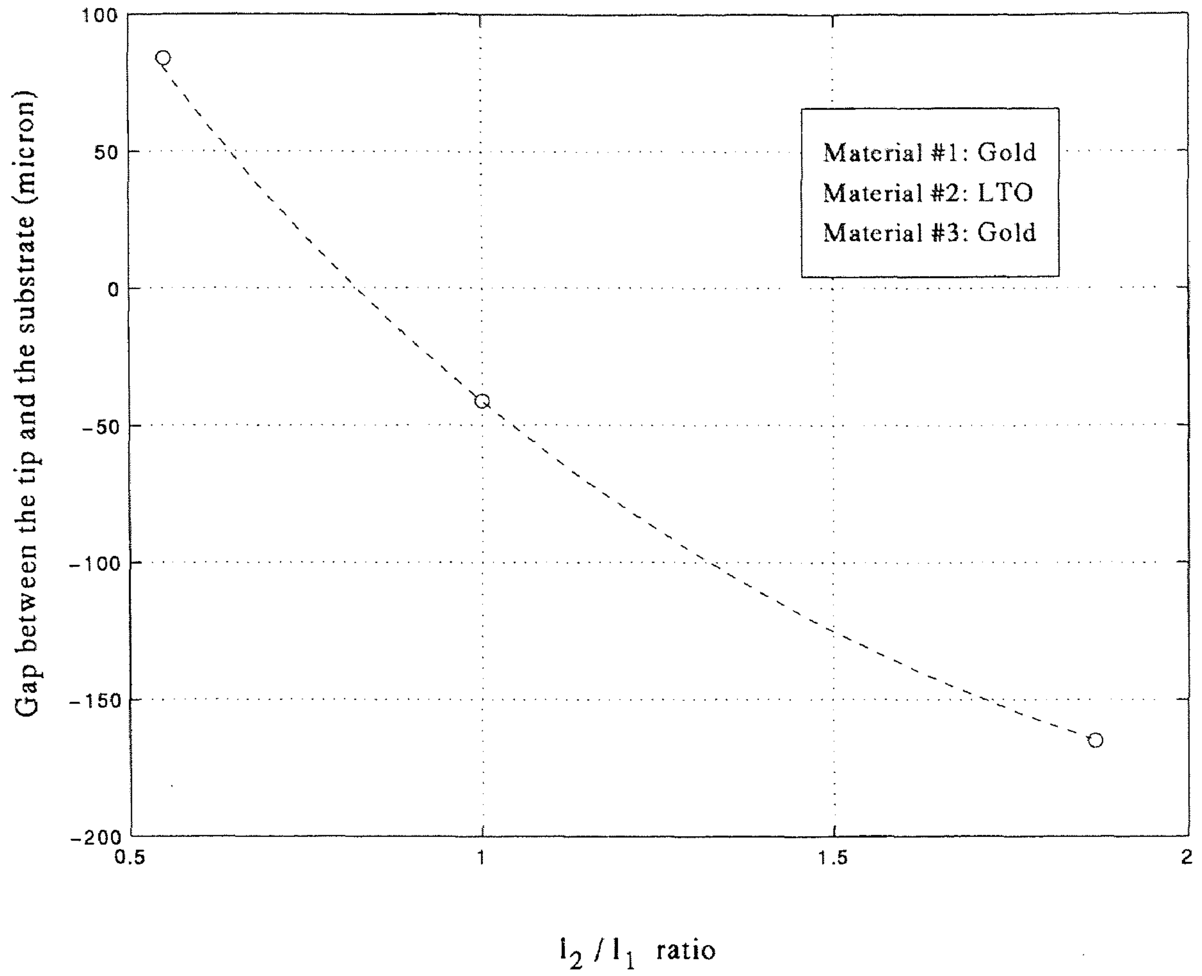

Figure 3.22 Simulation results of the two segment bimorph actuator: Case # 1

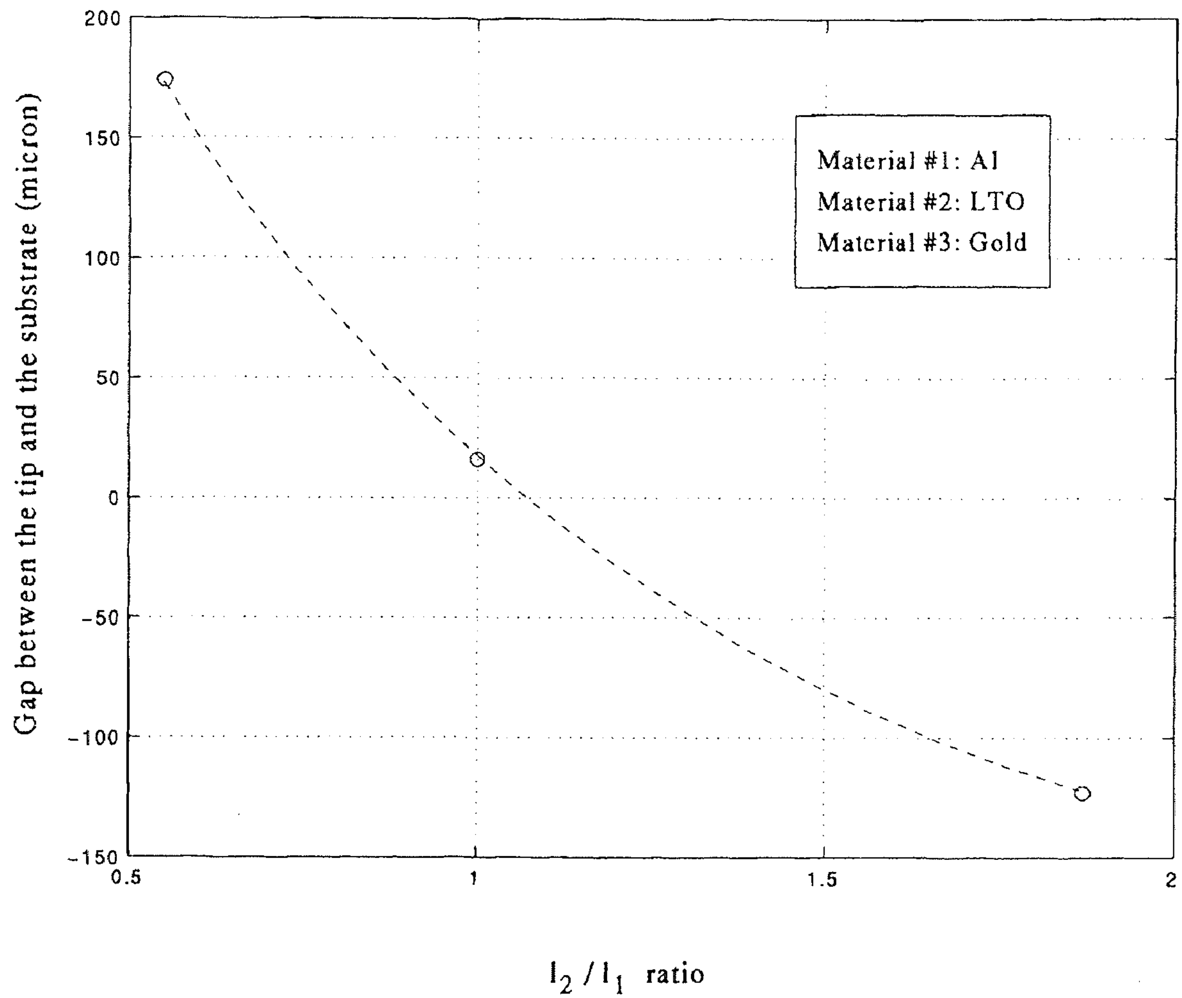

Figure 3.23 Simulation results of the two segment bimorph actuator: Case # 2

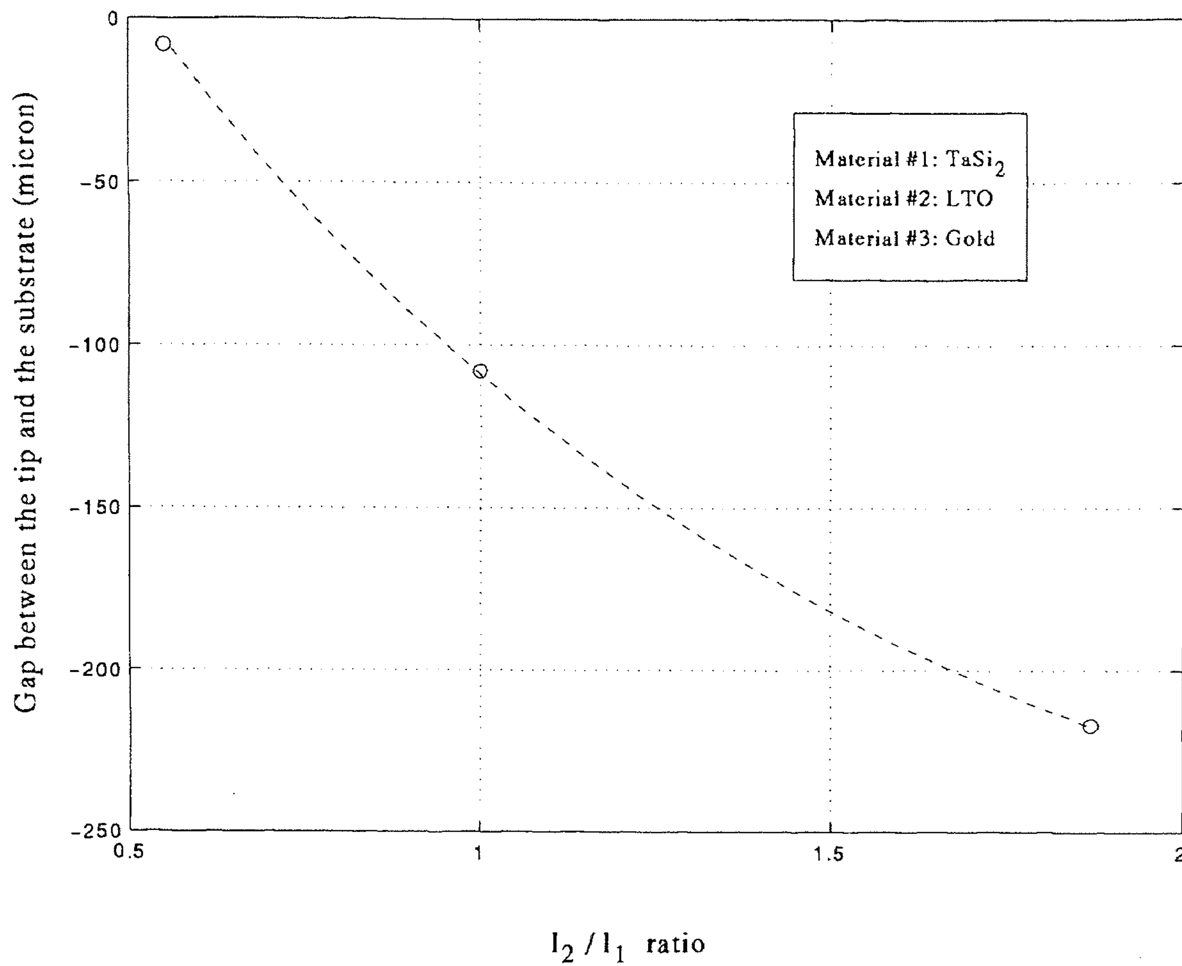

Figure 3.24 Simulation results of the two segment bimorph actuator: Case # 3

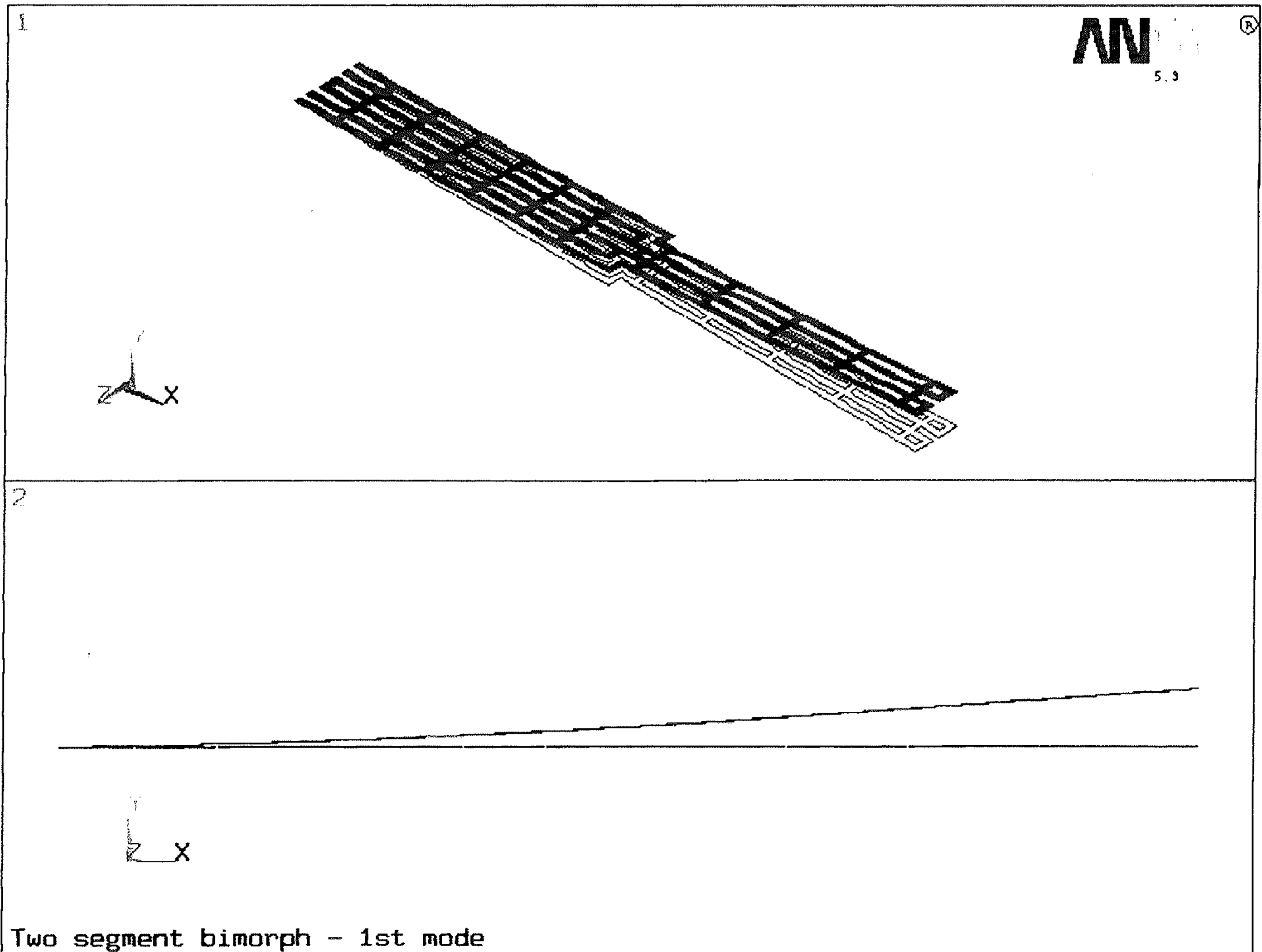

Figure 3.25 The deformed shape of the two-segment bimorph actuator at the first modal frequency ($l_1=l_2$)

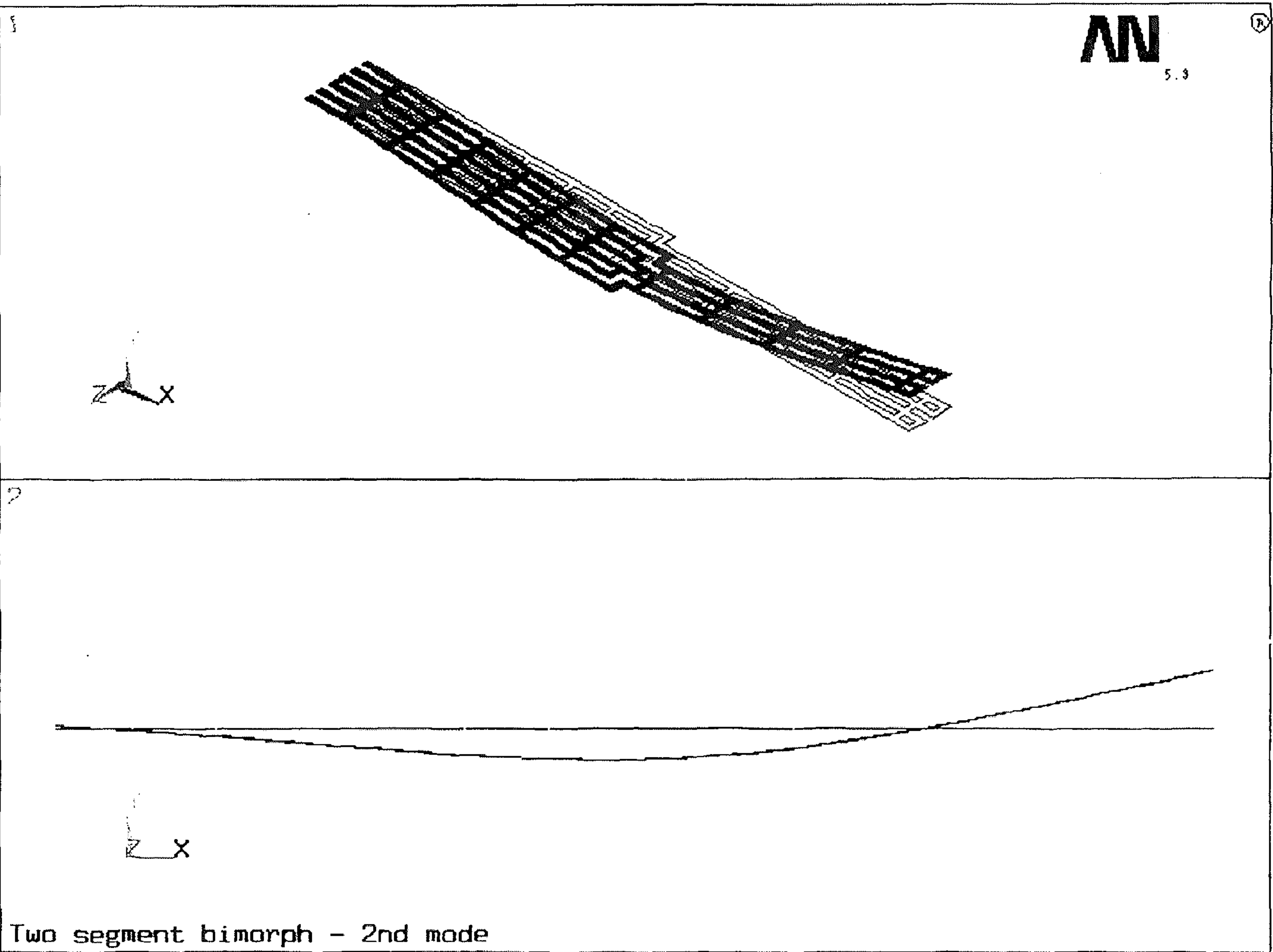

Figure 3.26 The deformed shape of the two-segment bimorph actuator at the first modal frequency (l_1=l_2)

CHAPTER 4

OUT-OF-PLANE ACTUATOR

In this section, the design of the bimorph out-of-plane actuators, which make use of thermal or residual stress, is discussed. The results are compared with the test results of the fabricated devices.

4.1 Thermal Design

In late 80's, bimetallic effect were presented as a promising microactuation technique, which relies on the thermal mismatch between two components of the sandwiched layer to provide force and displacement with change in temperature [17, 64, 65].

Figure 4.1 shows a schematic of the bimetallic cantilever, forces and moments acting on the cross-sections of a segment along the length of the composite beam as the temperature is increased. The internal stress over the cross-section can be reduced to a tensile force P and a couple M. Finally, the expression for the curvature, r can be derived as:

$$r = \frac{(w_1 E_1 t_1^2)^2 + (w_2 E_2 t_2^2)^2 + 2 w_1 w_2 E_1 E_2 t_1 t_2 (2t_1^2 + 3t_1 t_2 + t_2^2)}{6 w_1 w_2 E_1 E_2 t_1 t_2 (t_1 + t_2)(\alpha_2 - \alpha_1)\Delta T} \tag{4.1}$$

Assuming a constant radius of curvature r throughout the cantilever of the length L, the displacement δ at the cantilever tip can be obtained as follows:

$$\delta = \frac{1}{2}\frac{L^2}{r} \tag{4.2}$$

One must be careful with this equation. It is valid only, if the straight beam assumption mentioned in Section 3.2.2 is valid. When the tip displacement becomes large (e.g. curvature becomes small), the problem becomes nonlinear, and numerical methods need to be used.

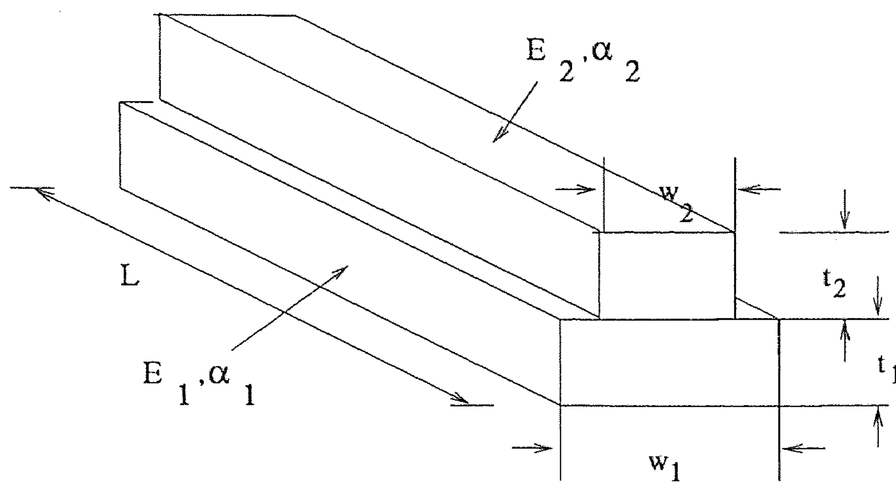

(a)

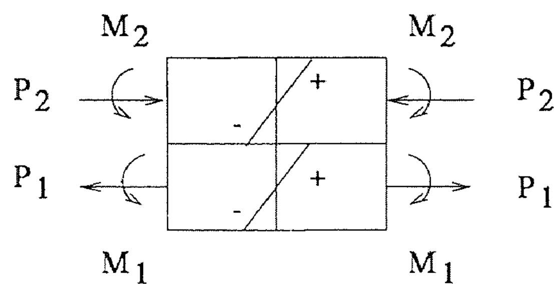

(b)

Figure 4.1 (a) Schematic of the bimetallic cantilever, (b) forces and moments acting on the cross-sections of a segment along the length of the composite beam

A bimorph, out-of-plane actuator was fabricated. It consists of a 0.9 μm thick SiO_2 as the lower layer and 0.6 μm $TaSi_2$ as the upper layer. The mechanical properties are given in Table 3.2. A 1 μm thick Al layer serves as the sacrificial layer. When the actuator is released, it bows up due to the thermal mismatch between SiO_2 and $TaSi_2$ (Figure 4.2).

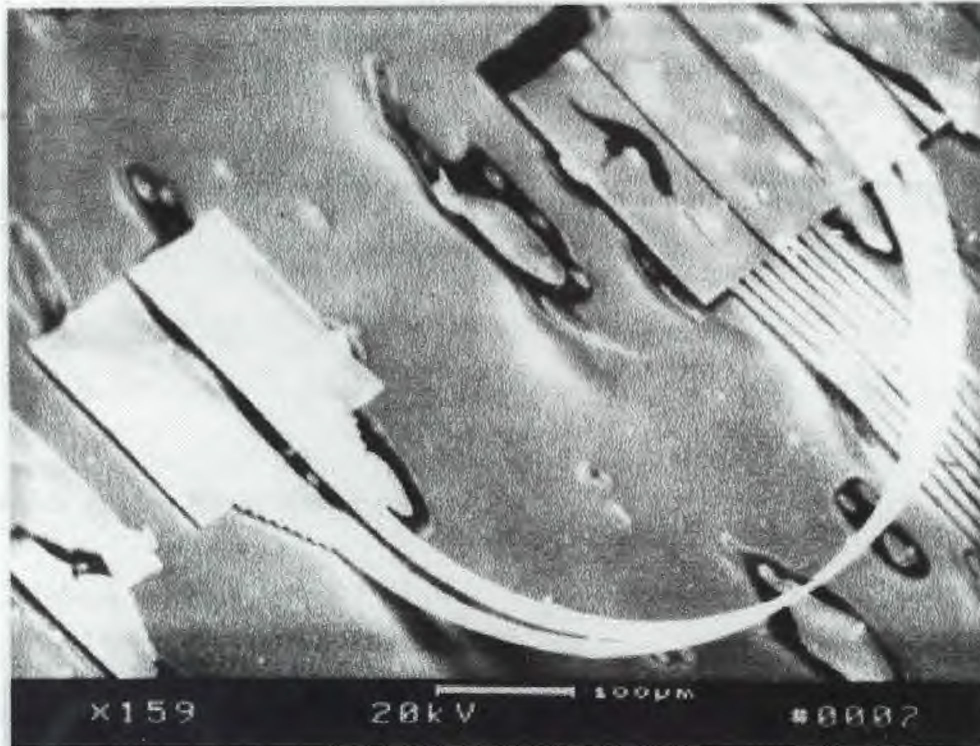

Figure 4.2 Released, bimorph, out-of-plane actuator.

The actuator can be driven by thermal and/or electrostatic excitation. The $TaSi_2$ layer serves as both the heater for thermal actuation and the upper electrode for electrostatic actuation.

Figure 4.4 shows a 1D lumped model, where the cantilever is represented by an ideal linear spring. The linear spring constant k is defined as the load per unit deflection. The deflection y_L at the tip of cantilever, which has a point load F at the tip (x=L), can be calculated as

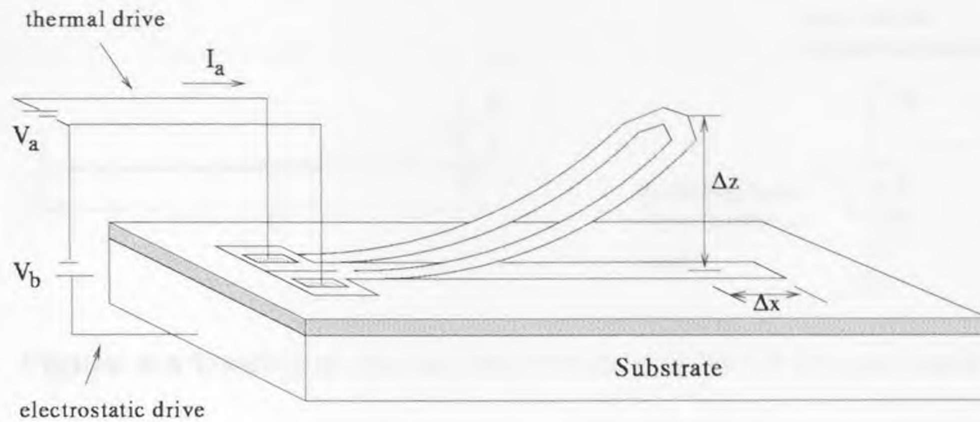

Figure 4.3 The bimorph, out-of-plane actuator can be driven thermally and/or electrostatically .

$$y_L = \frac{FL^3}{3EI} \, , \tag{4.3}$$

which gives a linear spring constant

$$k = \frac{F}{y_L} = \frac{3EI}{L^3} \, . \tag{4.4}$$

The thermal force F_{th} due to the thermal mismatch and F_r (the restoring force of the cantilever beam) are contradicting each other, and they bring the cantilever to the steady state position. The restoring force is

$$F \, = \, k \; y(x) \, . \tag{4.5}$$

The tip displacement due to thermal actuation can be calculated from Eq. 4.2 as long as the problem is linear. In all other cases, the 1D lumped model needs to be considered and numerical methods [1] needs to be applied to solve the problem.

[1]Newton-Raphson method, one of the many numerical methods, is discussed in APPENDIX A.

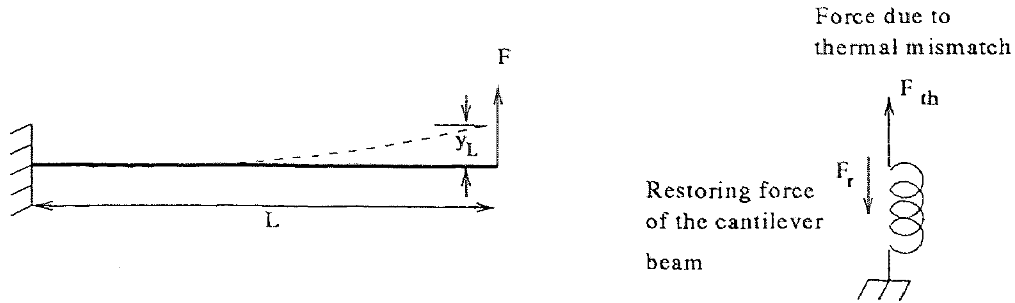

Figure 4.4 Loading of the cantilever beam and its 1D lumped model.

Thermo-mechanical finite element analysis of the out-of-plane actuator were performed using ANSYS ver5.3. The coupled electro-thermo-mechanical IntelliCAD, a CAD tool developed specifically for MEMS design by IntelliSense Inc.

First, the thermal drive was considered. The tip displacement of a bimorph cantilever beam with the properties given in Table 4.1 calculated from Eq. 4.2. A cantilever beam structure with the same dimensions and material properties was simulated using ANSYS with the large displacement (nonlinear analysis) option ON and the thermal uniform load applied in substeps. The calculated results are compared with the simulation results in Figure 4.5. From the figure, it can be easily seen, that the nonlinearities become significant at large temperature variations. Further simulations have shown, that the longer the cantilever beam is, the narrower is the linear region.

The process flow of the out-of-plane actuator is given in APPENDIX B. The $TaSi_2$ was sputtered on the LTO layer at 125°C. The actuator, which was in balance at sputtering temperature, curls up after the sacrificial aluminum etch at room temperature (Figure 4.2). To obtain the shape of the actuator after the release process, FEA was performed. To simulate the cooling from the process temperature to room temperature, negative uniform temperature was applied to the solid model. The deform shaped obtained from ANSYS is shown in Figure 4.6, which looks quite

Table 4.1 Dimensions and properties of the analyzed out-of-plane actuator

Beam length	1 mm
Beam width	8 μm
Top Layer:	
Material Thickness	$TaSi_2$ 0.6 μm
Bottom Layer:	
Material Thickness	SiO_2 0.9 μm

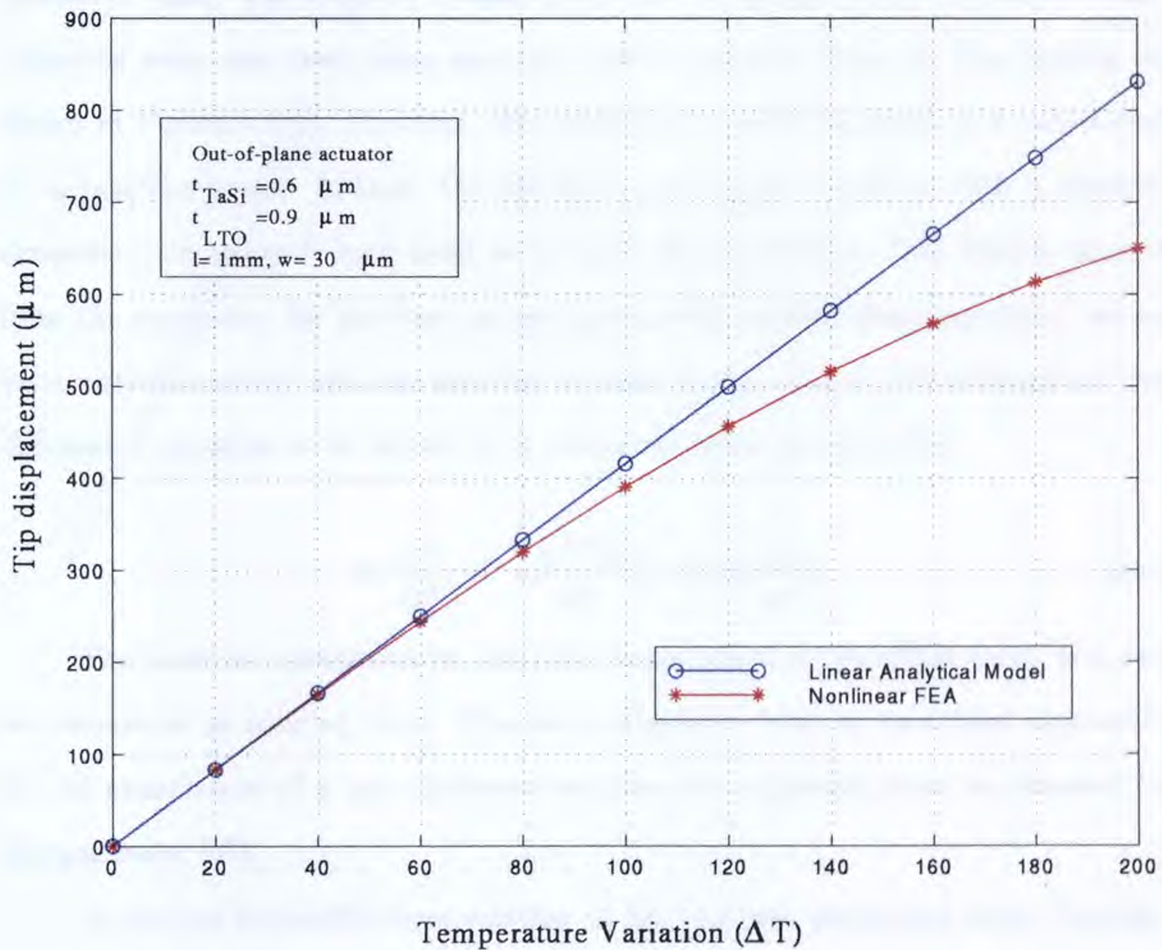

Figure 4.5 Tip displacement of the bimorph cantilever vs. temperature.

different from the test structure. From this figure one can conclude, what the simulation results reflect, is far from the deformed shaped of the actual, fabricated actuator. However, when the shape is reconstructed from the horizontal and vertical displacement values along the actuator obtained from FEA, one reaches the shape shown in Figure 4.7. The graphical user interface of FEA tools may be inappropriate to represent the real view, especially when large displacements are concerned. This example stresses the importance of correct evaluation of the simulation results.

4.2 Electromechanical Design

The thermal force can be combined with electrostatic force to drive the curled cantilever beam. The simplest model of electrostatic actuation is a 1D parallel plate capacitor with one fixed plate and one plate suspended from an ideal spring as shown in Figure 4.8(a). However, the rigid-parallel plate capacitor is a bad model for a bending beam. Instead, the 2D beam differential equations with a position dependent electrostatic load need to be used (Figure 4.8(b)). The load is derived from the expression for the force on an incremental parallel plate capacitor, whose value varies inversely with the position dependent gap. Under this assumption, the differential equation to be solved for a cantilever beam becomes [66]

$$EI\frac{d^4y}{dx^4} = -\frac{\epsilon_o V^2 w}{2y^2}\left(1 + 0.65\frac{y}{w}\right). \qquad (4.6)$$

The term in parenthesis on the right hand side is a correction term, and can be considered as fringing term. This term originates from an analytical expression for the capacitance of a zero-thickness stripline over a ground plane as obtained by Morganthaler [67].

Numerical finite-difference solution of Eq. 4.6 was performed using Newton-Raphson method implemented in MATLAB. The length of the beam (L) was

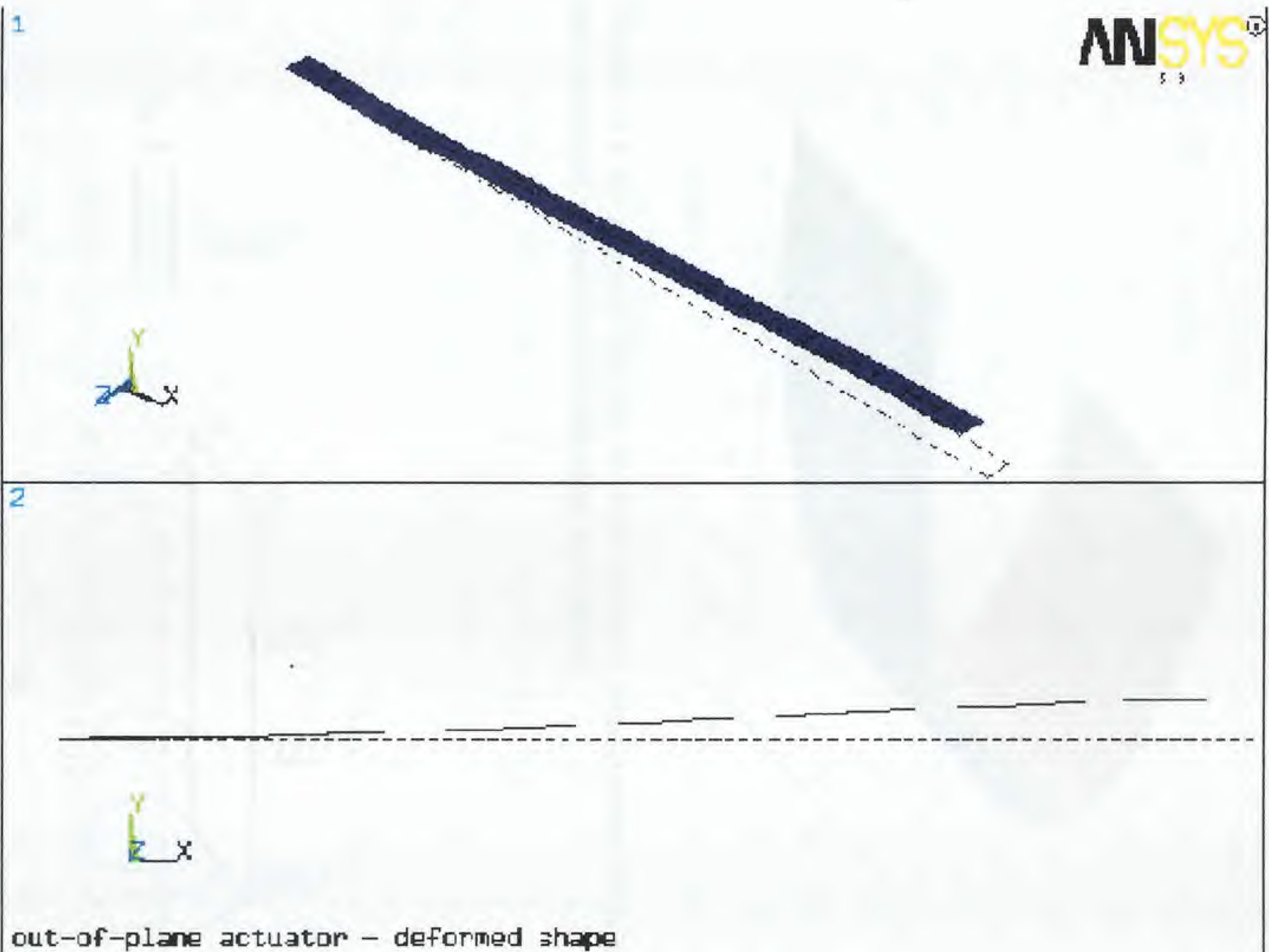

Figure 4.6 Calculated deformed shape of the out-of-plane actuator at room temperature.

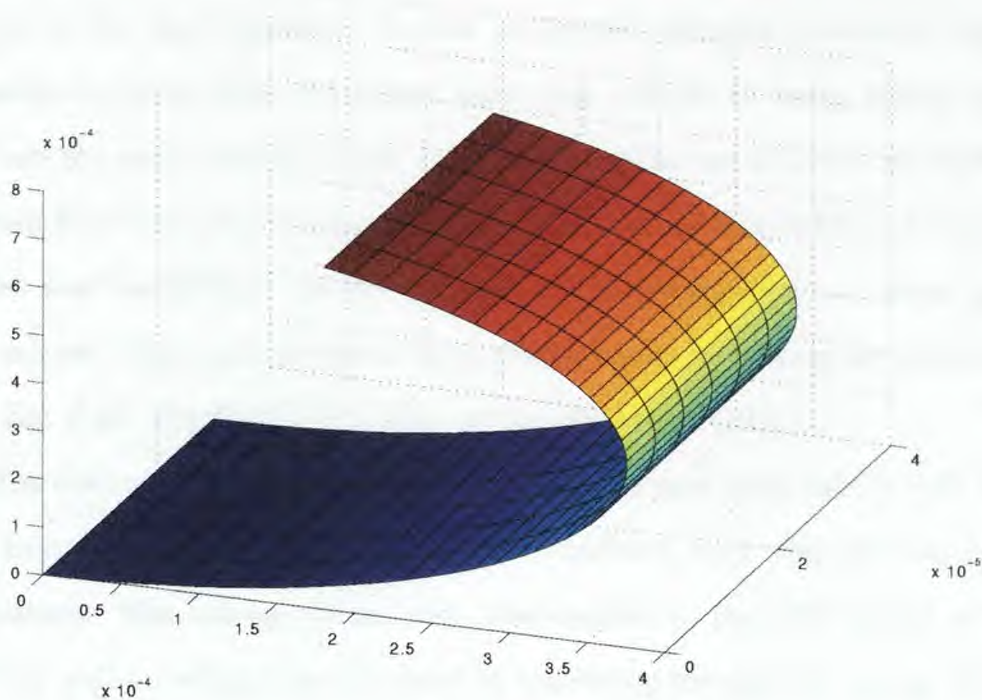

Figure 4.7 3D shape of the out-of-plane actuator reconstructed from the vertical and horizontal numerical data obtained by ANSYS.

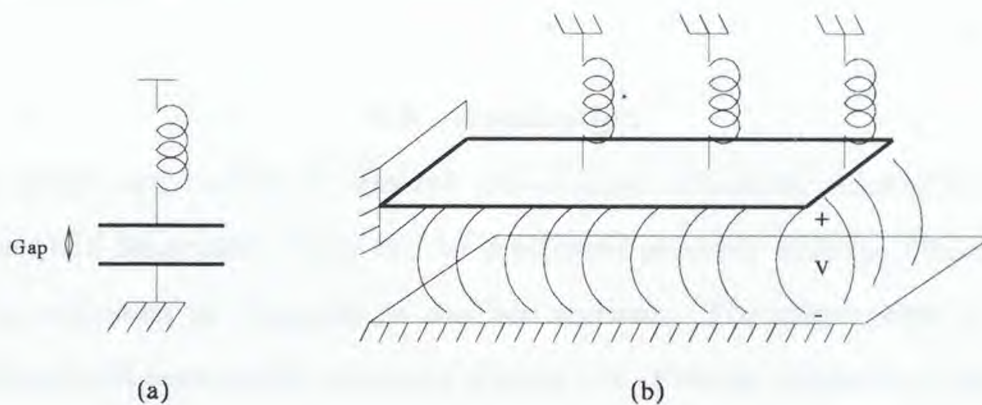

Figure 4.8 (a) 1D lumped parallel plate capacitor model (b) Visualization of the 2D problem

discretized into small elements, and Eq. 4.6 was solved according to the Newton-Raphson method. User chosen number of successive iterations were performed to converge to the final solution. The 2D model with fringing correction was found reasonably accurate when the aspect ratio (gap relative to beam width) is small, and when the gap is small enough so that the pull-in instability is reached before the beam bending enters the large-deflection region. In this MATLAB script, also included was the ability to model a curled cantilever subjected to a stress gradient before release. The model accounts for this deformation by varying the gap according to the Eq. 2.16. The MATLAB script is given in APPENDIX C.

The electromechanical FEA analysis was performed using IntelliCAD. Cooling down from the process temperature was simulated with the uniform negative temperature. The voltage values were also applied to the solid model as a load case. The pull-in voltage was obtained by increasing the applied voltage difference between the cantilever beam and the substrate.

In Figure 4.9, the calculated pull-in voltage vs. vertical tip displacement of the $TaSi_2$-SiO_2 cantilever beam of interest is compared with FEA and test results. As mentioned above, the numerical solution of the Eq. 4.6 gives correct results only in the linear region.

4.3 Application

As a system application of bimorph out-of-plane actuators, micromirrors were designed and fabricated. They can be positioned precisely utilizing bimorph out-of-plane actuators as discussed in previous sections. The micromirror is a SiO_2 platform placed between two actuators (Figure 4.10. Process temperature dependent internal stress causes the $TaSi_2$-SiO_2 actuators (Figure 4.11) to bow upward after the sacrificial layer etch, and they lift the micromirror up. The dimensions of the micromirror are 500 μm x 400 μm. When thermal or combined thermal and

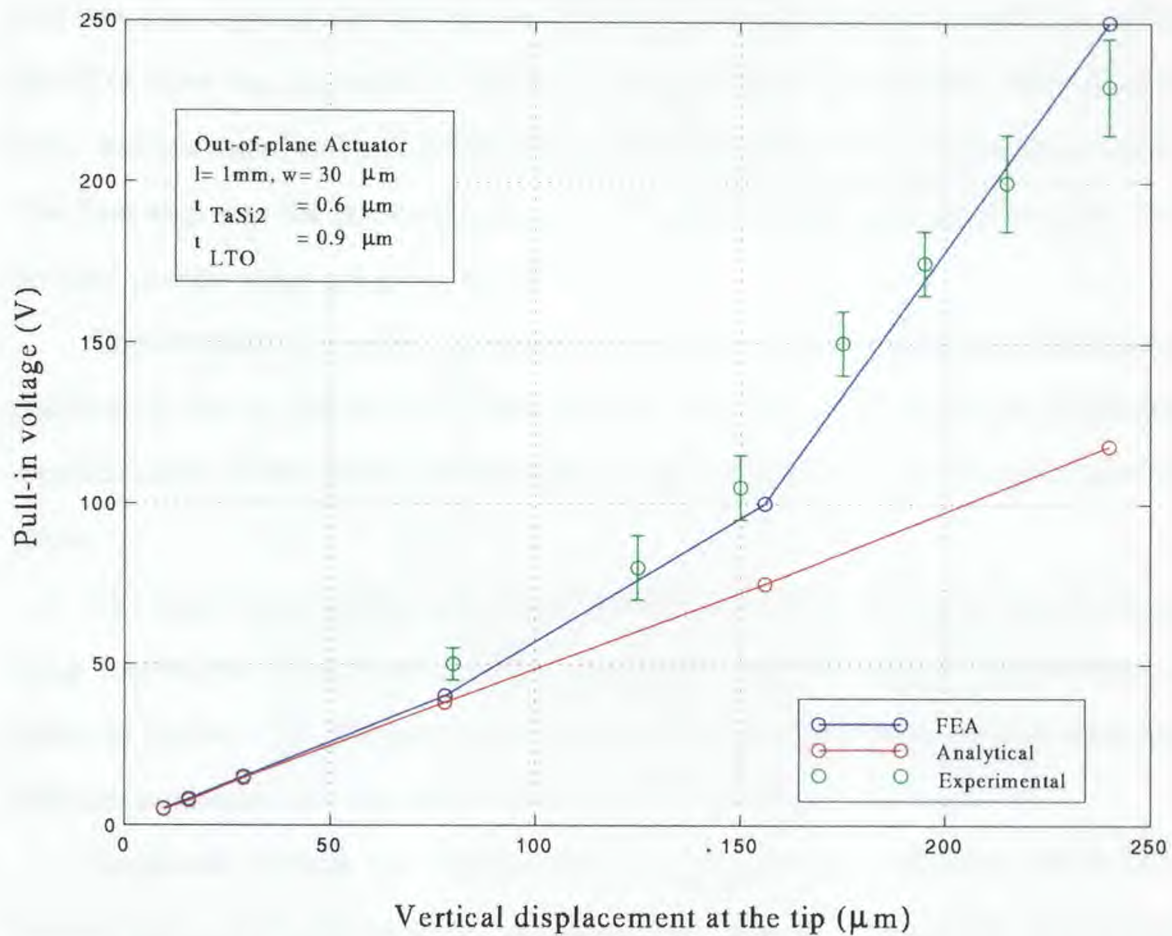

Figure 4.9 Pull-in voltage vs. vertical tip position of the $TaSi_2$-LTO out-of-plane actuator.

electrostatic drive is applied, the actuators flatten out and position the micromirror precisely (Figure 4.12).

The fabrication process can be summarized as follows. First, a thermal oxide layer of 3000 Å of thermal oxide was grown on n type < 100 > oriented wafer, followed by a 2000 Å Si_3N_4 LPCVD. These two layers served as the insulation layer. 1 μm Al sputtered as the sacrificial layer. Then, 9000 Å LTO deposited, which was both the first layer of the bimorph actuators and the micromirror platform. After the LTO layer was patterned to form the actuators and micromirror, 6000 Å thick $TaSi_2$ was sputtered and patterned to form the second layer of the bimorph actuator. The final step was the Al sacrificial layer etch and the release of the structure. The detailed process steps are given in APPENDIX B.

The released micromirror is shown in Figure 4.13. The curvature of the mirror platform, is due to high residual stress in LTO. Because of the underlying aluminum sacrificial layer, LTO couldn't be annealed at high temperature to released its internal stress.

The static thermal-electromechanical behavior of the micromirror was simulated using IntelliCAD. The mesh used in mechanical and electrostatic simulations is shown in Figure 4.14. The green area is the substrate, the yellow and gray areas are bimorph actuators, and the red one is the mirror platform.

Simulated vertical tip displacement vs. temperature difference (with only thermal drive and V_b=0) is shown in Figure 4.15. The FEA results for the thermal drive combined with electrostatic (V_b=30V) is shown in Figure 4.16. The new version of IntelliCAD can handle nonlinear *Contact Analysis*. To simulate the structure with decreasing thermal power, first it was brought into contact with the substrate by applying the temperature and the pull-in voltage to the solid model as the load case. Then this displacement case is used as the initial value for the consecutive contact analysis steps.

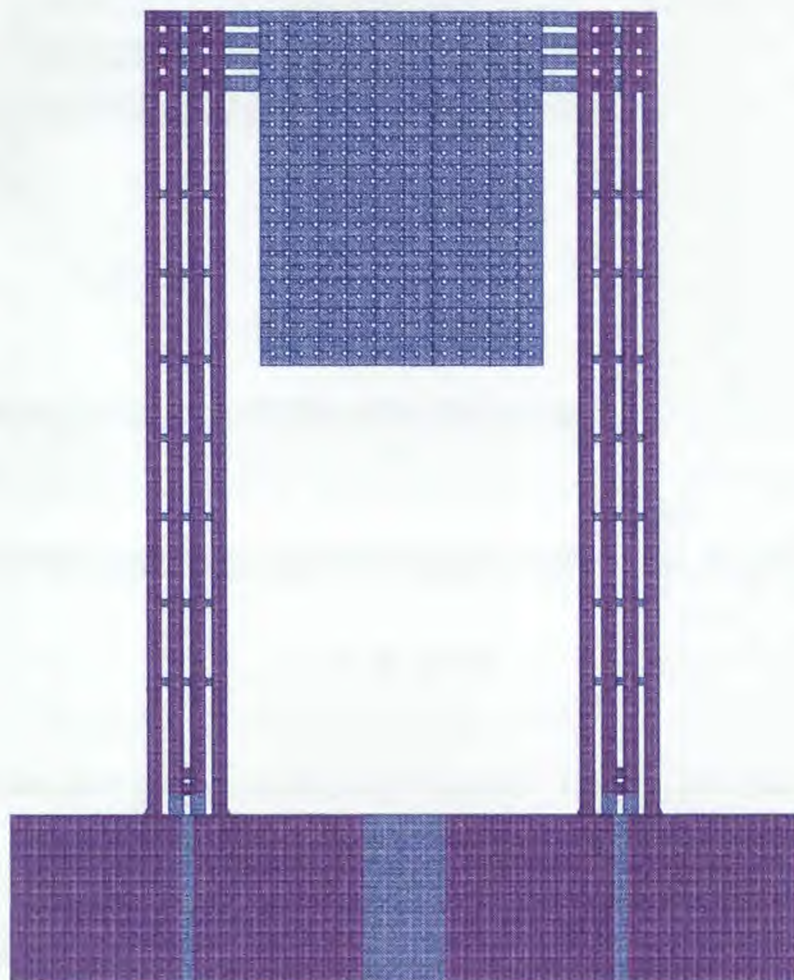

Figure 4.10 Layout of the micromirror designed using Mentor Graphics; LTO (blue) and $TaSi_2$ heater (pink) mask.

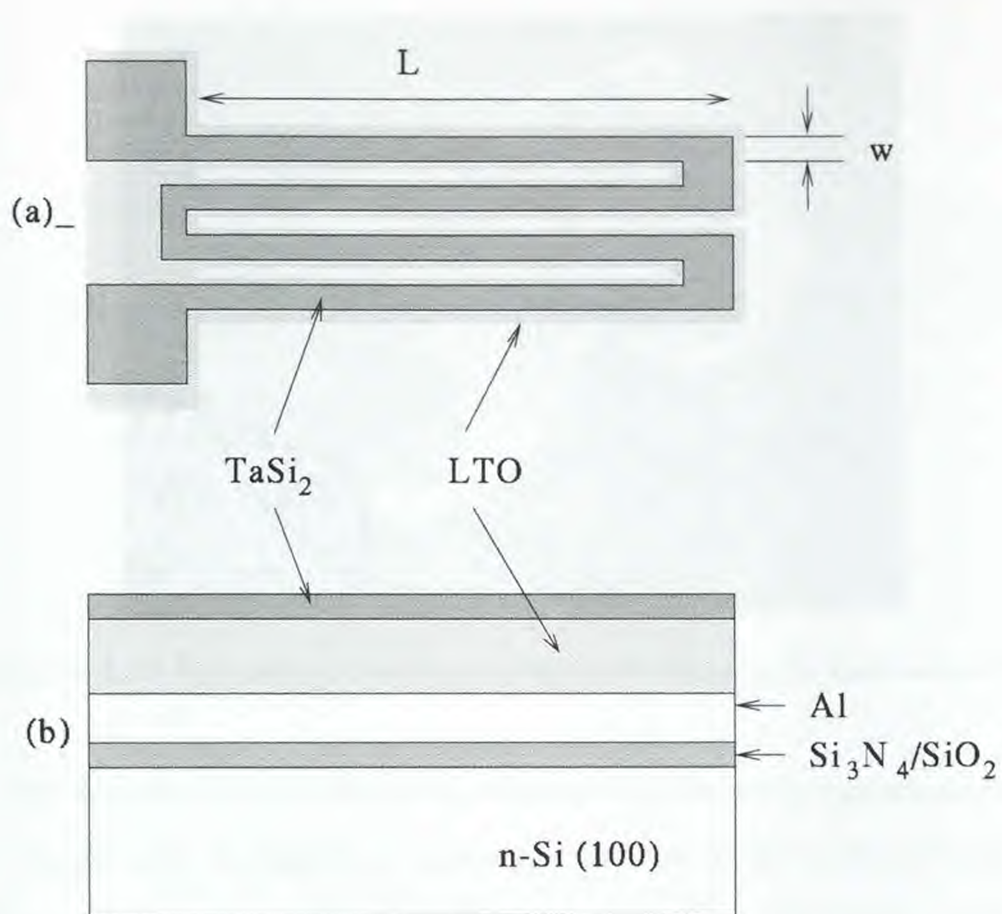

Figure 4.11 Schematic view of the bimorph actuator, (a) top, (b) cross-section.

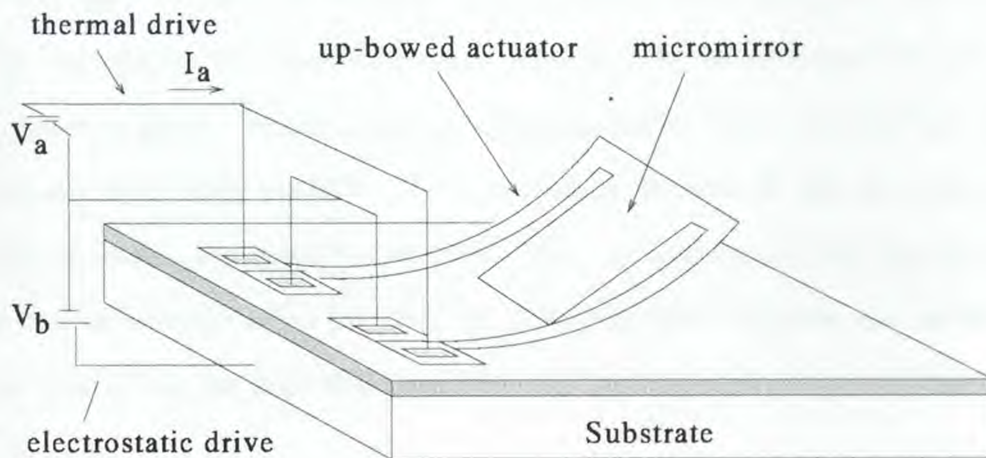

Figure 4.12 Schematic view of the micromirror with combined thermal and electrostatic drive.

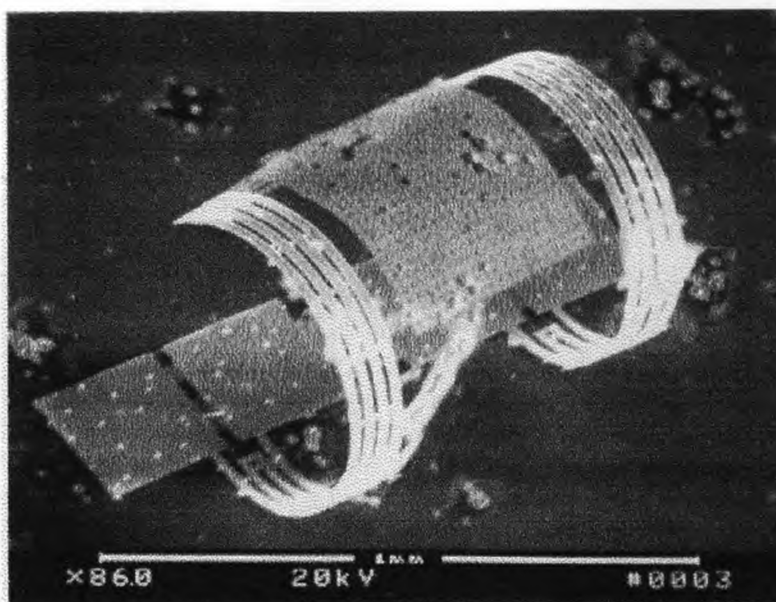

Figure 4.13 Released micromirror actuated by two out-of-plane actuators.

The micromirror was tested with thermal and combined thermal-electrostatic drive (Figure 4.12). In Figure 4.17 shows the variation of the tip displacement with the thermal input power (V_b=0). The sheet resistance of the unannealed $TaSi_2$ film was measured to be $\approx 1\Omega/\square$, and the resistance value of the $TaSi_2$ heater was calculated to be 400Ω. At a thermal input power 15 mW, a degradation of the heater's shape was observed. At higher input power values, the heater was damaged.

In Figure 4.18, the vertical tip displacement of the micromirror with the varying input power is given. In this case the thermal driving force is combined with the electrostatic force with V_b=30V. The hysteresis is because of the very high electrostatic force, when the mirror becomes flat. One can make use of this hysteresis. The mirror can be brought to the flat position. Then the thermal power can be decreased, and the mirror can be kept flat even with the low thermal power and electrostatic drive.

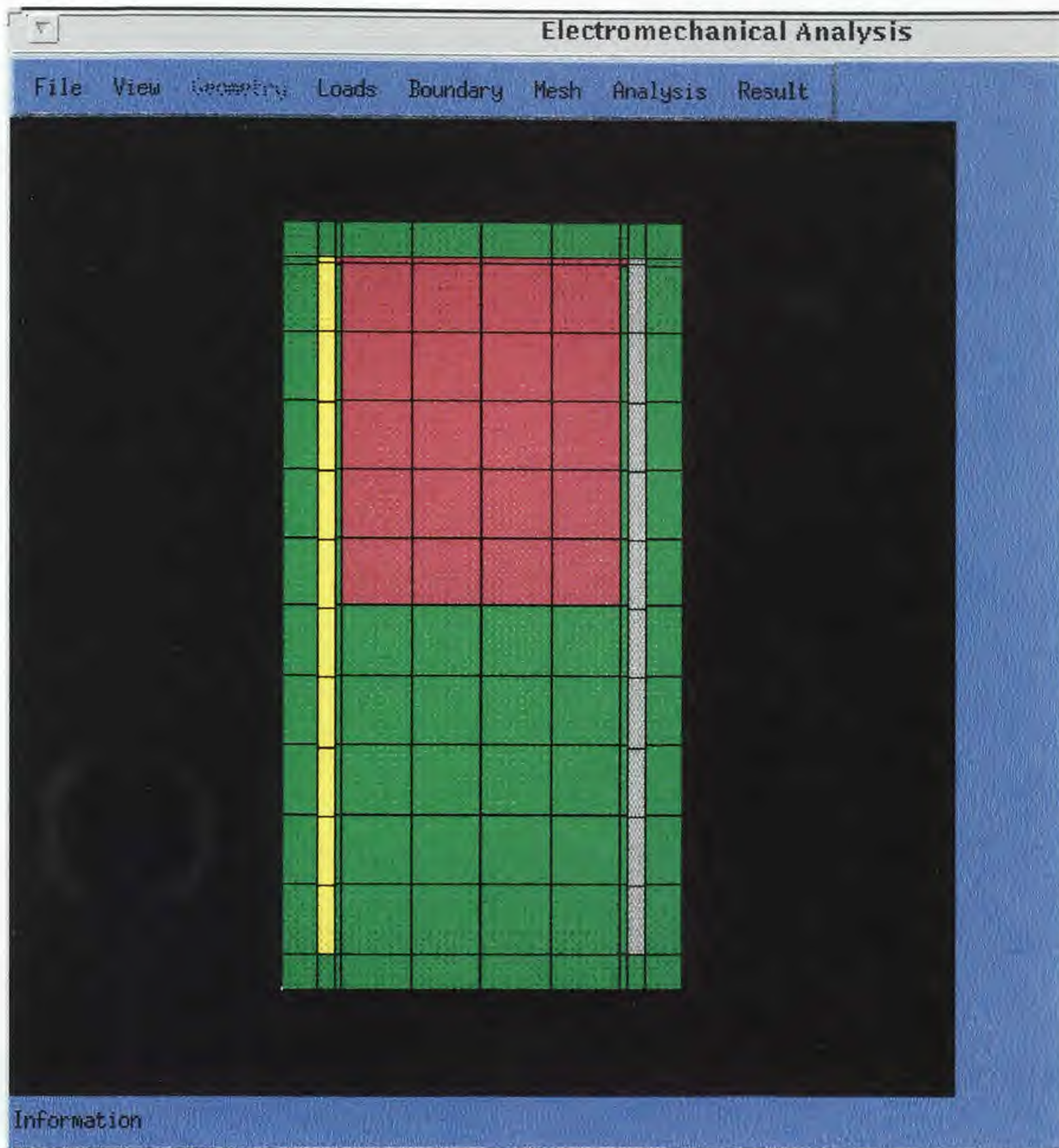

Figure 4.14 Meshed solid model of the micromirror (IntelliCAD).

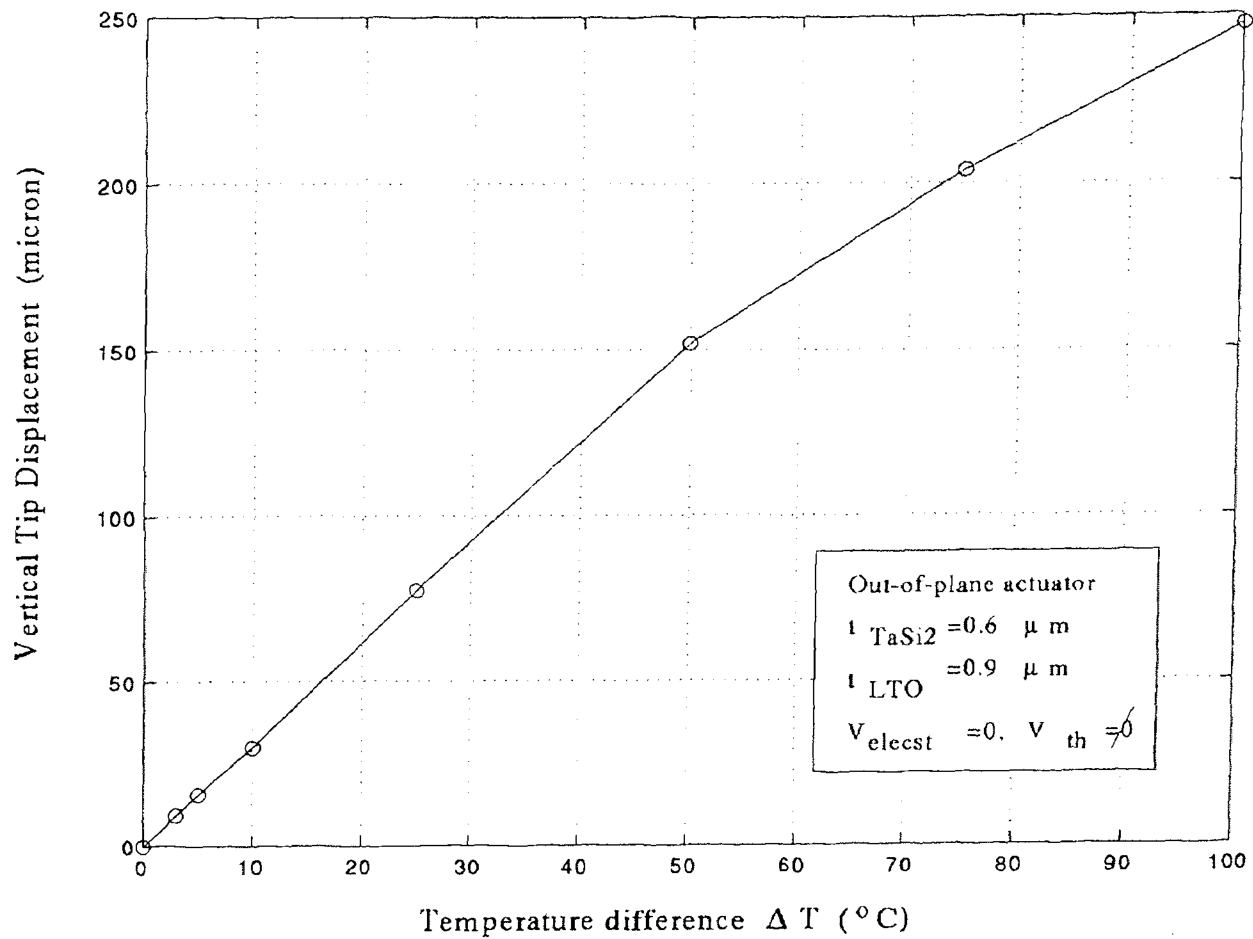

Figure 4.15 Calculated vertical tip displacement vs. temperature difference - IntelliCAD (without electrostatic drive).

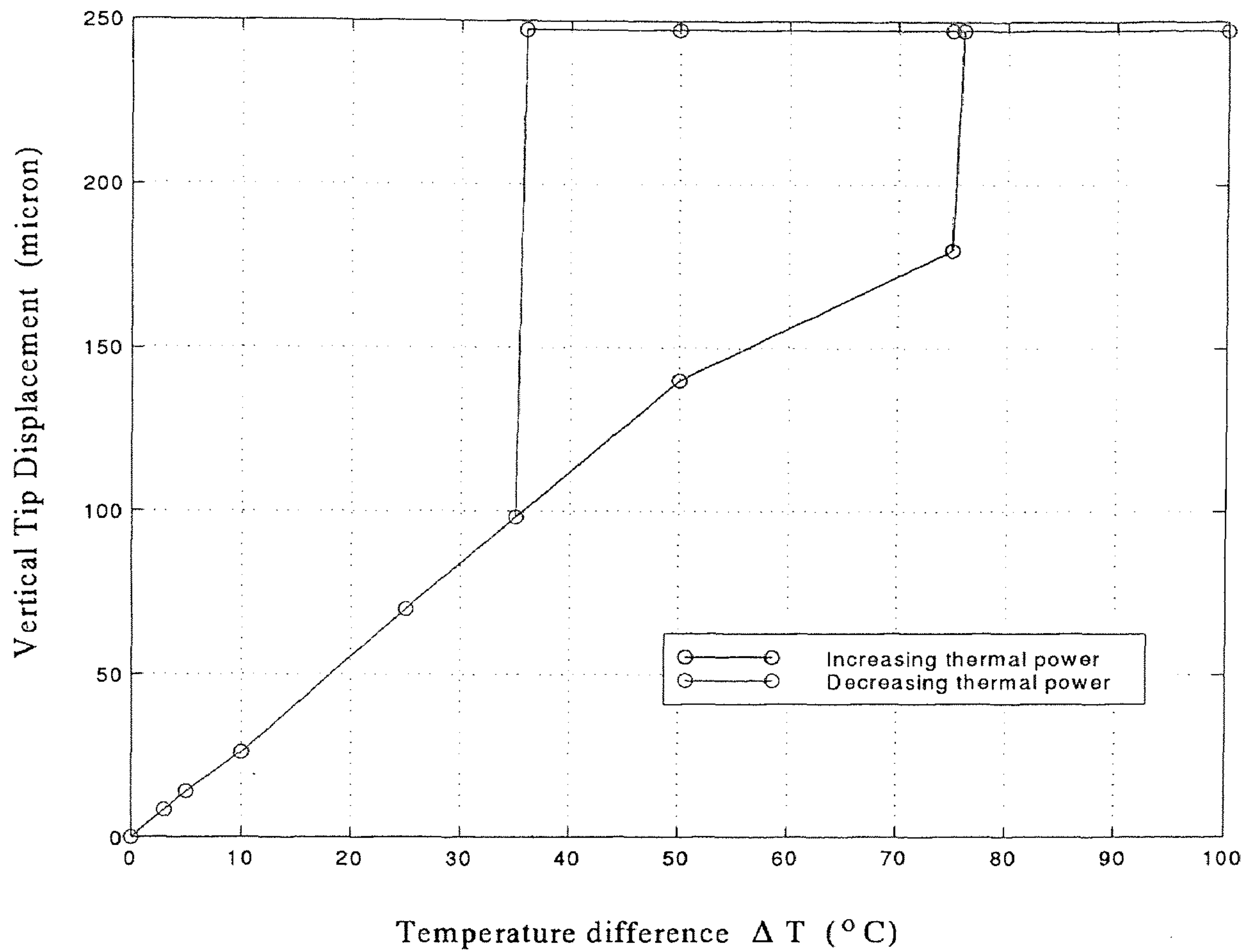

Figure 4.16 Simulated vertical tip displacement vs. temperature difference for the out-of-plane actuator - IntelliCAD (with V_b=30V).

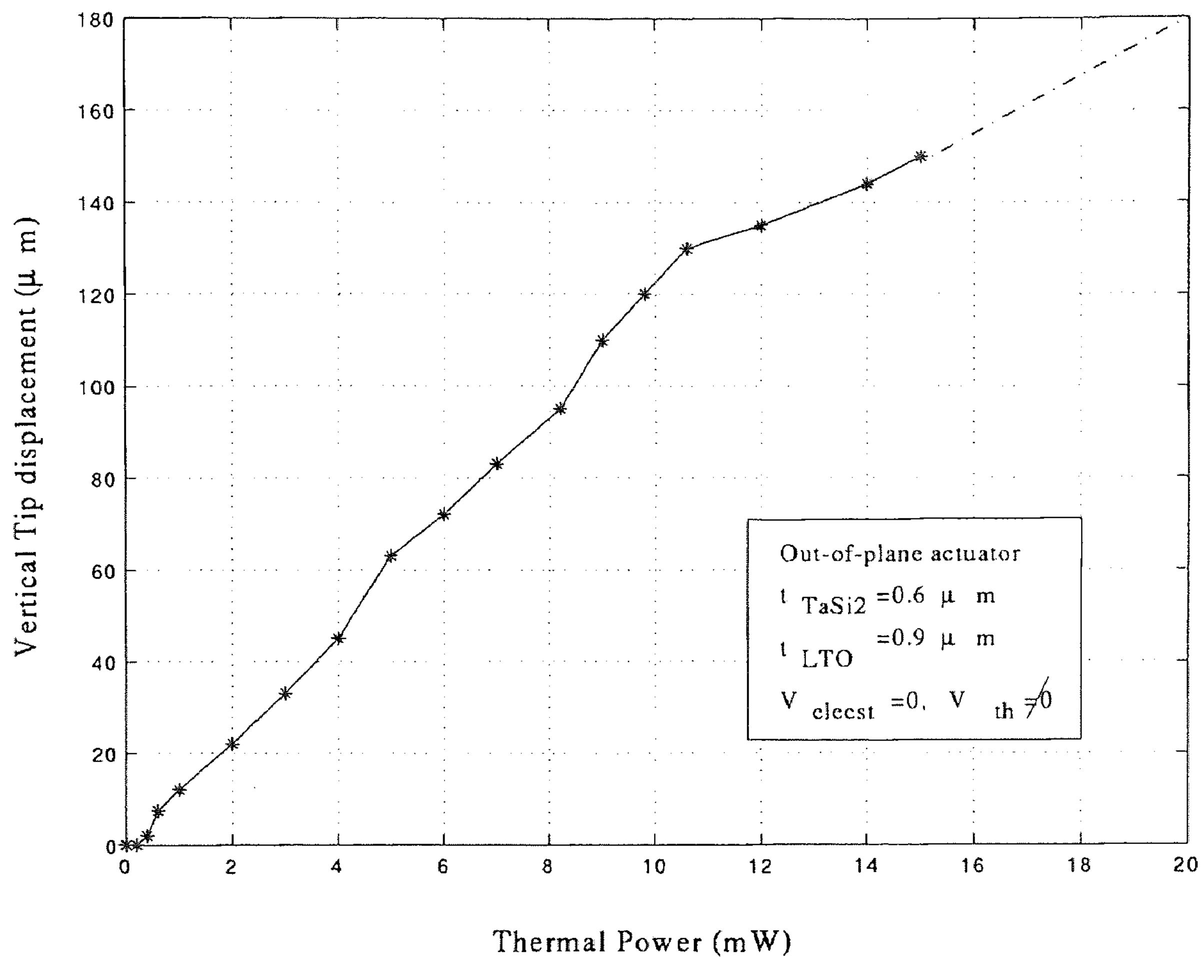

Figure 4.17 Measured tip displacement vs. thermal input power without electrostatic drive.

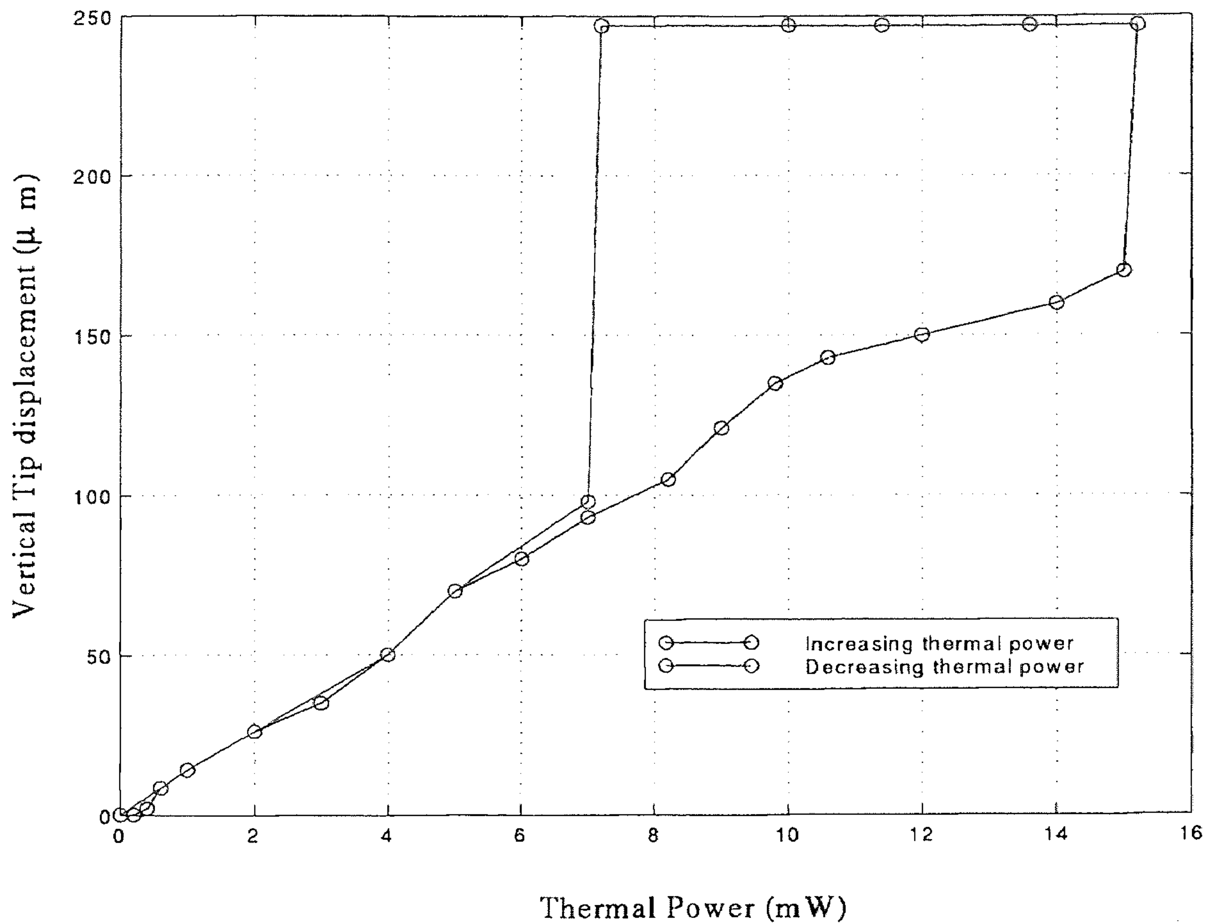

Figure 4.18 Measured tip displacement vs. thermal input power for the out-of-plane actuator with electrostatic drive (V_b=30).

CHAPTER 5

RESHAPING AS A NEW MICROMACHINING AND SELF-ASSEMBLY TOOL

Today, the fabrication of microactuators and micromechanical parts is merely based on IC fabrication technologies. The main reasons are tremendous know-how in IC fabrication and available IC based services for a reasonable price. However, the micromechanical world is three-dimensional and 2D world of microelectronics sets a limit to it. There are techniques available to construct 3D microstructures, which were briefly discussed in Chapter 1. Although successful products have been demonstrated utilizing these techniques, they are expensive, and there are still many challenges to overcome.

A new micromachining and self-assembly technology is introduced to realize 3D structures, actuators, and micro-electro-opto-mechanical systems. The advantages of two-dimensional IC fabrication are combined with the third dimension of the mechanical world. With the new technology, a structure fabricated by the surface micromachining technology can be deformed to any desired 3D shape. In this process the micromachined structure is first elastically deformed and then annealed by Joule heating generated by the current passed through the structure (thermal power dissipation, $P_t=I^2R$).

A similar technique was proposed by Fujita [68], but there is a lack of a detailed investigation, which will help to understand the reshaping process. These details are discussed in an elaborate manner in this chapter. Different reshaping setups are proposed and discussed. The reshaped structures can be used in many applications including fabrication of 3D actuators. First 3D reshaped actuators and a micromirror as an application example, which makes use of reshaped actuators, were designed and fabricated. The design, fabrication and test results of the micromirror are given in this chapter along with a 3D optical system example.

5.1 Fabrication

The polysilicon structure to be reshaped was fabricated with the following process: First, a thermal oxide of 3000 Å was grown and a 2000 Å thick LPCVD Si_3N_4 layer was deposited. These two layers serve as an insulation layer between the polysilicon layer and the substrate. Then $2\mu m$ thick LTO was deposited as the sacrificial layer, followed by LPCVD of a $1.6\mu m$ thick polysilicon layer. After the polysilicon structures were patterned by reactive ion etch with photoresist as mask, the sacrificial LTO layer was etched in 49% HF to release the actuators. In order to avoid any sticking onto the substrate, isopropanol vapor was used, which led to $\approx$ 100% release yield. The detailed process steps are given in APPENDIX B.

The basics of the reshaping process can be summarized in the following steps: First, the free end of the actuator is lifted with one probe, and the actuator is deformed to the desired shape (Figure 5.1(b)). Then voltage applied between the anchored end and the tip. Joule heat raises the temperature of the arm high enough to cause the anneal effect, and the stress in the arm is released. After removing the voltage, the arm cools down and the structure keeps its 3D shape (Figure 5.1(c)).

5.2 Recrystallization of Polysilicon and Grain Growth

Heat treatments of polysilicon were investigated in mid 70's [69]. The primary recrystallization temperature was defined as the temperature at which 95% of the material was recrystallized within half hour. It was found to be between 1100°C and 1250°C depending on the shape and dimensions of the grains. Secondary recrystallization was observed to occur from 1350°C onwards [69].

During reshaping process, the annealing occurs at much lower temperature than the recrystallization temperatures mentioned above. When the polysilicon beam was heated up to be reshaped, it's color was observed to turn to orange, where the beam was reshaped. This color indicates a temperature of 625-650°C. There is an

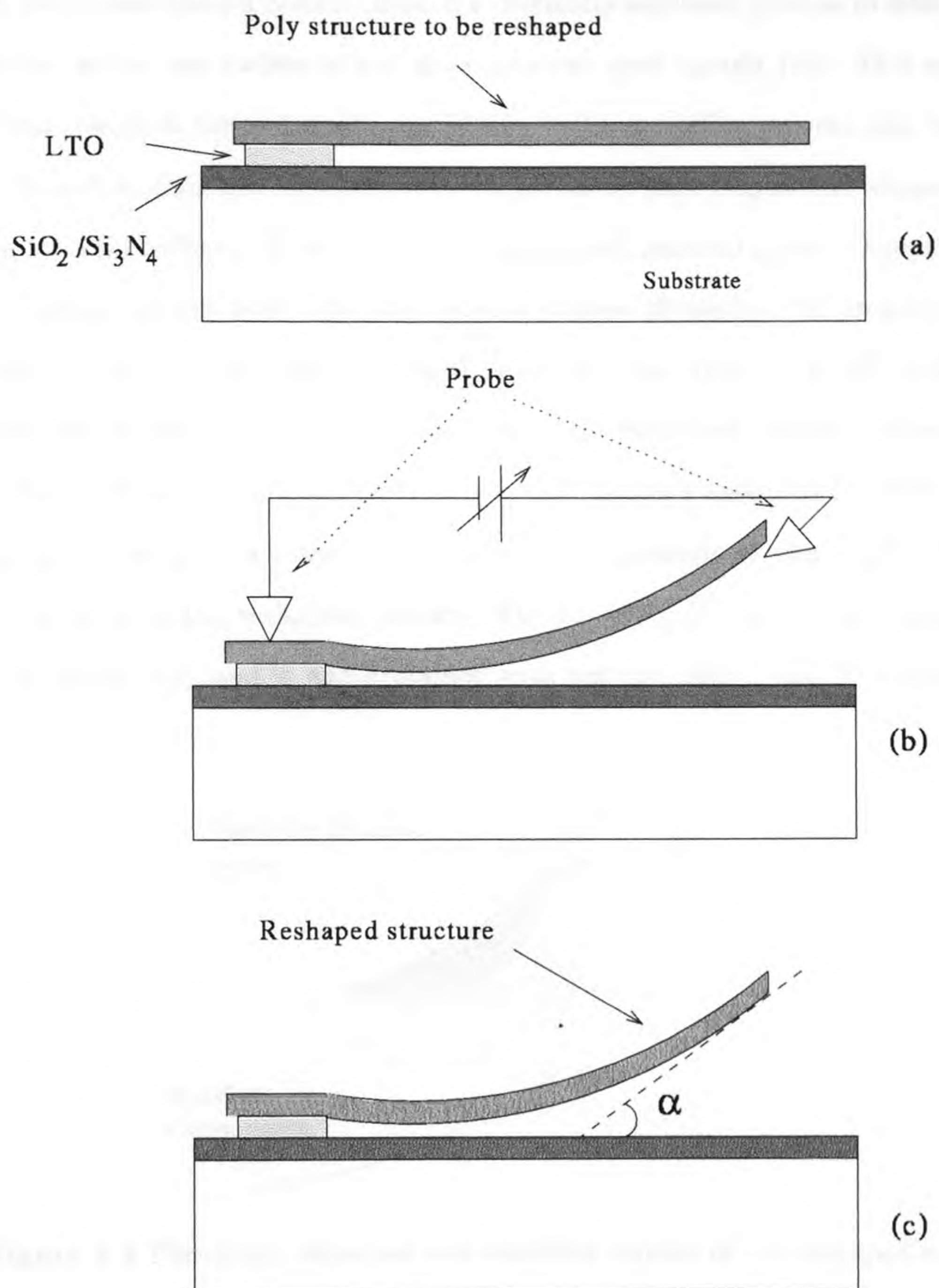

Figure 5.1 Setup for reshaping process

approach developed independently by Johnson and Mehl, Avrami and Kolmogorov (JMAK theory), which forms the basis for analytical models of recrystallization. This theory recognizes that recrystallization is a thermally activated process in which new, strain free grains are nucleated and grow into the grow matrix [70]. This explains the stress release in the reshaped arm. However, the annealing process also causes a major change in grain size as reported in the literature [39]. Deposition temperature, doping level [71], effects the grain size, structure, and residual stress. Depending on the annealing current and annealing time, a change of mechanical properties was observed. Later in this chapter, it will be shown that there is a 10% difference between the simulated natural frequency and the measured natural frequency of the reshaped beam, and it can be inferred, that Young's modulus changes due to reshaping. This can be attributed to plastic deformation at the highly stressed region involves in the reshaping process (Figure 5.2) [72]. A similar change was reported before [44], and it was explained with texture change and modification of Si-Si bonds.

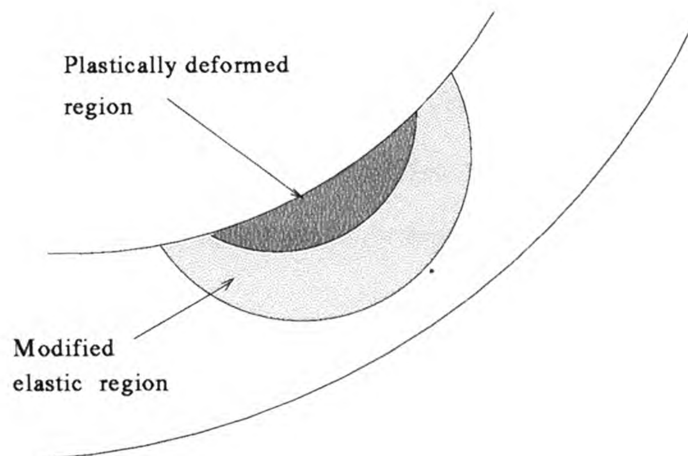

Figure 5.2 Plastically deformed and modified regions of the reshaped arm.

Annealing with Joule heating shows similarities to *Rapid Thermal Annealing (RTA)*. During RTA process, the wafers are heated up to 1300°C for very short time with high power lamps, and results obtained with RTA are different than those

obtained with conventional furnace heating. Since early 80s, intensive studies about RTA of polysilicon have been done [73]. Annealing of polysilicon at high temperature (1100-1225°C) for <10 seconds [74], and at low temperatures (525°C) for longer durations (4min.) was reported [75]. Change in electrical and structural properties, and grain growth were observed.

5.3 Reshaping Process

5.3.1 Description of the Reshaping Process

The experiments showed, that the basic setup displayed in Figure 5.1 would fail because of the lack of a good ohmic contact. Only if the polysilicon layer is very thick, the necessary force can be applied to the tip, and also the contact area is increased, but this contradicts with IC process compatibility. To solve this problem, three different ways are proposed in this work. The first one makes use of a probe with a special tip as shown in Figure 5.3. However, this will increase the complexity of the test bench. The second solution requires a slightly complicated fabrication process (Figure 5.4). Depending on the thickness of the sacrificial layer, dimple holes can be opened in the sacrificial layer. If this layer is not thick enough to form a vertical tall base, a trench can be etched in the substrate at the beginning of the fabrication process. Another alternative approach is to fabricate a U-shaped structure with a fixed pad at either end.

Another problem encountered was the difficulty to deform the structure to the desired round shape with only two probes. This problem can be overcome with employing a third probe as shown in Figure 5.5. Actually, this case brings up the real power of the reshaping technology. One can use more than two probes to give *exotic* shapes to the structure in three dimensional world (Figure 5.6).

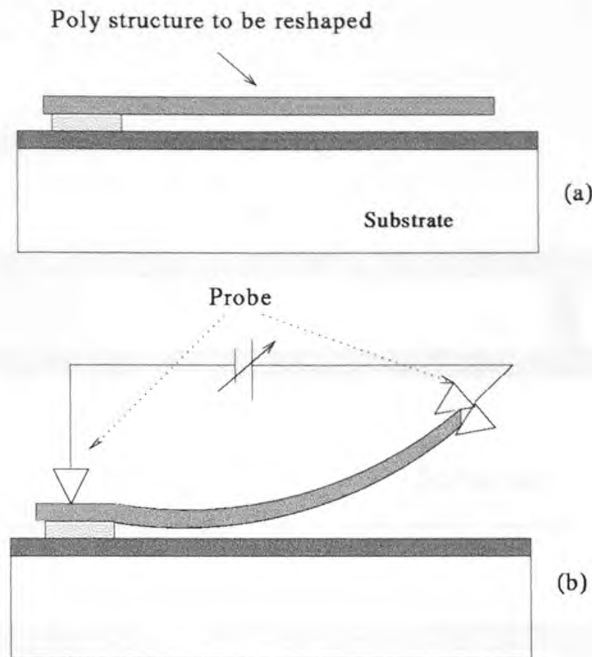

Figure 5.3 Reshaping with a special probe.

5.3.2 Experimental Results

In order to investigate the reshaping process, the micromirror structure shown in Figure 5.7 was used. While the thermal power was applied through the probe pads, the actuators were lifted and brought to the desired position by lifting the mirror platform (Figure 5.8). The edge of the platform was elevated by 350 μm, where the angle was $\alpha \approx 45°$ (for the definition of α, see Figure 5.1). Voltage was applied between two pads as a pulse with varying pulse width, and the actuators were annealed with Joule heating due to the current passing through them. Then the mirror platform was released and the deflection of the platform edge with respect to the substrate was measured. For large displacements, the laser-photodiode setup shown in Figure 5.9 was utilized, while for small displacements the focus of the optical microscope was used.

Figure 5.10 and Figure 5.11 show, that the structures can be deformed in complicated 3D shaped and it is possible to give an initial angle of 45° and 90° to

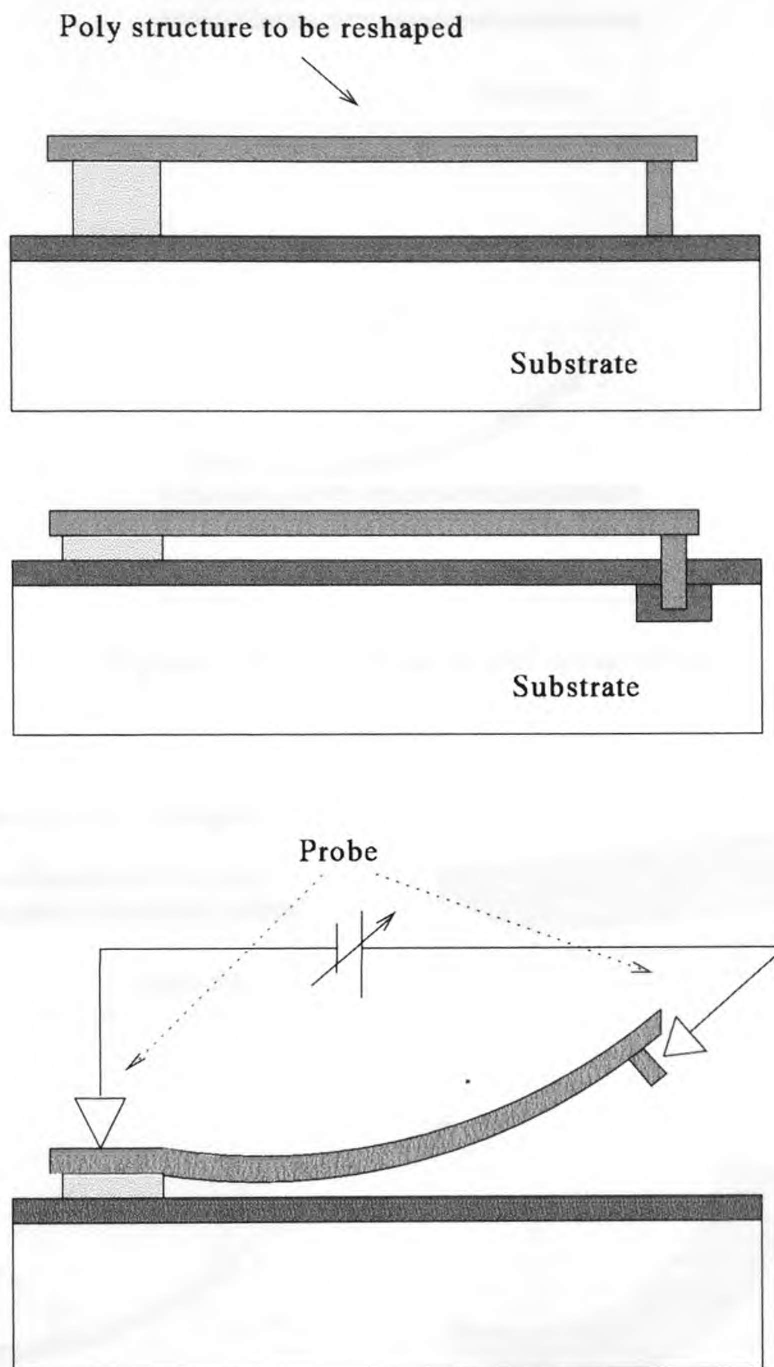

Figure 5.4 Fabricating dimple as a base to make an ohmic contact with the tip.

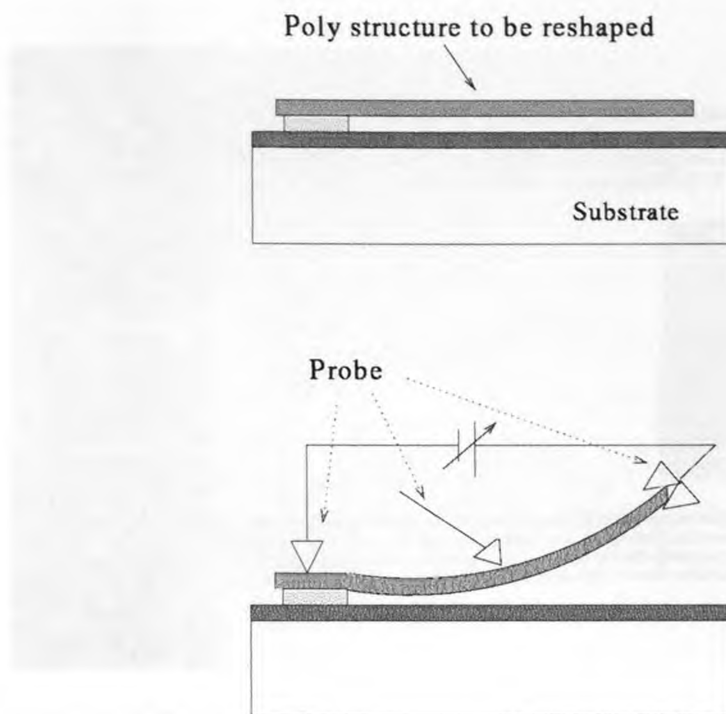

Figure 5.5 An alternative reshaping setup.

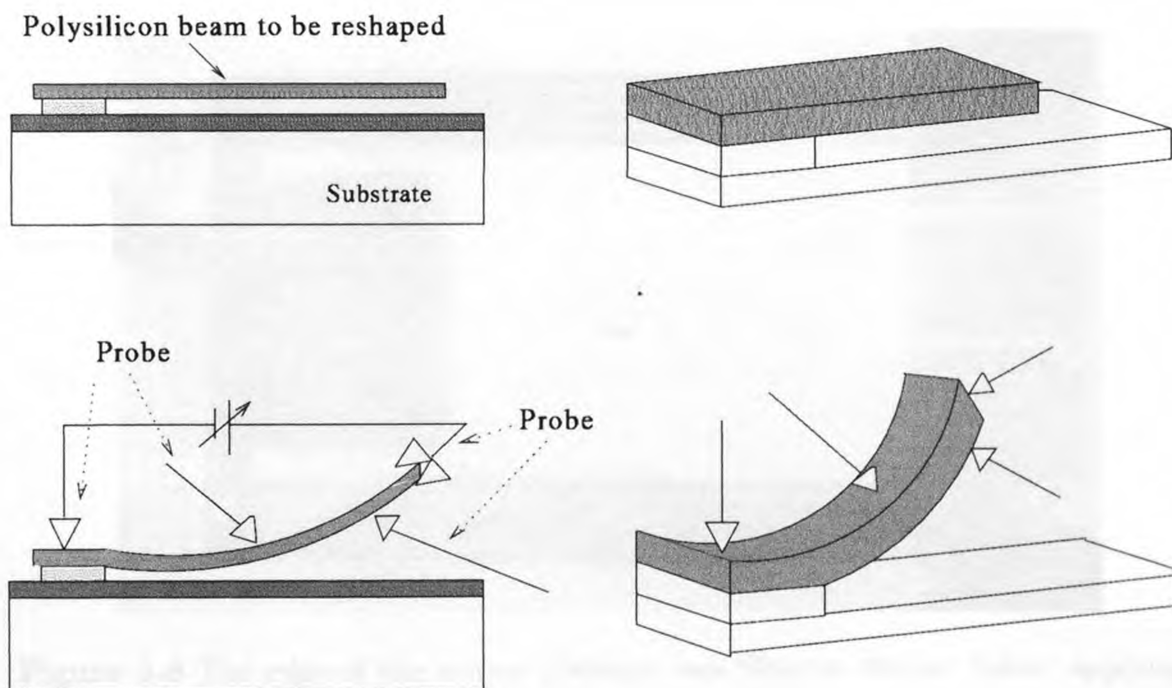

Figure 5.6 Setup for three-dimensional reshaping with many probes.

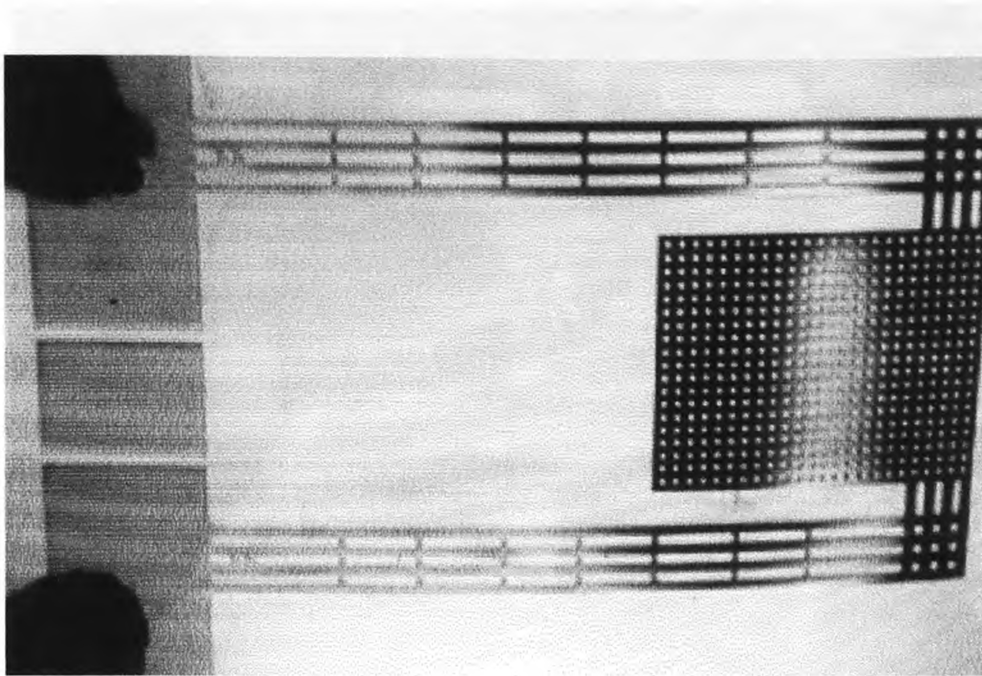

Figure 5.7 Released actuators and mirror platform before reshaping.

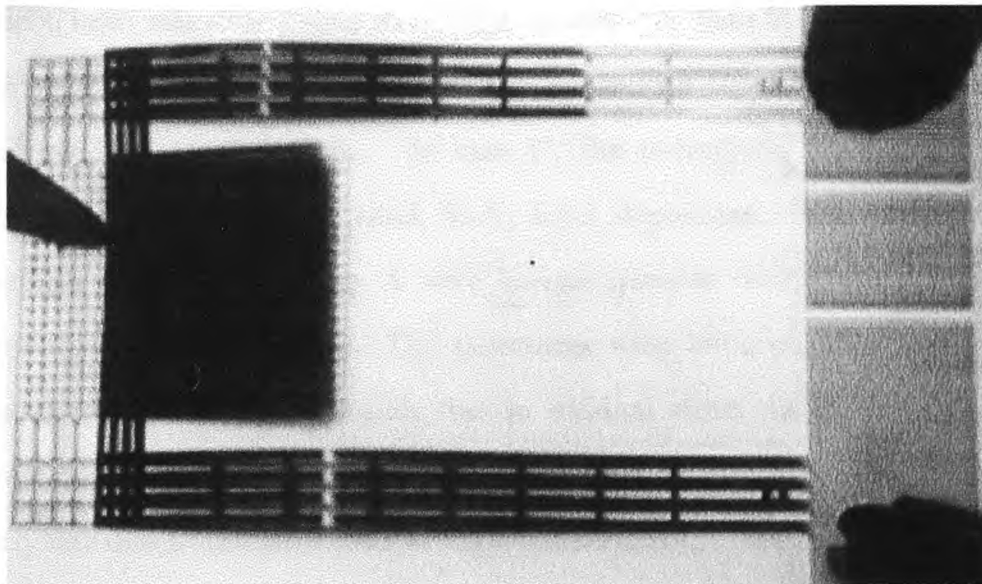

Figure 5.8 The edge of the mirror platform was lifted $\approx 350\mu m$ before applying thermal power.

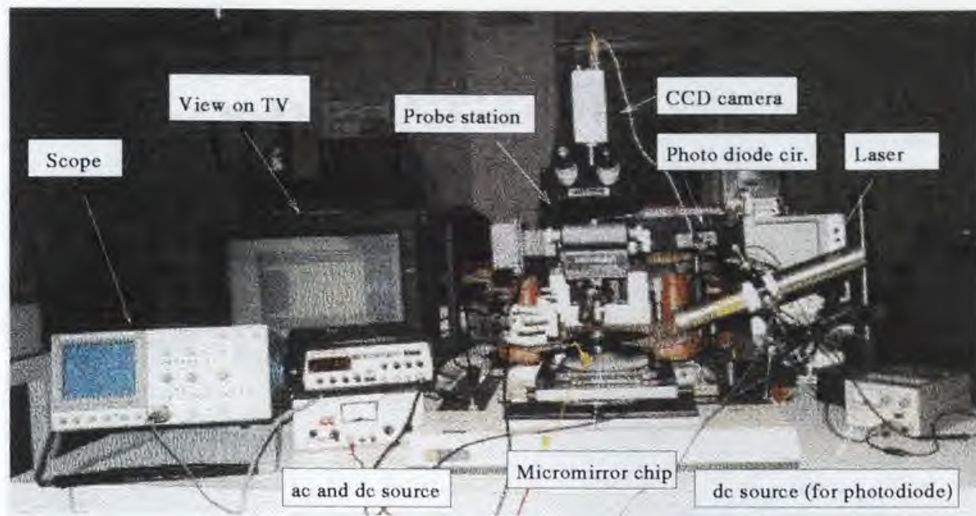

Figure 5.9 Laser-Photodiode setup to measure micromirror deflection

the micromirror platform. Even an angle larger than 90° is possible (e.g. 120° as displayed in Figure 5.12).

Three sets of samples (A, B and C) were prepared 5.1. The detailed process flow for all three cases are given in APPENDIX B. In case A, 1.6μm thick LPCVD polysilicon layer was only doped from solid phosphorus disks at 950°C for 2 hours in O_2 rich environment, while in case B, the polysilicon layer was doped at 950°C and annealed at 1100°C in N_2. In case C, the polysilicon layer was doped at 950°C, followed by a 2000 Å thick Si_3N_4 layer deposition. The structures with monomorph actuators in group A were bowed upwards mainly due to the stress gradient throughout the layer. The structures with bimorph actuators in group C were also bowed upwards mainly due to residual stress discussed in Chapter 3 (Figure 5.14). The mirror platform and actuators in group B were found to be perfectly flat due to the annealing at high temperature.

The structures were reshaped in two different ways. First a 1 second long voltage pulse with increasing voltage values were applied to the test structure, the percentage of deformation was measured with increasing electro-thermal power and

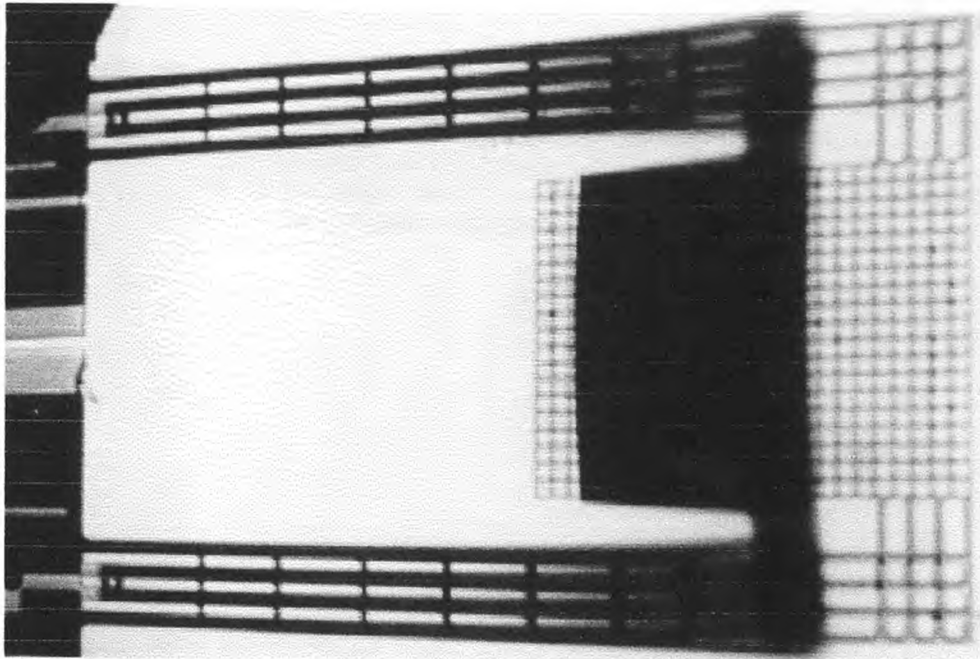

Figure 5.10 Actuators and mirror platform reshaped at 45°.

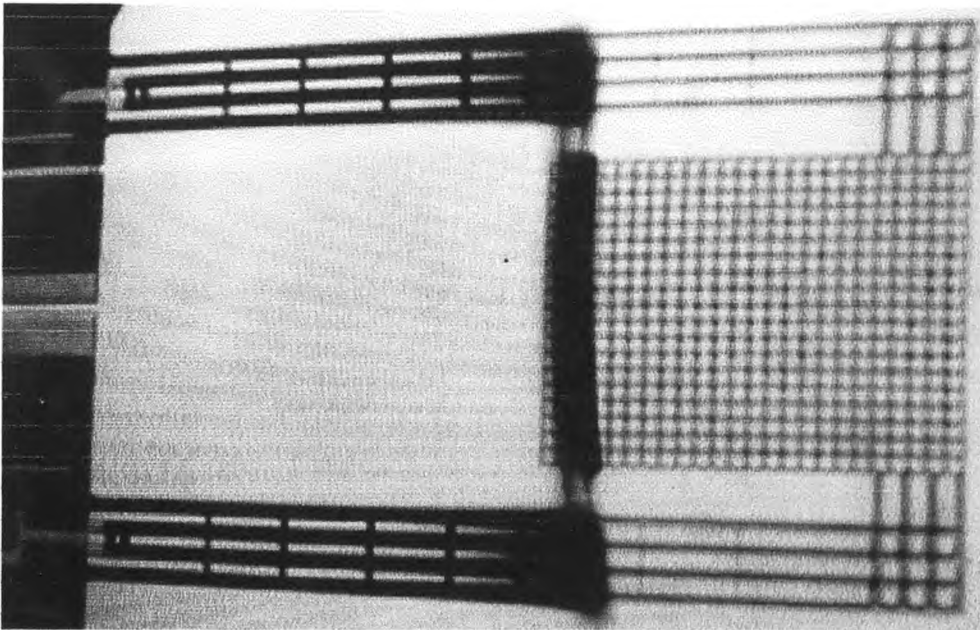

Figure 5.11 Actuators and mirror platform reshaped at 90°.

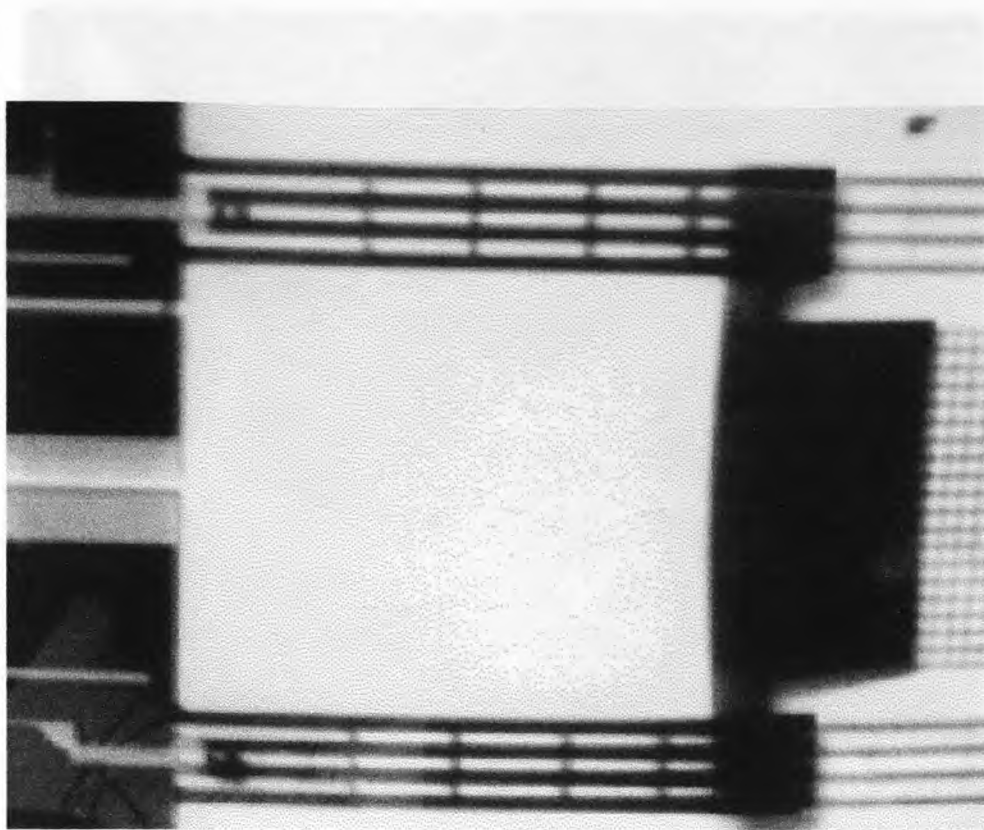

Figure 5.12 Actuators and mirror platform reshaped at 120°.

Table 5.1 Three sets of samples used for investigation of the reshaping process.

Sample	Process
A	Polysilicon Layer Doped at 950°
B	Polysilicon Layer Doped at 950° Annealed at 1100°
C	Bimorph Bottom: Polysilicon Doped at 950° Top: 1200Å LPCVD Si_3N_4

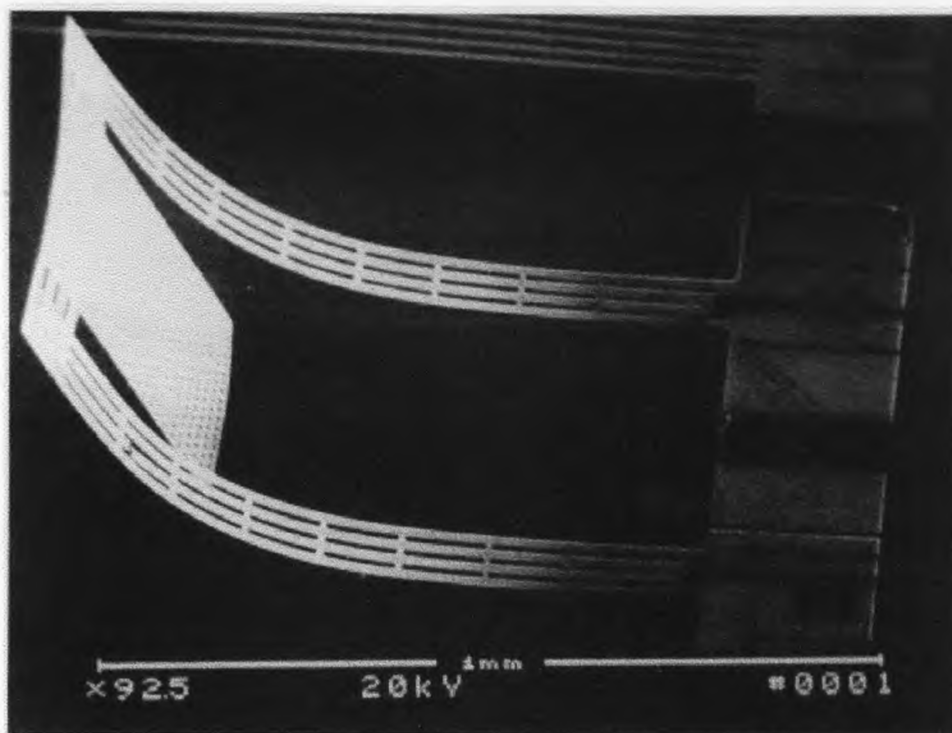

Figure 5.13 SEM photograph of a micromirror reshaped at 45°.

current. The percentage of deformation was defined as the ratio of the deflection of the deformed actuator with respect to the initial deflection given with the probe. All three types of devices were reshaped with incremental power and the deformation vs. input power and input current curves are give in Figure 5.15 and Figure 5.16, respectively. From the figures, one can see that *phosphorus doped and annealed* structures (samples A) can be reshaped with lower input power and input current compared to input power and input current necessary to deform *phosphorus doped only* polysilicon structures (samples B).

Figure 5.15 displays, that significantly lower power is required to deform structures coated with a Si_3N_4 layer (samples C). This is mainly because of the low thermal conductivity of Si_3N_4 layer, which causes additional temperature increase, and the annealing starts at lower power values.

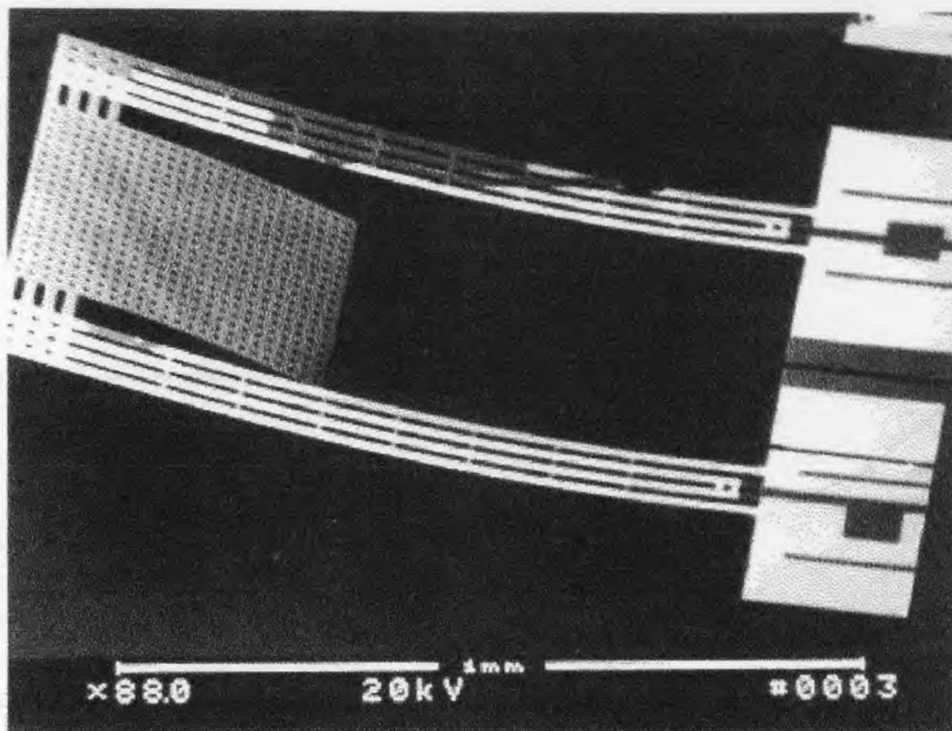

Figure 5.14 Bimorph micromirror after release.

Another group of actuators were reshaped with a single 1 second long voltage pulse high enough to cause different amounts of permanent deformation. The effect of incremental annealing is compared with one step annealing in Figure 5.17 and Figure 5.18. From these figures, it can be seen, that the same amount of permanent deformation occurs at lower input power values, if the electro-thermal power is applied in one step. This may be because of previous recrystallization, and grain growth already inserted into the structure in incremental annealing case. These are believed to make further recrystallization and permanent deformation require higher power.

The experiment was repeated with a pulse with 4, 10 and 30 second durations. Test structures were reshaped with incremental pulses and deformation vs. input power and input current plots are given in Figure 5.19, Figure 5.20, Figure 5.21, and Figure 5.22.

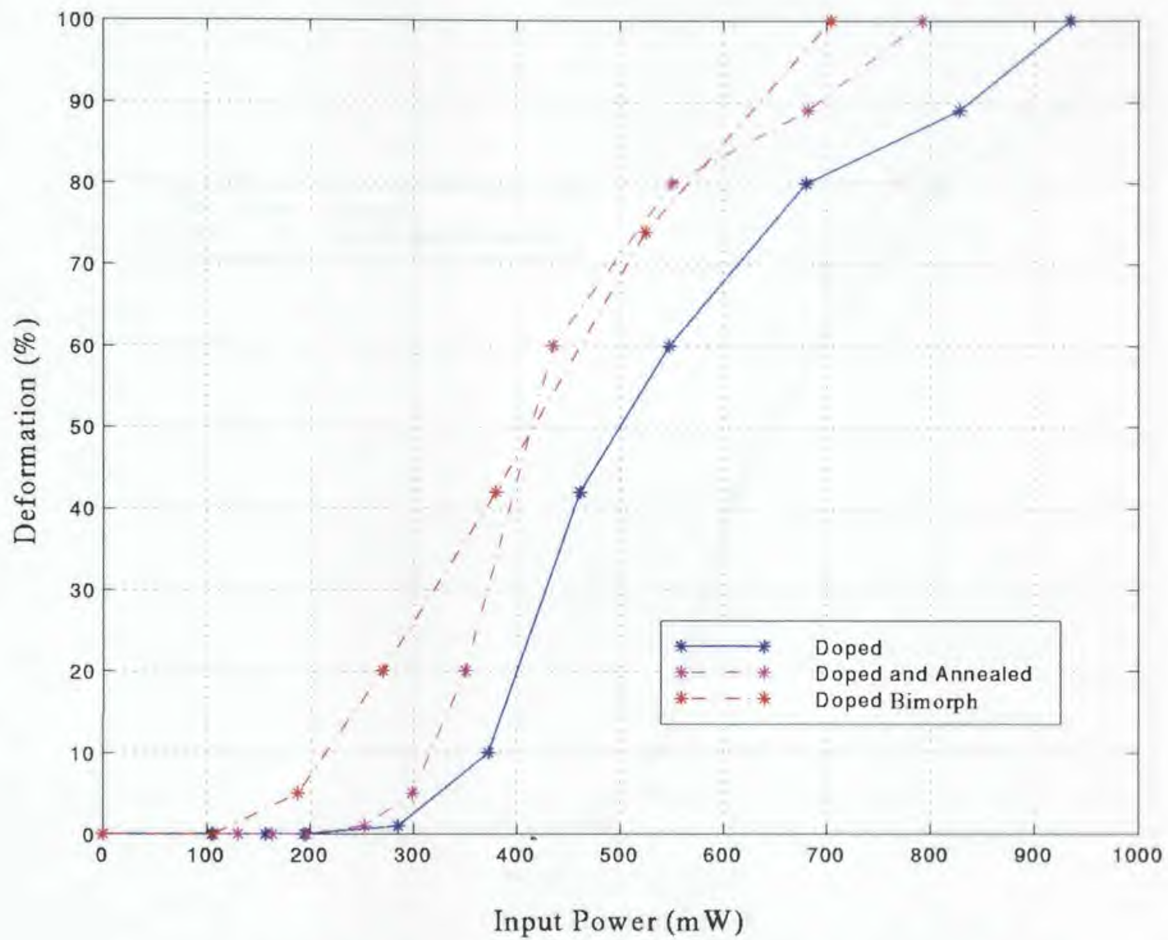

Figure 5.15 Deformation vs. input power. Pulse duration=1 sec

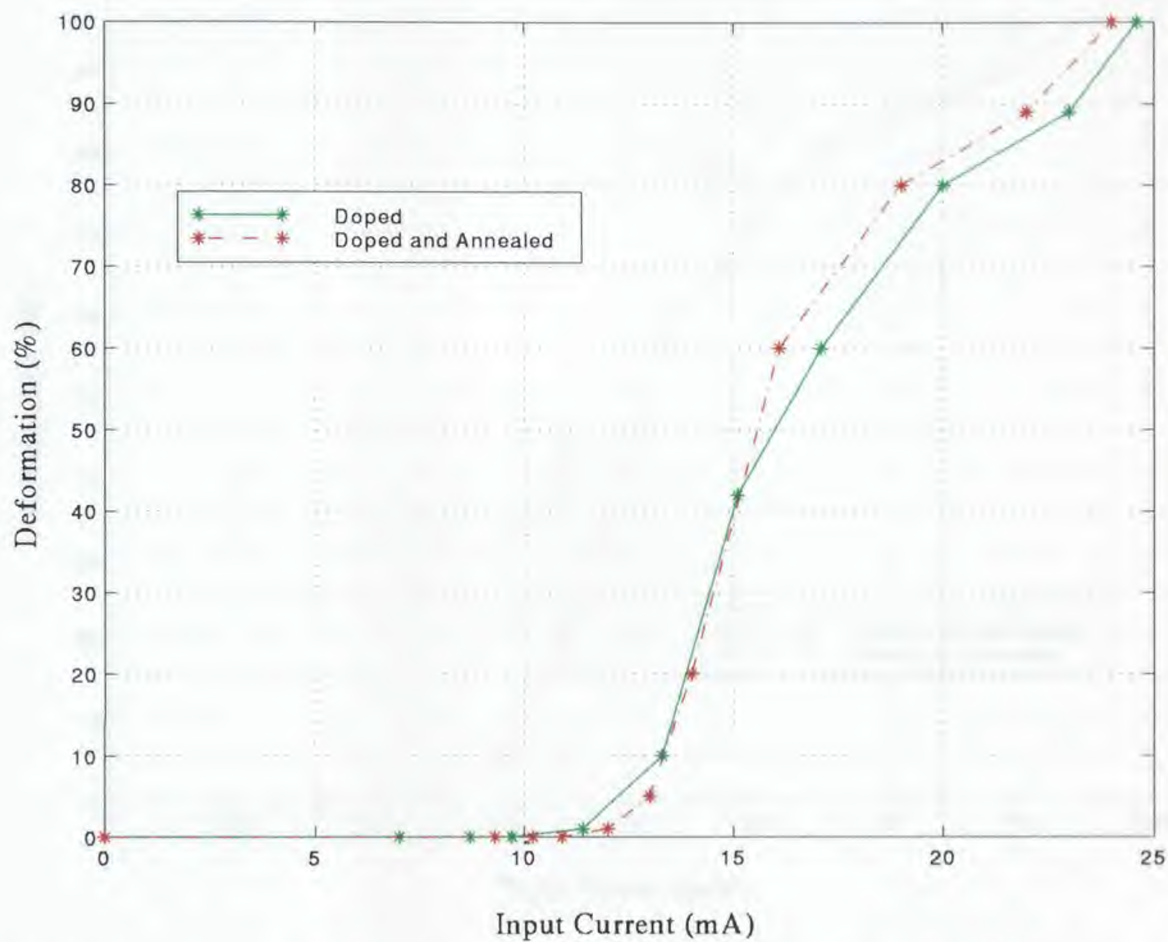

Figure 5.16 Deformation vs. input current. Pulse duration=1 sec

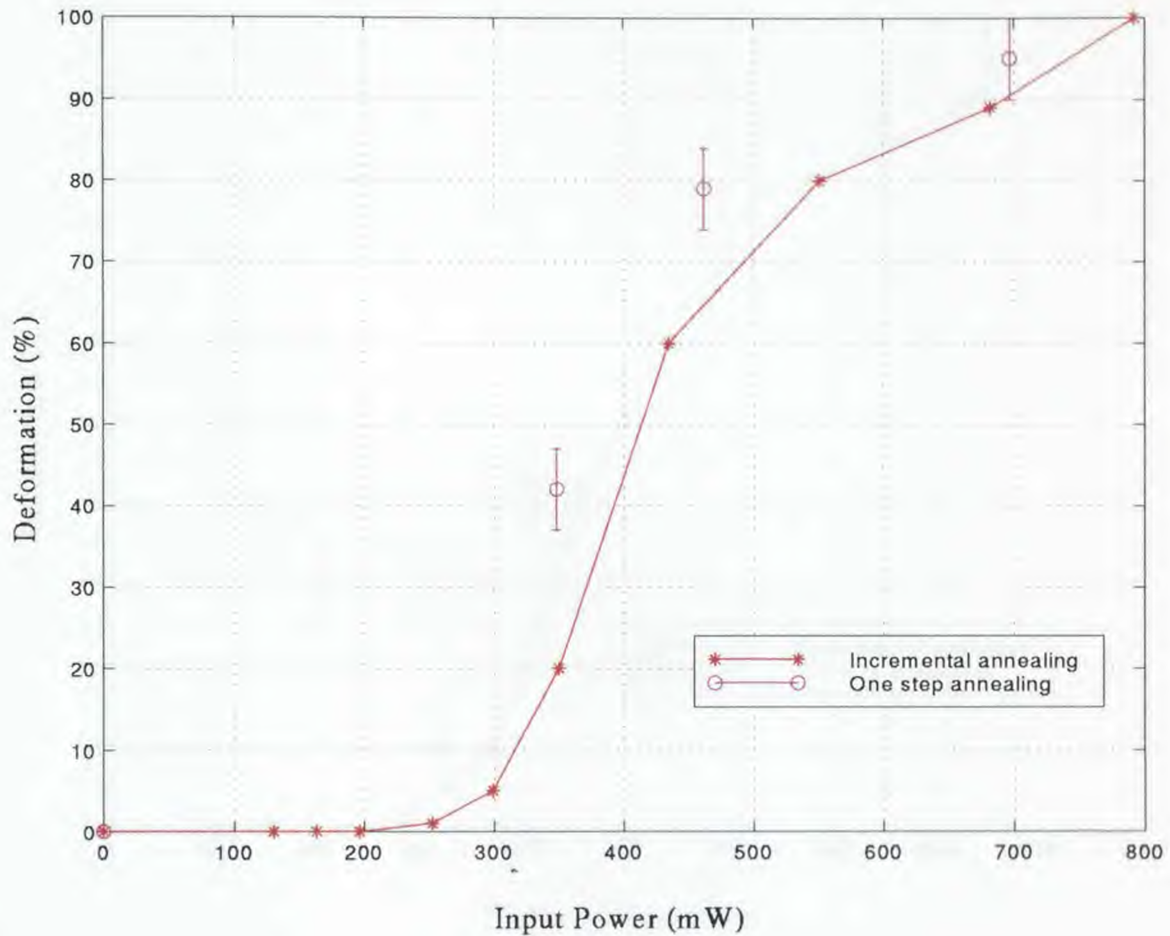

Figure 5.17 Input power vs. Deformation. Polysilicon layer was doped at 950°C and annealed at 1100°C. Comparison of incremental annealing with one step annealing. Pulse duration=1sec

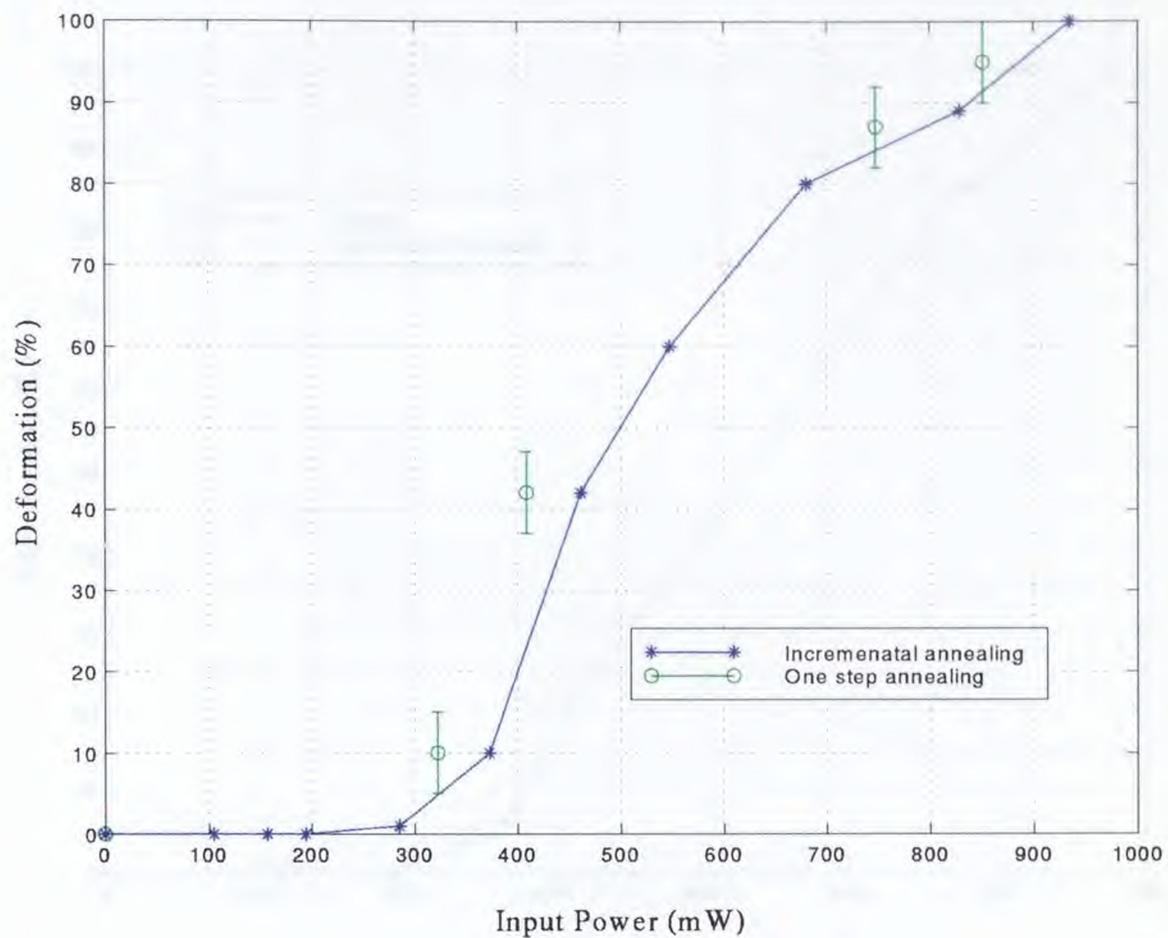

Figure 5.18 Deformation vs. input current. Polysilicon layer was only doped at 950°C. Comparison of incremental annealing with one step annealing. Pulse duration=1sec

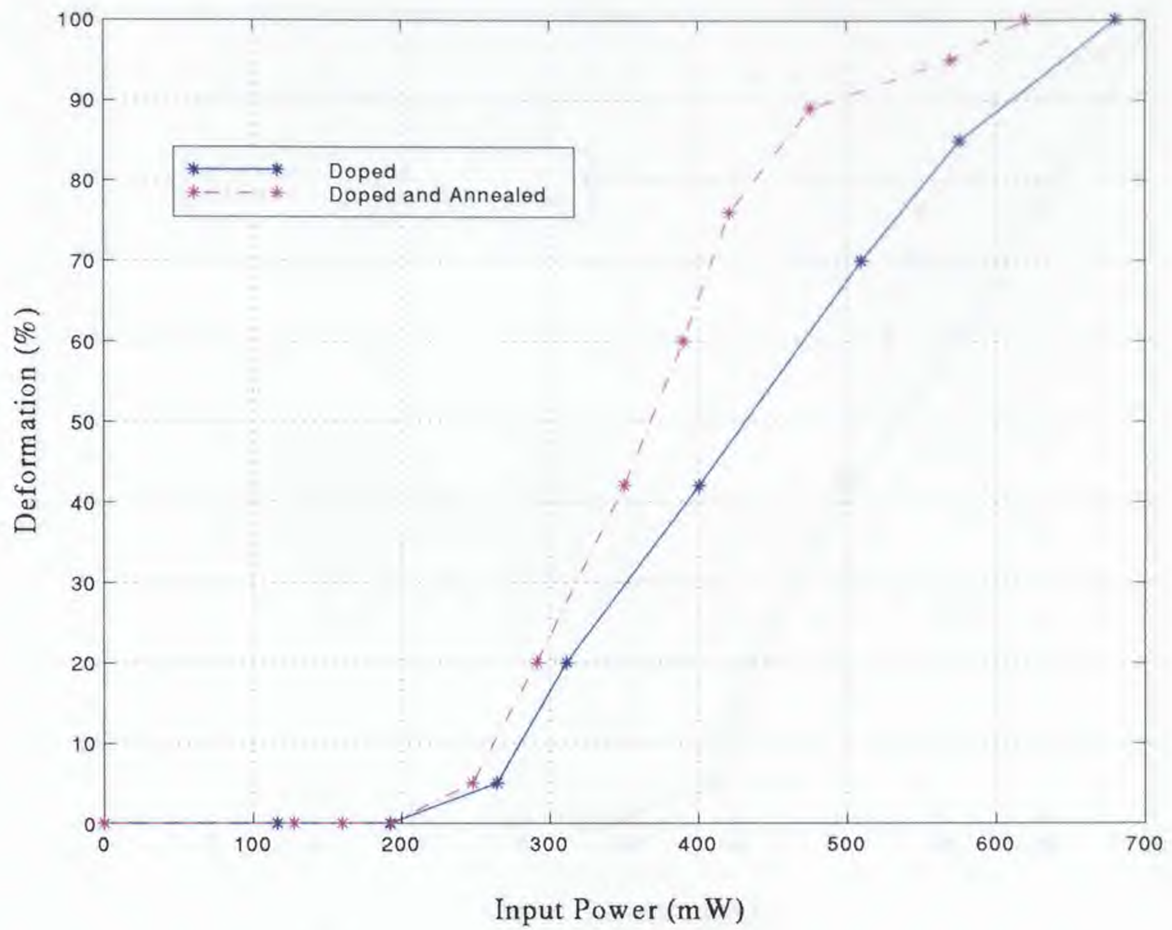

Figure 5.19 Deformation vs. input power. Pulse duration=4 sec

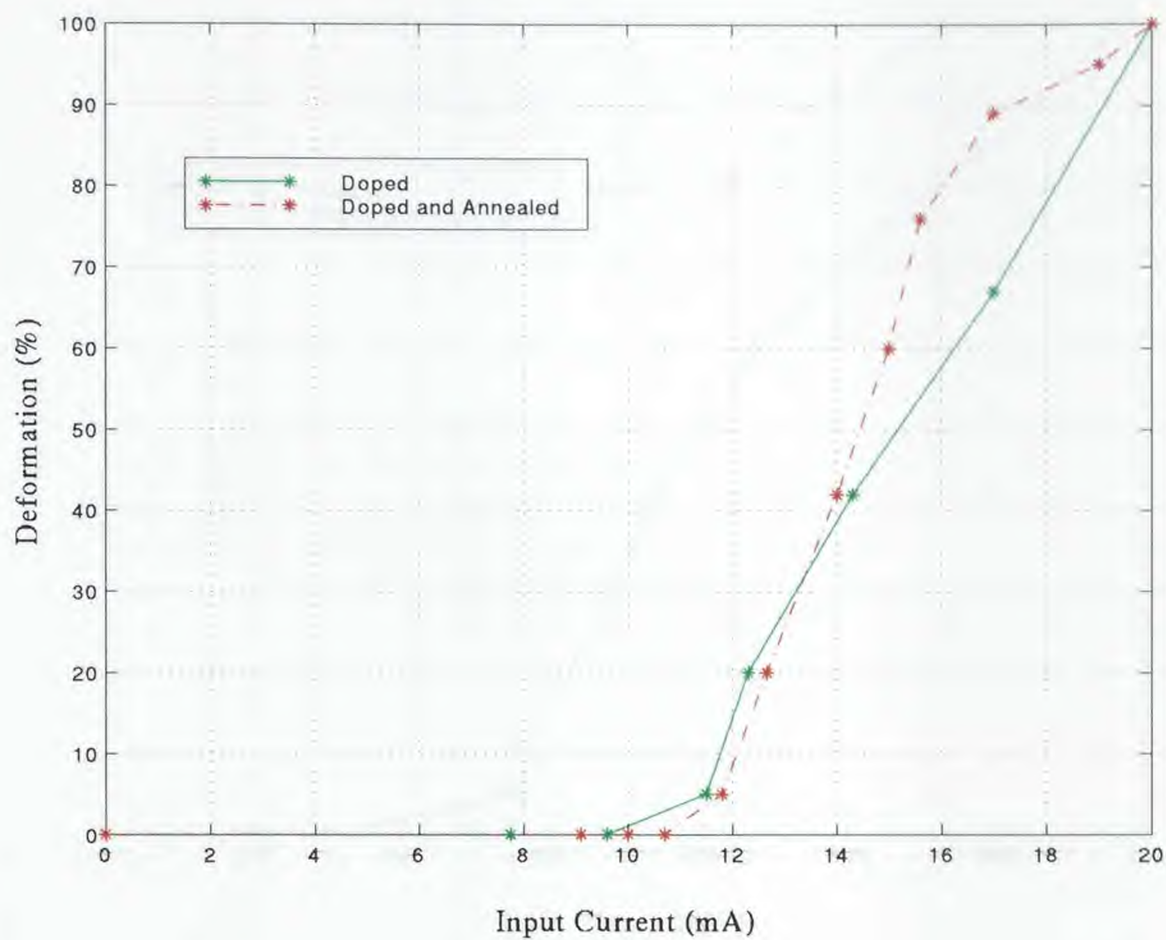

Figure 5.20 Deformation vs. input current. Pulse duration=4 sec

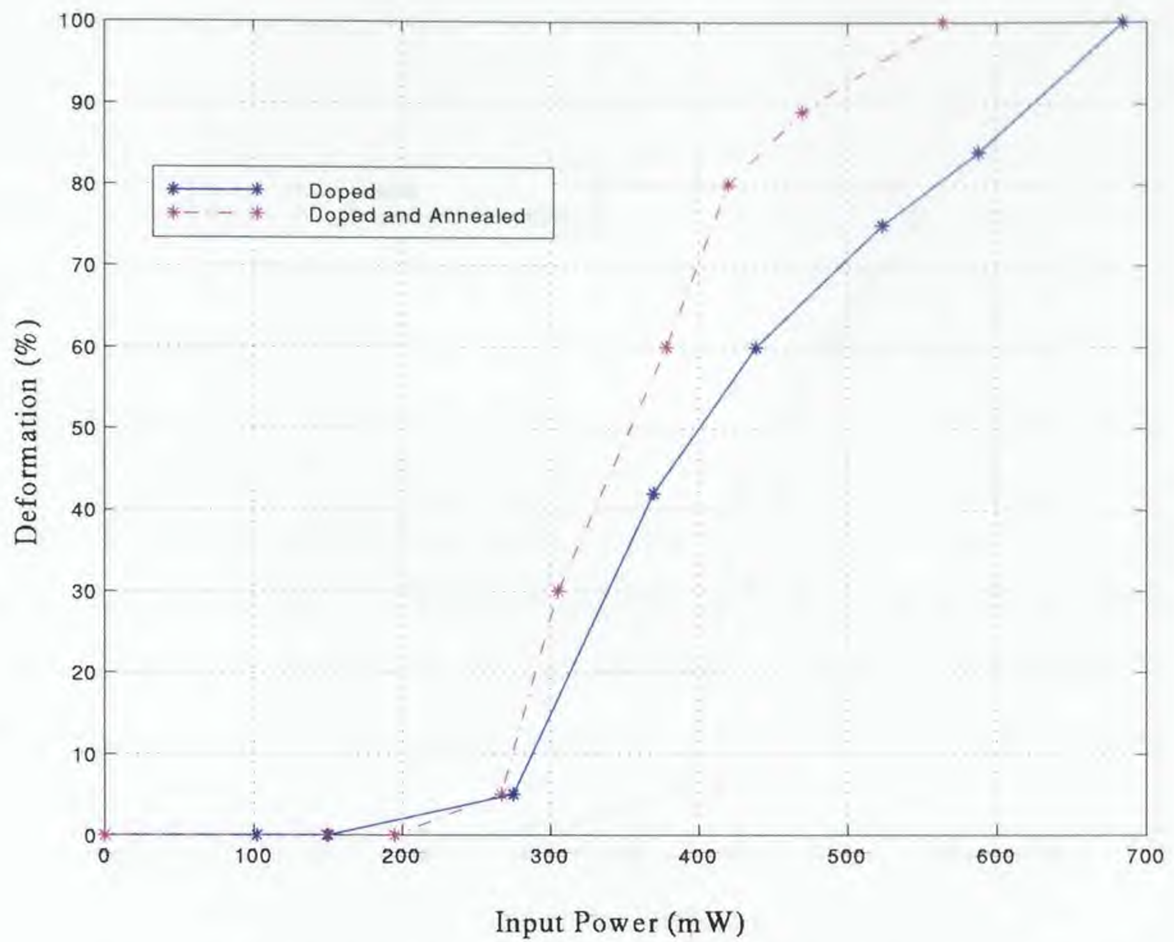

Figure 5.21 Deformation vs. input power. Pulse duration=10 sec

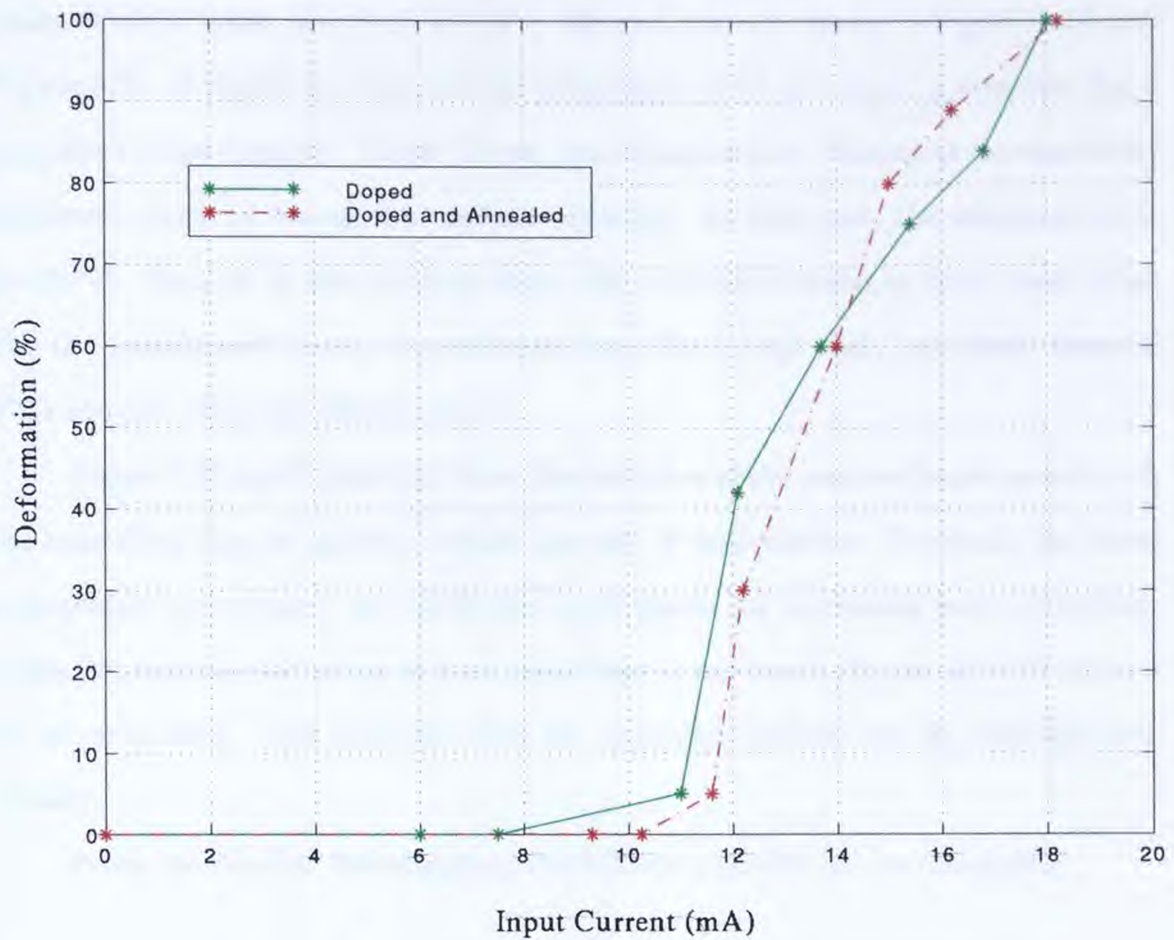

Figure 5.22 Deformation vs. input current. Pulse duration=10 sec

Figure 5.23 displays the relationship between the applied voltage and the measured current for the undeformed (original) and deformed structures. At low voltage values, the resistance of the deformed structures is higher than original structures because of the additional stress generated during the lifting the mirror platform with the probe tip. Up to 8 mA, both currents are almost equal. Above this value one can conclude, that the reshaping process starts. The deformation vs. pulse duration plots are given for four different current values in Figure 5.24 and Figure 5.25. A significant deformation takes place at 13 mA input power even for a very short pulse duration. Above 15 mA, the actuators start shining at the elastically deformed region in orange due to Joule heating. At this spot, the temperature is $\approx 625°C$. Because of this heating effect, the resistance values in both cases drop. For the undeformed beam, the substrate acts like a heat sink, but static thermal FEA showed, that this effect is small.

Figure 5.26 and Figure 5.27 show the variation of the required input power with the annealing time to create a certain amount of deformation. To obtain the same deformation percentage, one needs less input power for increasing pulse durations, while this decrease saturates at 4 sec, and there is not much change after 10 sec and 30 sec annealing. This indicates that the annealing process can be achieved very quickly.

From the detailed investigation, the following results can be concluded:

- Elastic stresses can be annealed by Joule heating, where both recrystallization, grain growth and plastic deformation play a major role.
- Increasing electro-thermal power causes increased deformation.
- The initial crystalline structure effects the required input power.

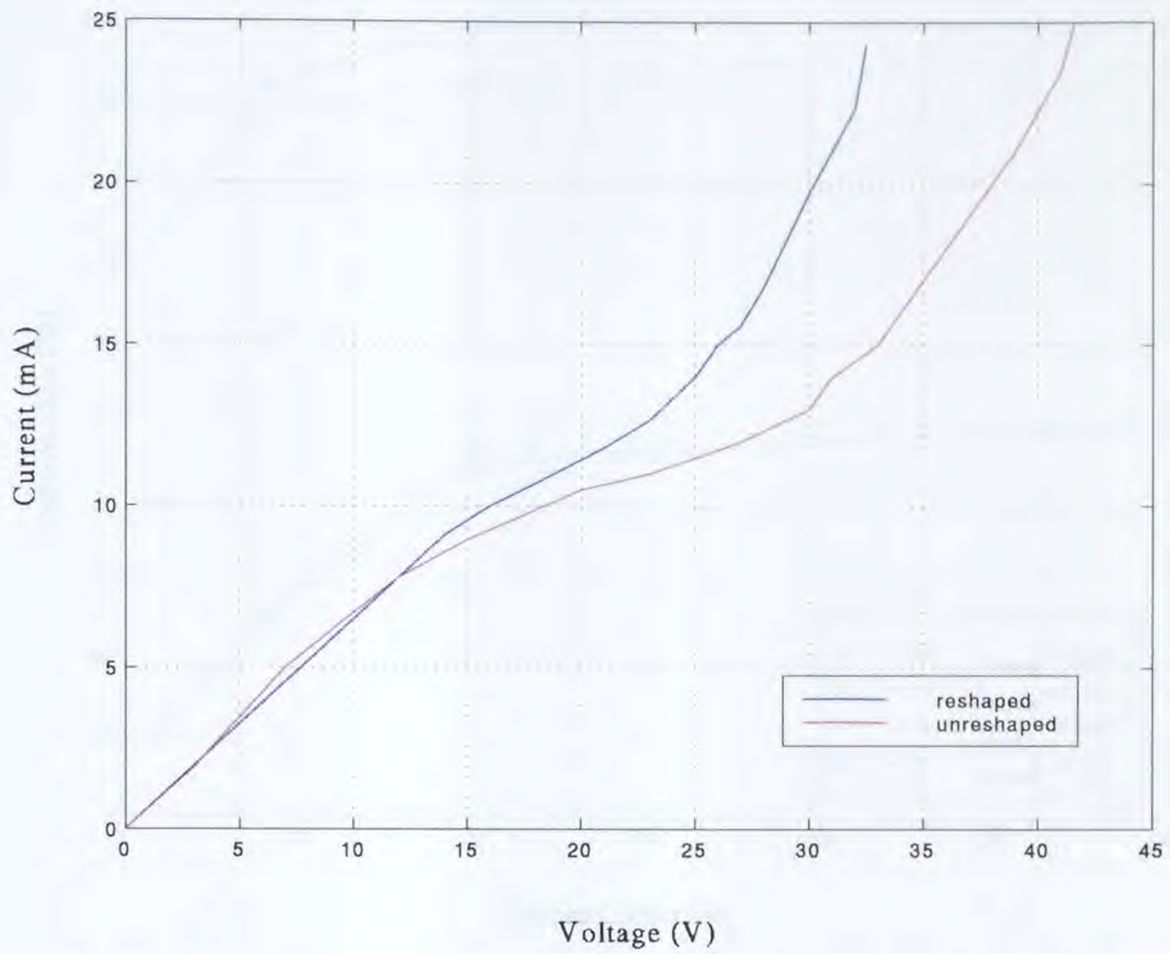

Figure 5.23 I-V characteristics of the actuators under investigation.

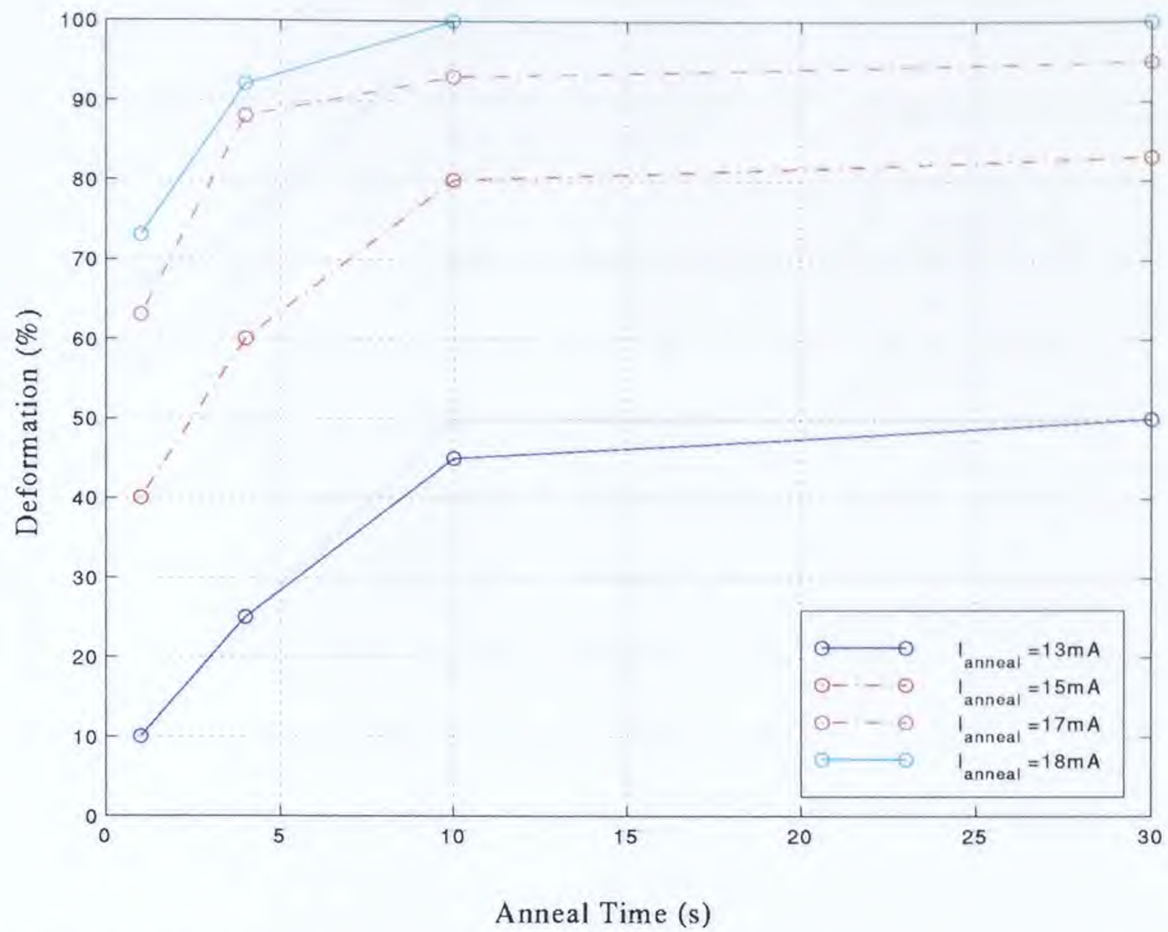

Figure 5.24 Deformation versus anneal time of the samples in group A for four different current values.

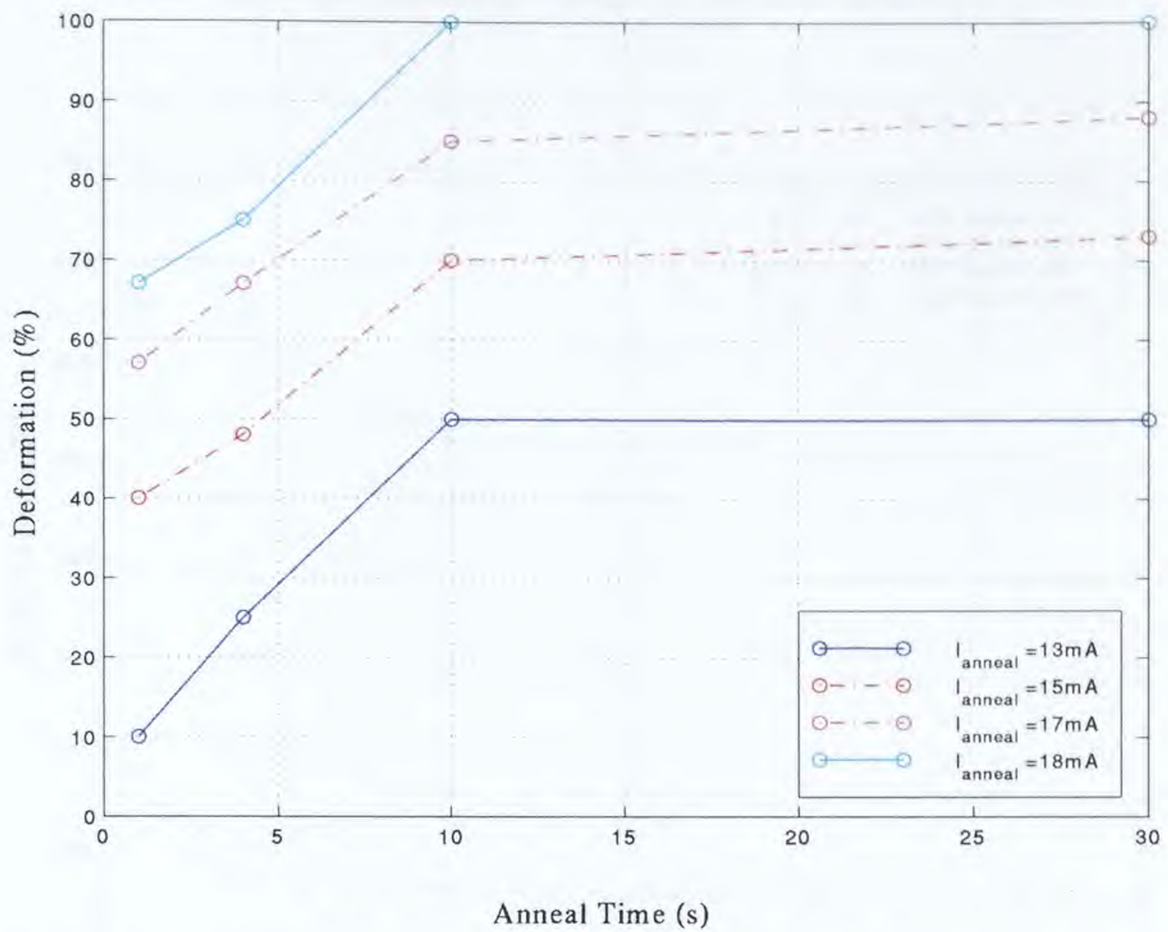

Figure 5.25 Deformation versus anneal time of the samples in group B for four different current values.

- A 3×10^4 A/cm^2 current density supplied for 4 sec. is sufficient to achieve a complete reshaping. Further increase in annealing time does not effect the deformed shape significantly.

- The ohmic resistance of the deformed structures is lower than the initial (undeformed) one after the annealing occurs. Moreover, the I-V deviates from the linear Ohm's law indicating a change in polysilicon properties.

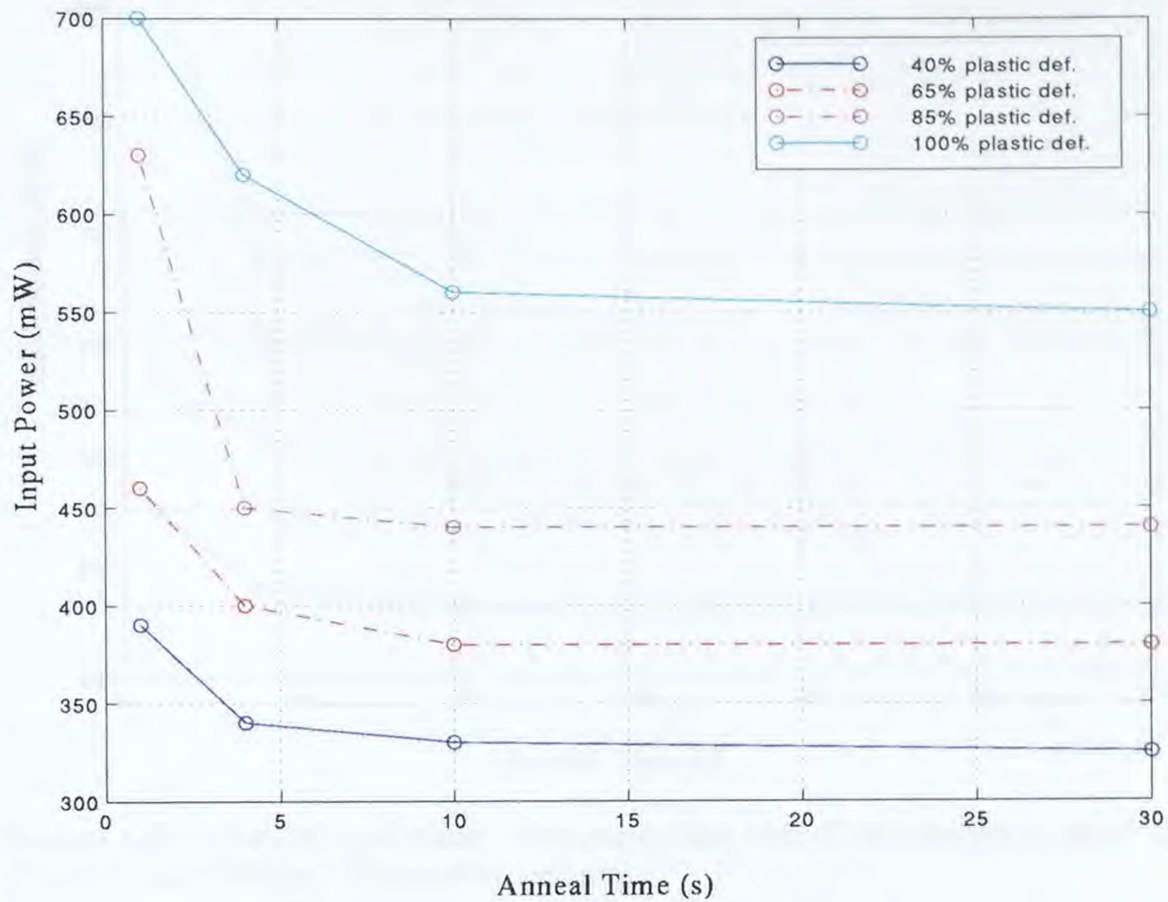

Figure 5.26 Required input power versus annealing time of the samples in group A to obtain four different deformation amounts.

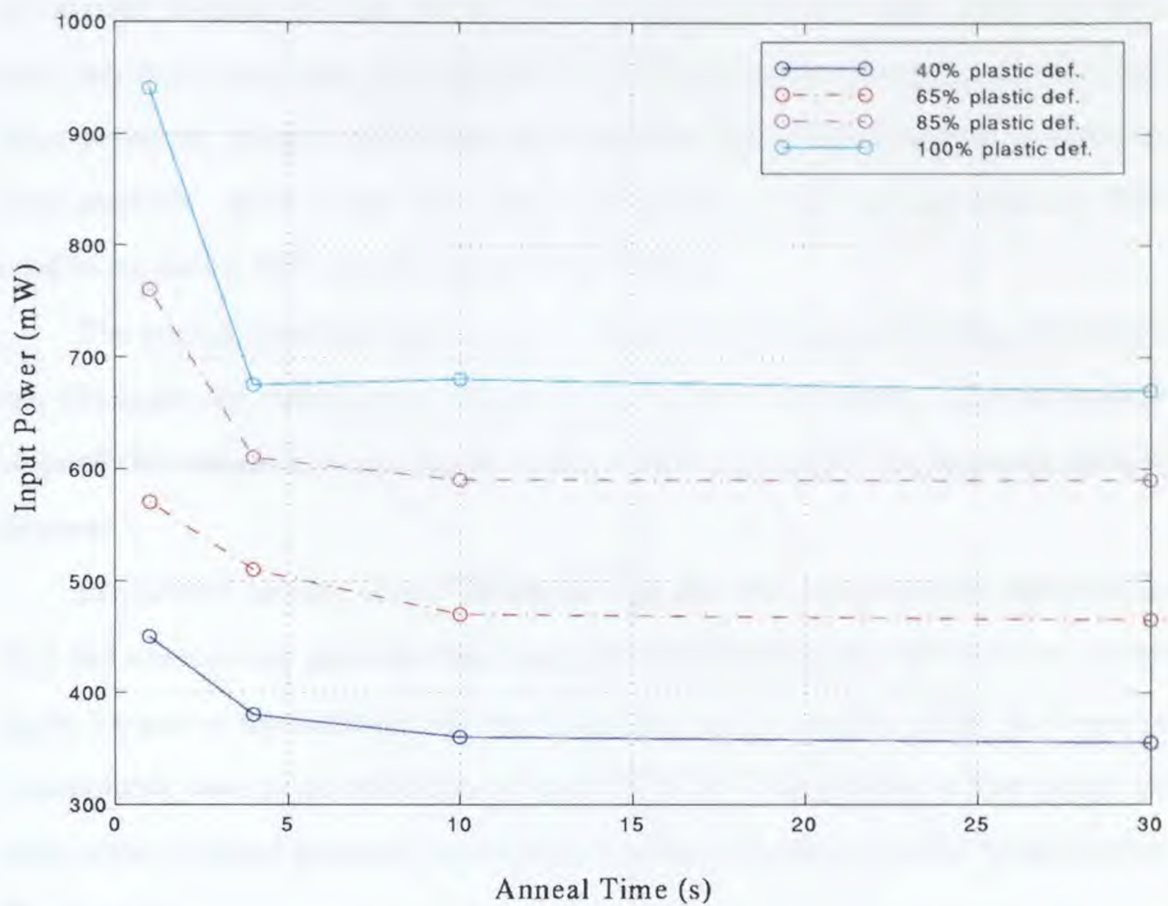

Figure 5.27 Required input power versus annealing time of the samples in group B to obtain four different deformation amounts.

5.4 Application: Reshaped Micromirror

Micro-opto-electro-mechanical (MOEM) systems become more and more available for a variety of applications. Such applications go beyond single devices to include whole optical systems on a chip, comprising mirrors, gratings, Fresnel lenses, and shutters [76]. Today most of them are fabricated with available IC processes, which allow only couple of micron high devices. Most of these devices have a hight of couple of hundred microns, so they are fabricated as horizontal structure. They are freed after sacrificial layer etch, and an actuation mechanism flips them up and positions them precisely. Hinges and locks make sure that the released devices are kept at their positions. Most of the time, these mechanisms occupy a large area and they need to be driven with complicated control signals.

The micromirror structure is a good example to show, how reshaping technology can eliminate the silicon area consuming complicated actuators. The fabrication steps of the reshaped structures are much more simpler that the reported MOEM devices.

In previous section, it was displayed, how the structure could be deformed so that the micromirror platform was tilted at the desired angle. 45° is a very useful angle, because a micromirror tilted at this angle can be used to couple the beam of a monolithic laser to an optic fiber (Figure 5.28), or a signal from a fiber lying in a bulk-micromachined groove to another fiber positioned perpendicular to the surface (Figure 5.29).

External-cavity semiconductor lasers are of interest for applications such as laser linewidth narrowing, emission wavelength tuning, and laser mode locking. For this purpose, micromirrors standing vertically (90°) are required (Figure 5.30).

Angles larger then 90° are also useful. An optical beam from a surface photodiode can be directed to a subject (e.g. lens, optical fiber) by utilizing a micromirror tilted 135° from its original position.

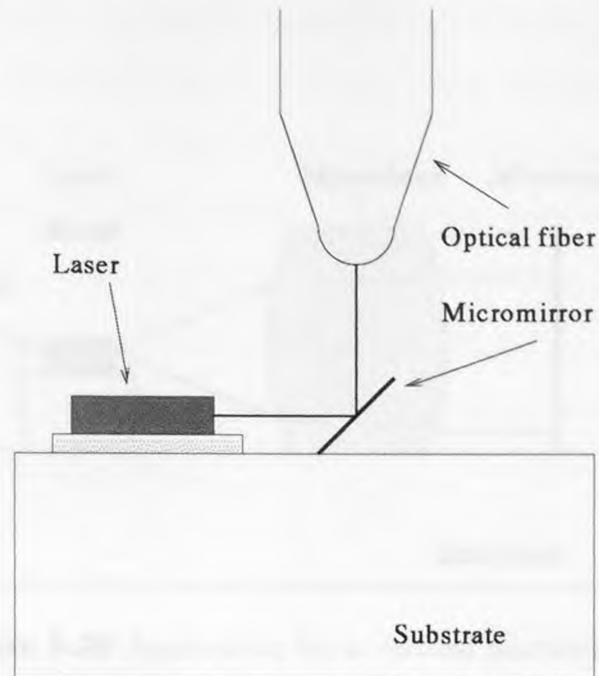

Figure 5.28 Application # 1 for 45° tilted micromirror.

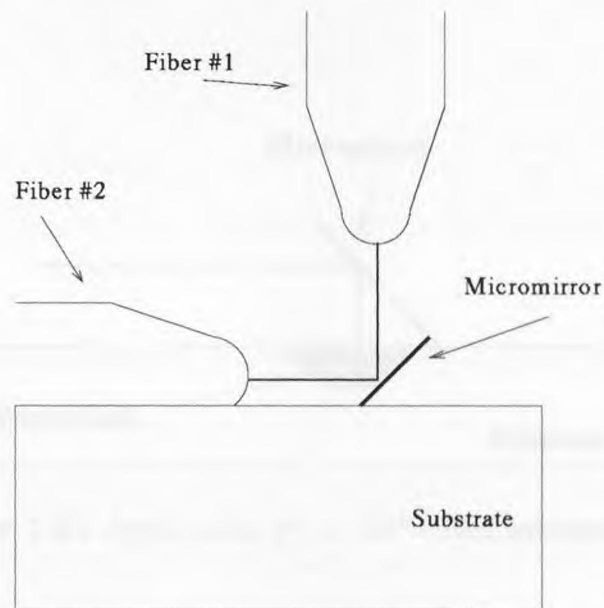

Figure 5.29 Application # 2 for 45° tilted micromirror.

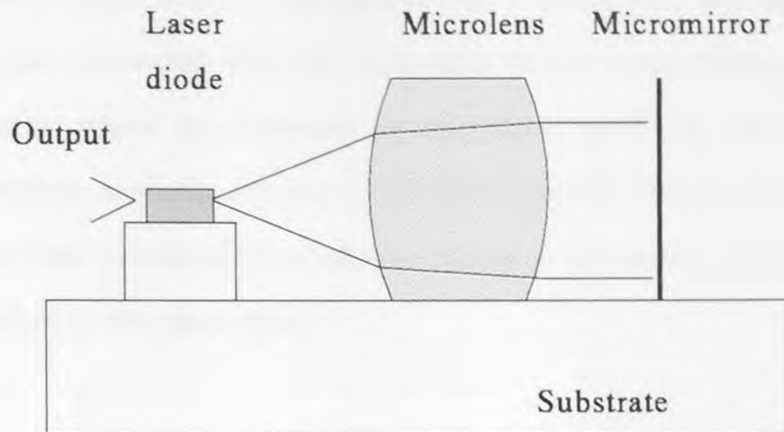

Figure 5.30 Application for a vertical micromirror.

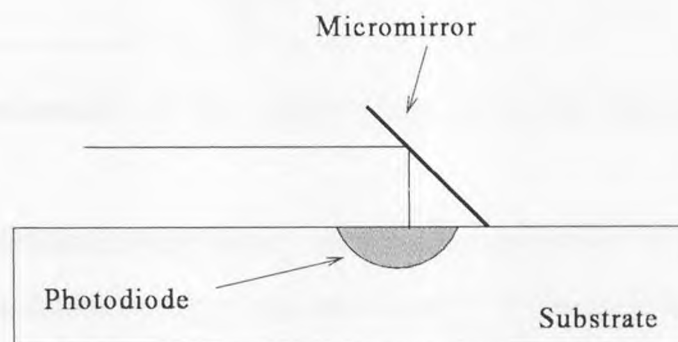

Figure 5.31 Application for a 135° tilted micromirror.

The micromirror can be driven electro-thermally and/or electrostatically. To investigate static and dynamic structural response of the micromirror, sample structures from all the three groups (A, B and C) were reshaped so that the mirror platforms[1] were tilted $\approx 45°$. Throughout the experiment, the deflection of the micromirror was measured with the laser-photodiode setup shown in Figure 5.9. The laser beam, which was focussed on the mirror platform, was reflected from the mirror surface towards a screen-photodiode system (Figure 5.32). The large displacements were measured from reflected image at the screen, while dynamic data were collected with the photodiode.

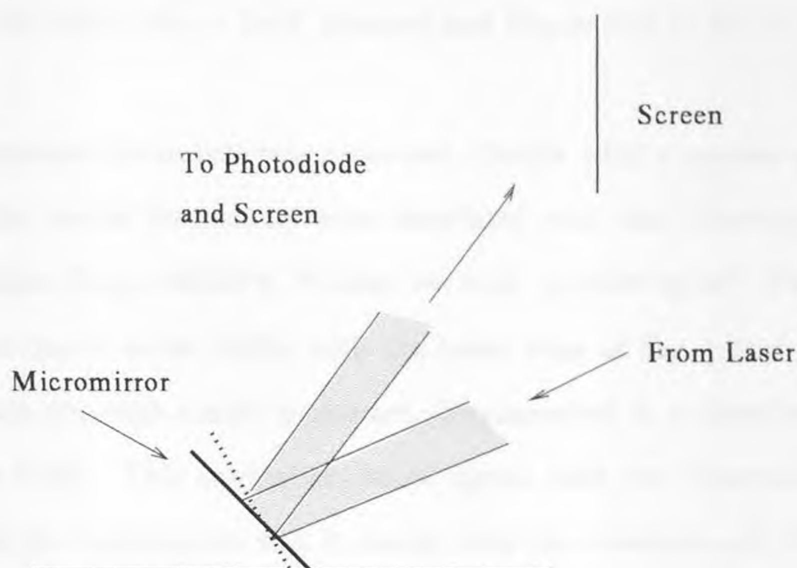

Figure 5.32 Schematic of the measurement setup for the scan angle of the micromirror.

First, the actuators were driven with dc thermal power. A varying dc voltage was applied. The displacement of the micromirrors in group C was found to be the largest, while the response of the structures in group A was less and the displacement of the micromirrors in group B was negligible. This result was expected. The small actuation effect observed at the micromirrors in group A is due to the gradient stress throughout the polysilicon as discussed in Chapter 4. The bimorph actuators in

[1]The size of the micromirror platform is $500 \text{x} 400 \mu m^2$

group C showed a large deflection due to the temperature dependent residual stress as discussed in Chapter 3. The largest scan angle for the micromirror was measured 11° (22° for the deflected laser beam), which corresponds to a $61\mu m$ vertical and $73\mu m$ horizontal displacement of the mirror's upper edge.

To obtain the dynamic response of the micromirror with bimorph actuators, it was driven with an ac signal (10 V in amplitude) with varying frequency combined with 10 V dc voltage. The measured frequency response of the micromirror is plotted in Figure 5.33.

The photodiode response to the reflected laser beam at 10 Hz and 166 Hz were shown in Figure 5.34 (1 div = 2mV, 20msec) and Figure 5.35 (1 div = 2mV, 2msec), respectively.

The resonance frequency was measured 1030Hz with a system quality factor Q of 2.5. The modal frequencies were simulated with the following parameters: Young's modulus E_{Poly}=160MPa, Poisson $\nu = 0.25$, ρ=2300 kg/m^3. The first modal frequency was found to be 740Hz with the lower edge of the mirror platform free and 940Hz with the edge simply supported (displacement in y direction is zero, e.g. $u_y=0$)(Figure 5.36). This simulation result agrees with the observation, that the lower edge of the micromirror was in touch with the substrate all the time. The first four modal frequencies are given in Table 5.2. The modal shapes are given in Figure 5.37 to Figure 5.40.

Table 5.2 The simulated modal frequencies of the reshaped micromirror.

Mode #	Freq. (Hz)
1	940
2	12301
3	13448
4	14203

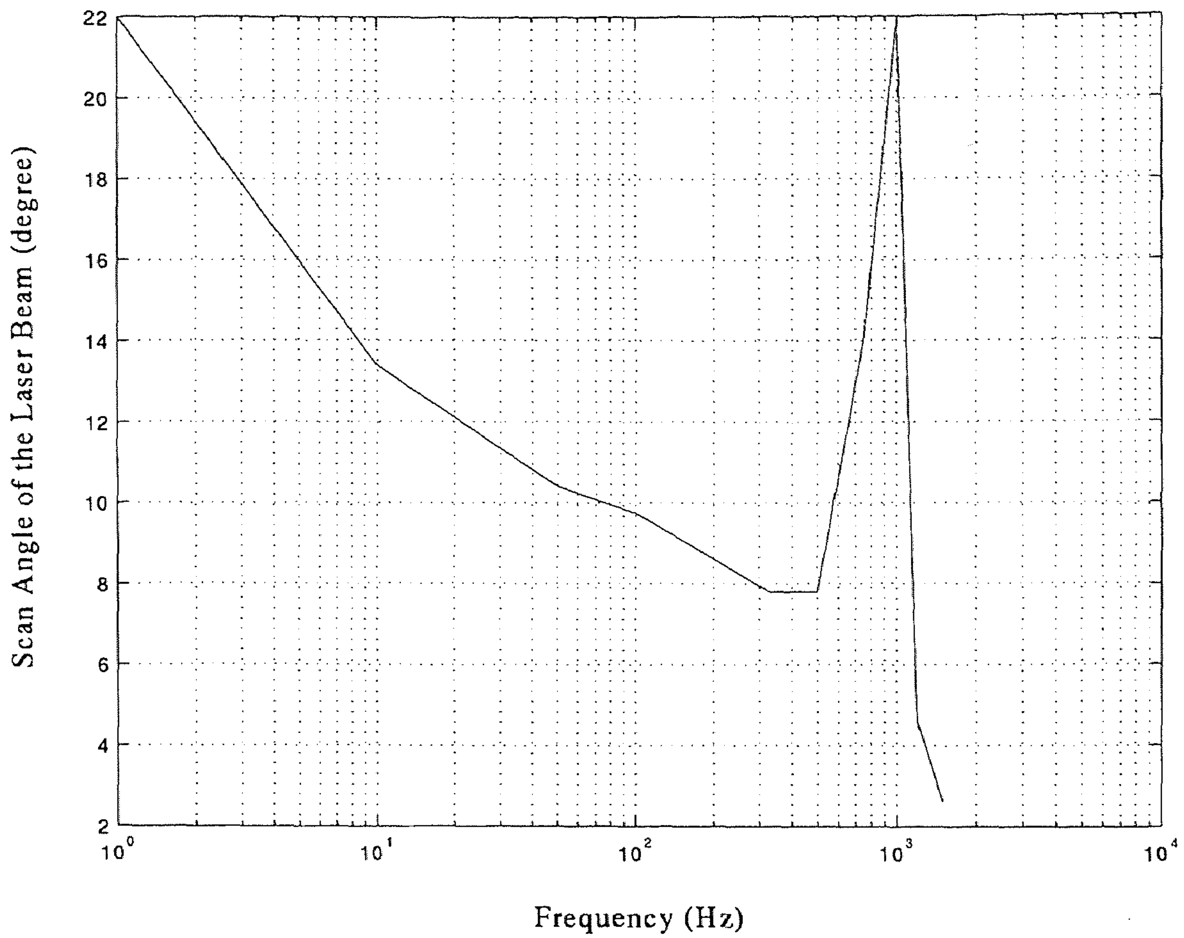

Figure 5.33 Frequency response of the reshaped micromirror with bimorph actuators driven with 10 V ac signal superimposed on 10 V dc voltage.

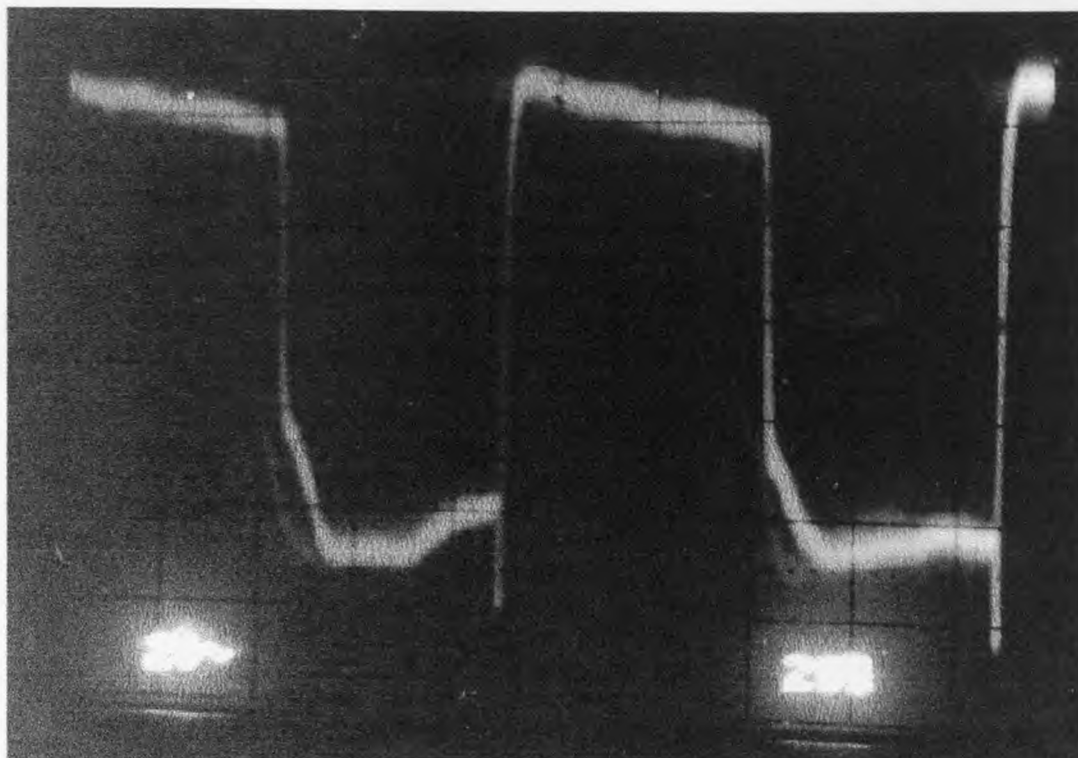

Figure 5.34 The photodiode response to the reflected laser beam at 10 Hz.

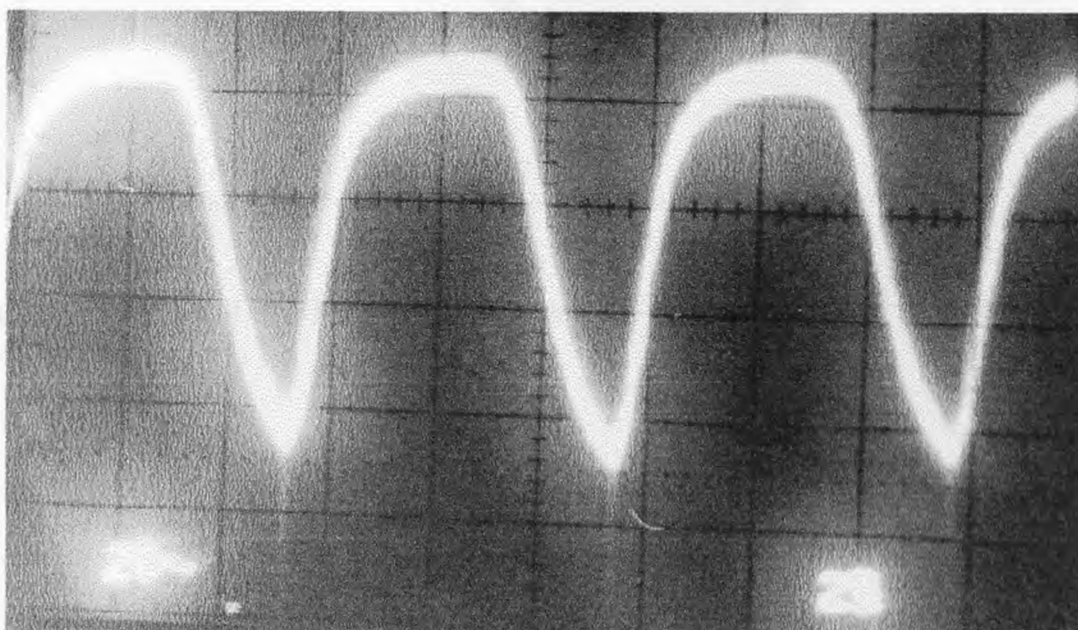

Figure 5.35 The photodiode response to the reflected laser beam at 166 Hz.

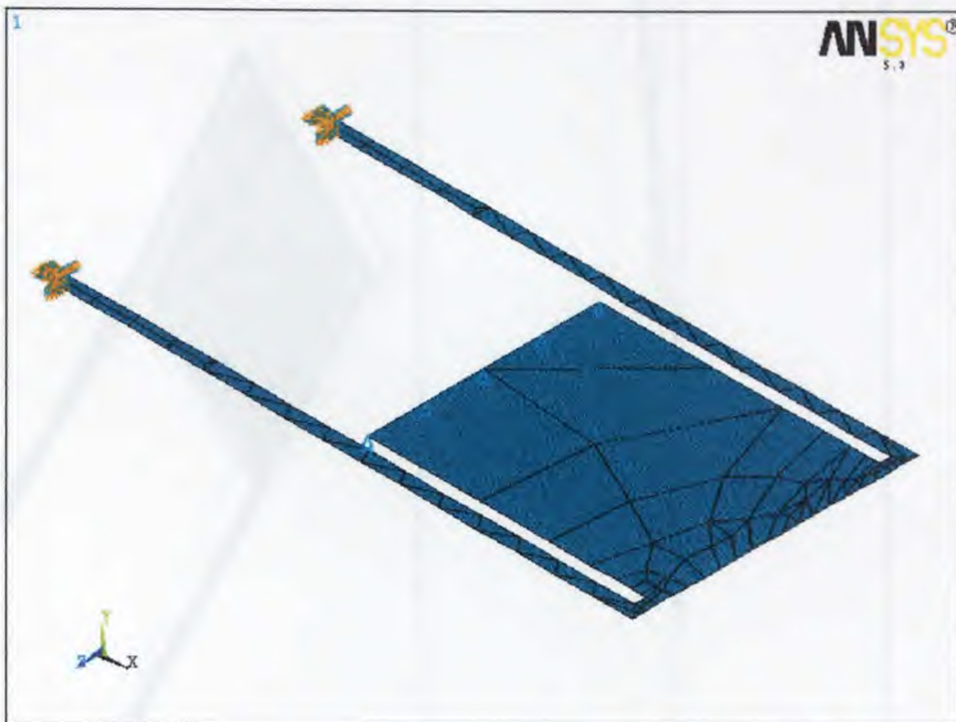

Figure 5.36 Solid model and mesh used to do modal FEA of the reshaped micromirror.

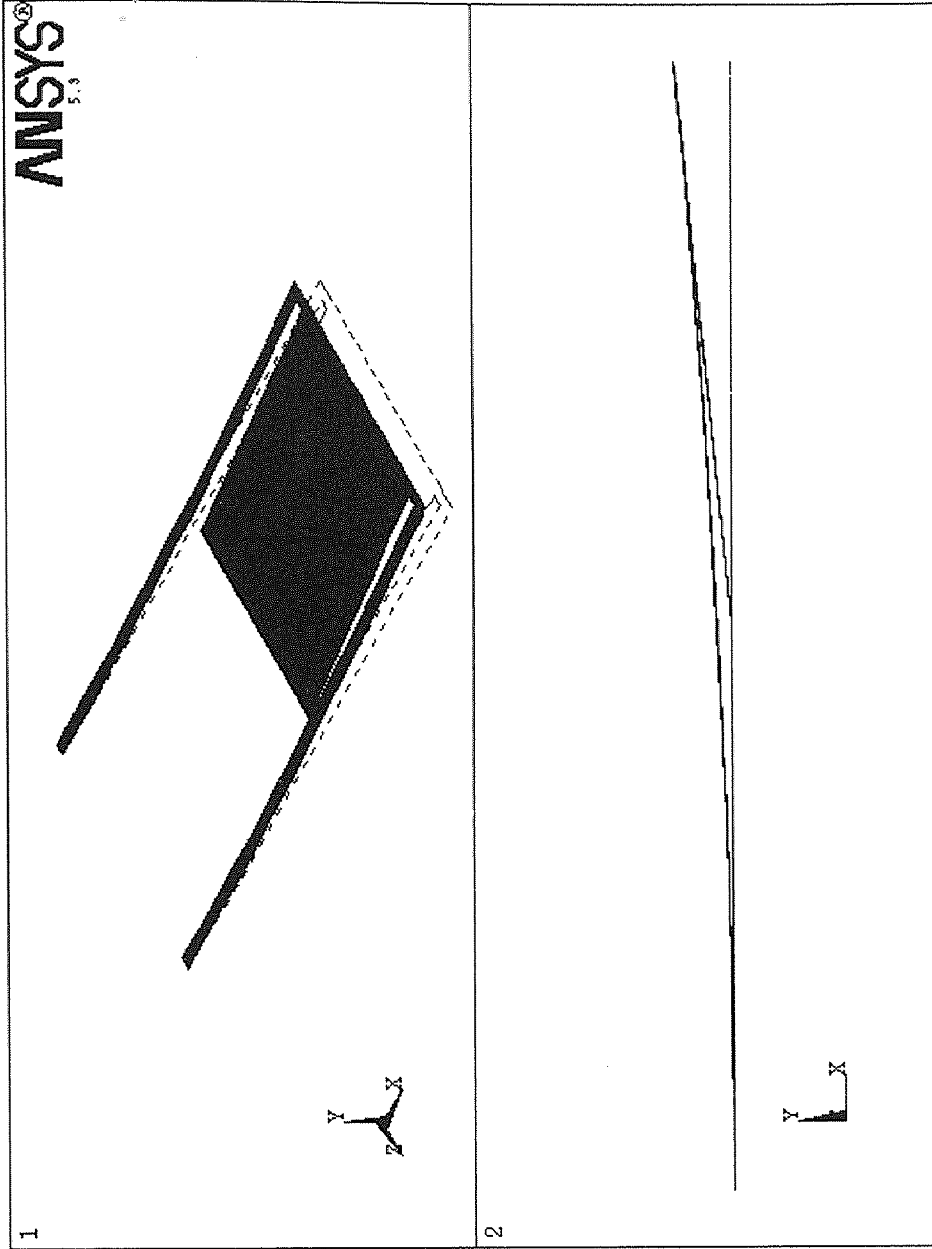

Figure 5.37 The deformed shape of the reshaped micromirror at the 1st mode.

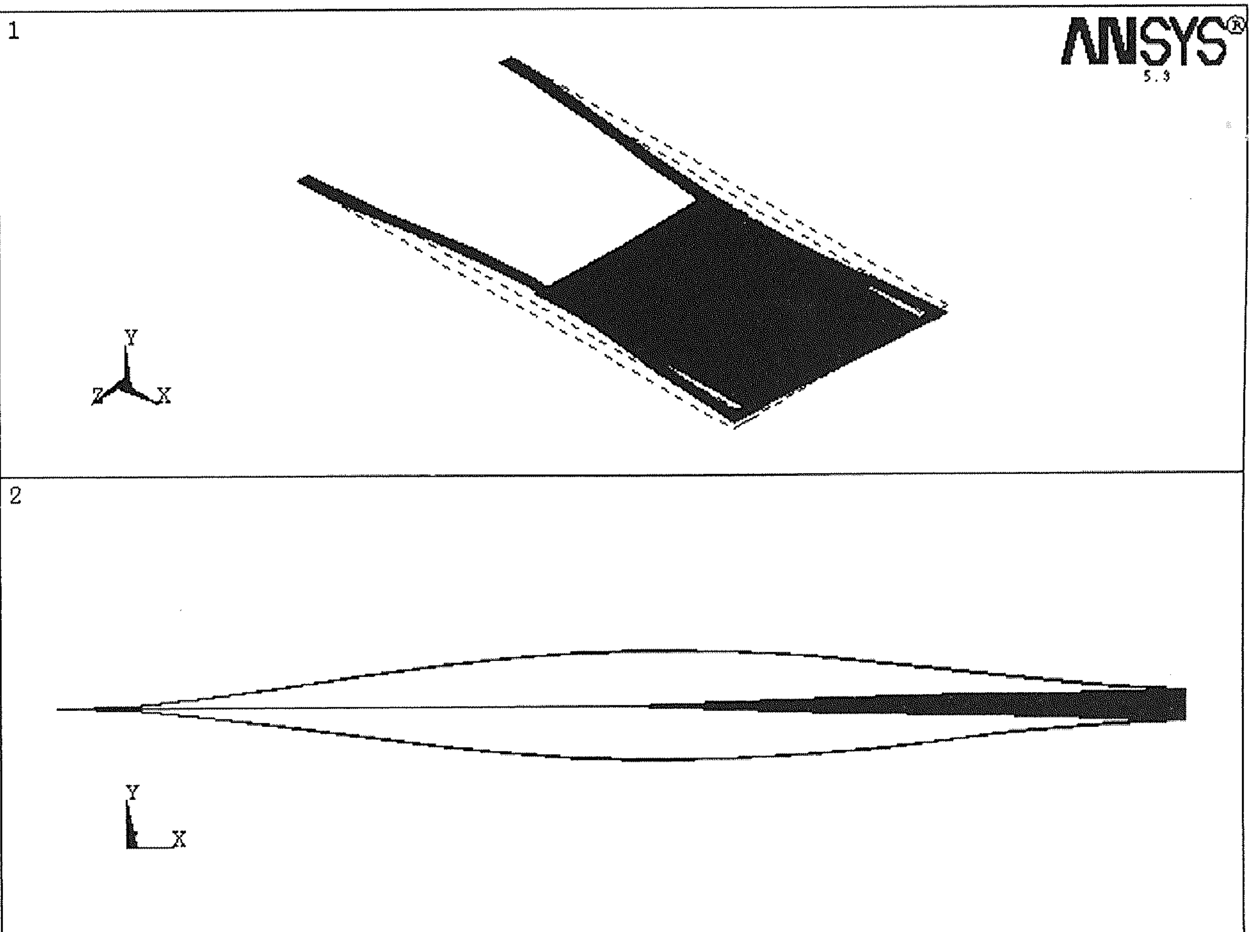

Figure 5.38 The deformed shape of the reshaped micromirror at the 2nd mode.

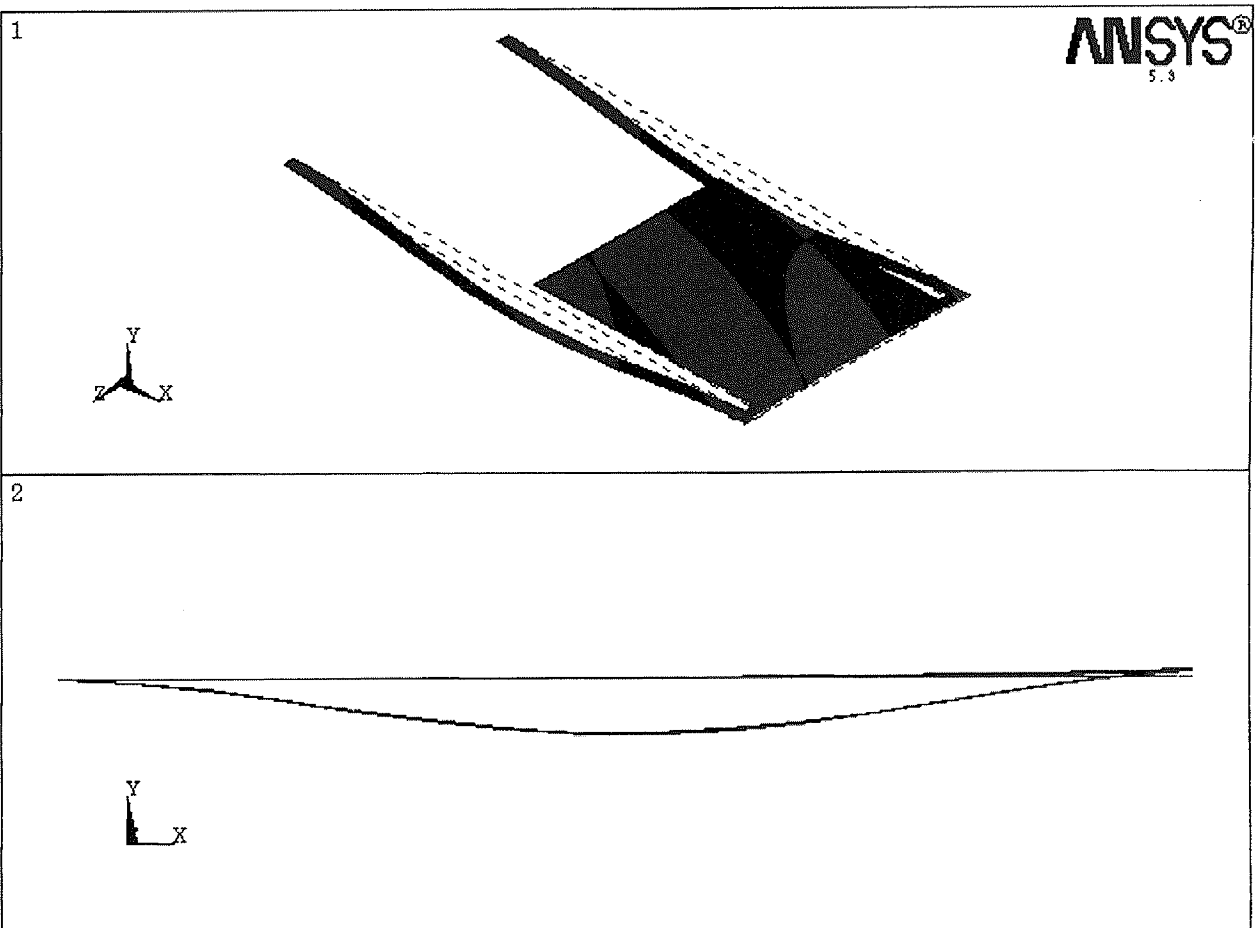

Figure 5.39 The deformed shape of the reshaped micromirror at the 3rd mode.

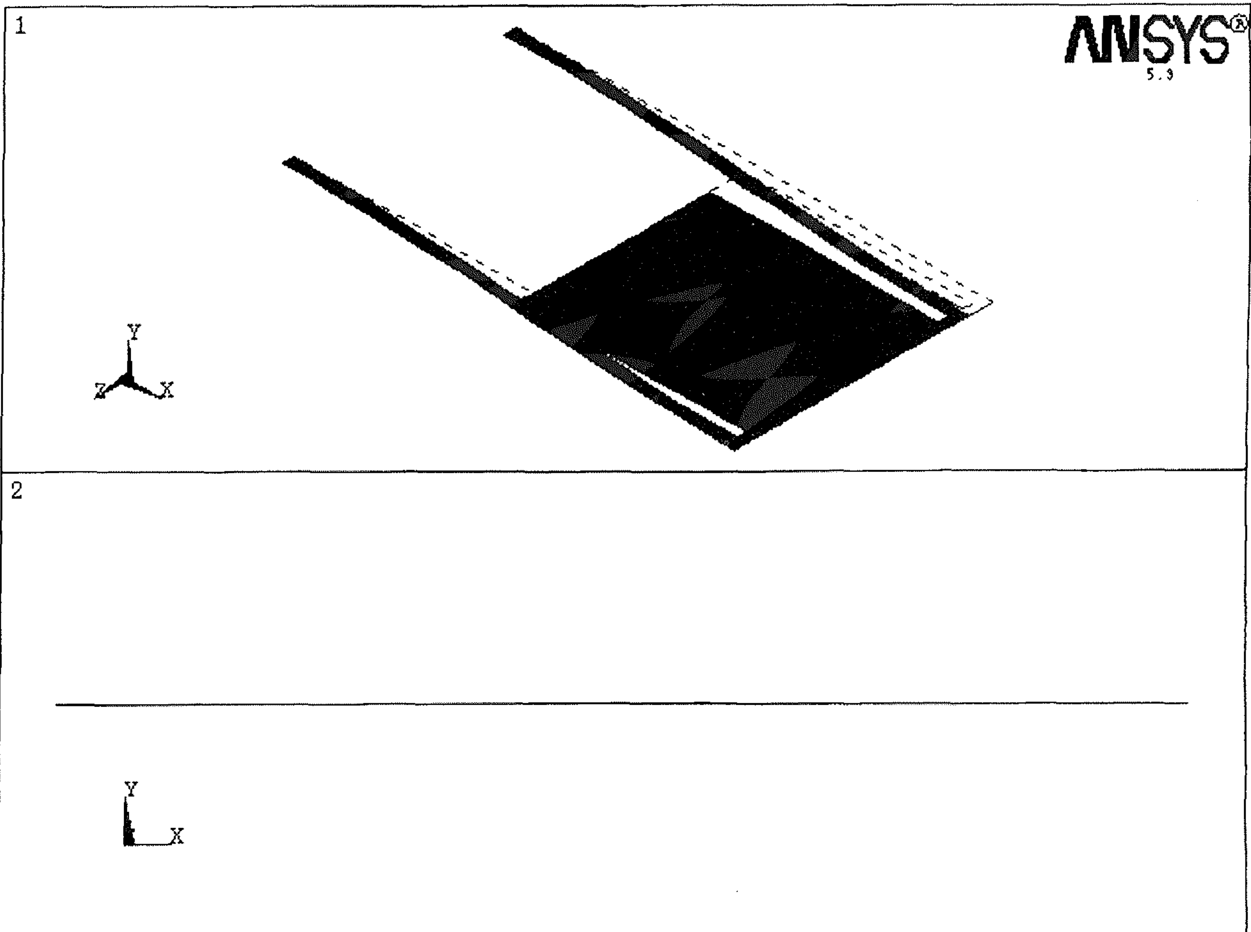

Figure 5.40 The deformed shape of the reshaped micromirror at the 4th mode.

The reliability of the reshaped micromirror was tested under fatigue test and shock test. The mirror was driven at the resonance frequency with thermal drive only (6.5V ac signal superimposed on 10V dc input voltage). The deflection was 6°, one half of the maximum deflection. The reshaped structure survived more than 1.5×10^9 cycles. The mirror was dropped on a metal surface from a hight of 30 cm, which corresponds to a shock of more than 200g, and the reshaped micromirror was found to be fully functional after this test.

The reshaped micromirror was also tested with electrostatic excitation, where a varying dc voltage was applied between the actuators and the substrate. The measured and simulated normalized tip position vs. the normalized electrostatic voltage was plotted in Figure 5.41. For 45° initial angle, the pull-in voltage was measured to be 300V. The maximum tip position was $350\mu m$. While the simulation results show, that the micromirror is pulled in when the tip reaches 85% of the maximum value, during the test of the micromirror much smaller values were measured. The reason is the friction between the lower edge of the mirror platform and the surface. In measured and simulated data, a hysteresis can be seen very clearly. The measured hysteresis is larger than the simulated results. In a few cases, the mirror platform got stuck to the substrate and didn't get released, even when the electrostatic input voltage was turned off completely, and both the substrate and the actuators were connected to ground. A gentle touch with the probe tip was enough to release the stuck micromirror. One solution to prevent sticking and friction problems is to open a window right under the mirror platform by etching through the wafer from back-side. This step requires a photolithography step which involves double-side alignment.

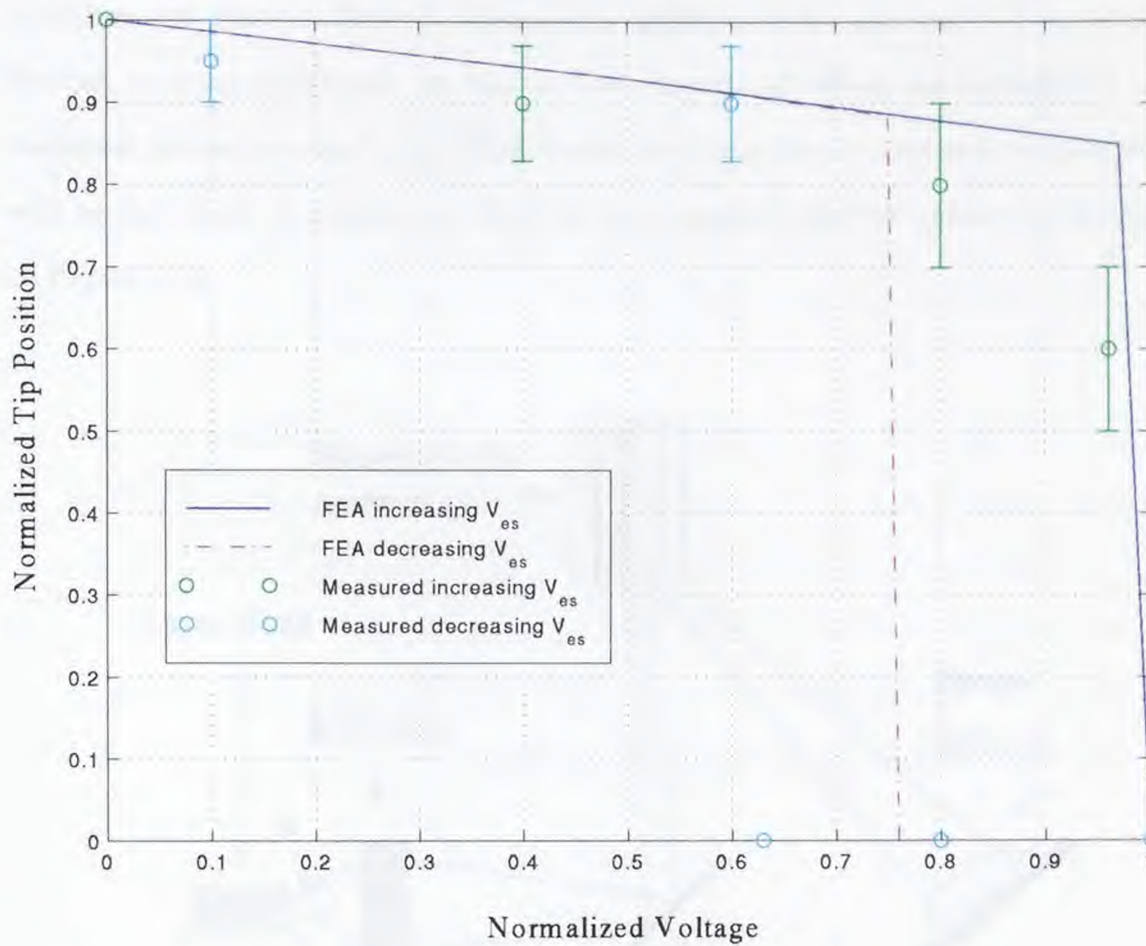

Figure 5.41 Normalized tip position (t/t_{max}) versus normalized voltage ($V/V_{pull-in}$). $V_{pull-in}$=350V, t_{max}=353μm.

5.5 A Proposed System Application: Microscanner for Barcode Readers

The micromirror, discussed in the previous sections, can be used as a part of an MOEM system, i.e. a microscanner for barcode readers. Resonant optical scanners have long been used for scientific and industrial applications that range from laser imaging and displays to laser surgery tools and home-office appliances such as fax machines and printers. Barcode scanners are widely used for automatic object identification in many industries. In this section, the use of silicon micromachined and reshaped micromirror and other MOEM devices to construct a resonant microscanner will be described. A conceptual sketch of an integrated barcode reader is displayed in Figure 5.42.

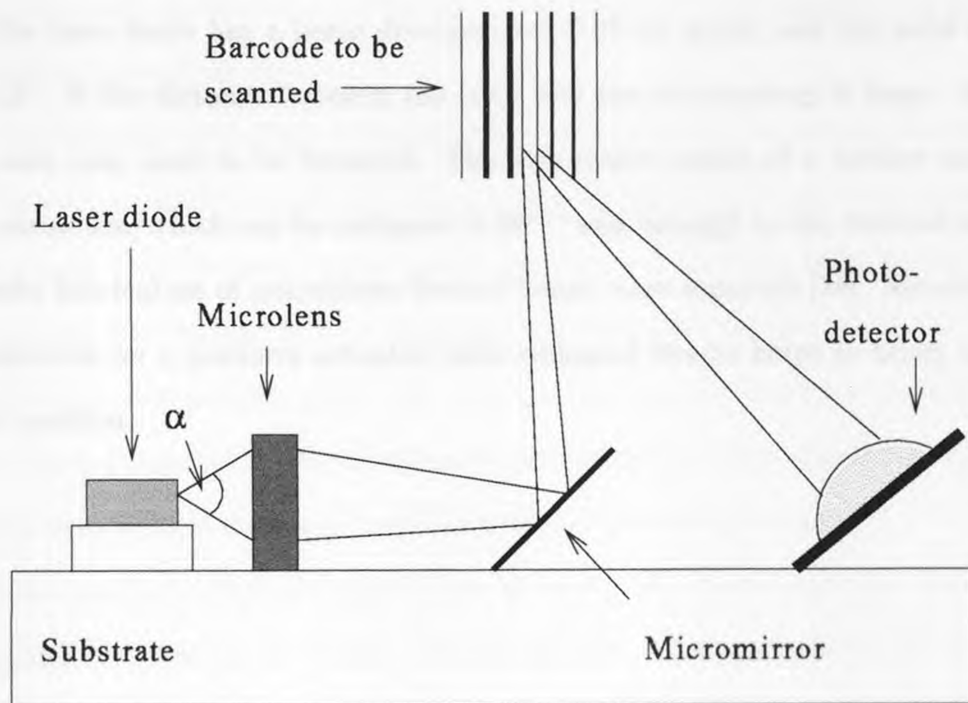

Figure 5.42 A prototype design for an integrated barcode-scanner module on a silicon substrate.

The proposed system does not require a sophisticated driving mechanism. As investigated in details above, one can drive a reshaped micromirror with simply applying thermal power. A novel resonant microscanner requires a fast scan rate, and a large scan angle, low mass and low operating power. The designed and fabricated micromirror with reshaped bimorph actuators can be set to any initial angle. It has a scan rate of 1 kHz with a Q-factor of 2.5. One can modify the length of the actuators and change the scan rate by changing the resonant frequency. The laser beam scan angle of the fabricated micromirror is 22°, which compares favorably with angles typically achieved in bulk resonant scanner. By optimizing the polysilicon-Si_3N_4 thickness ratio, this scan angle value can be improved further. The recent micromirror dissipates less than 100 mW, when thermal drive is combined with the electrostatic drive.

The laser diode has a beam divergence of 0.25-0.4 mrad, and the solid angle is α=10-12°. If the distance between the laser and the micromirror is large, then the laser beam may need to be focussed. The lens could consist of a surface micromachined structure, which can be reshaped to 90^{circ} and brought to the vertical position. Successful fabrication of polysilicon Fresnel lenses were reported [76]. Mounting the photodetector on a platform actuated with reshaped beams helps to bring it to the desired position.

CHAPTER 6
SUMMARY AND CONCLUSION

In this work, the design, simulation, fabrication and characterization of bimorph and monomorph cantilever beam actuators were investigated. These actuators are driven by electro-thermal power combined with electrostatic excitation, and they are able to produce large force and in and out-of-plane actuation.

A linear analytical model, which describes the thermal actuation of bimorph in-plane (inchworm) actuators, was proposed. The temperature dependent residual stress in both layers was included into the model. The numerical results obtained from the analytical model were compared to simulation results obtained with the FEA (Finite Element Analysis) and experimental measurements. The validity limits of the proposed model were discussed. The design of an improved two segment inchworm actuator was presented.

Out-of-plane actuation of monomorph and bimorph cantilever beams due to the thermal expansion coefficient mismatch and stress gradient was investigated. It was shown that the well known equations were not valid for large displacements. Thermal and electrostatic models for numerical methods were discussed. 2D actuator model for the electrostatic drive was solved using Newton-Raphson method. These results were compared to the results obtained from the nonlinear FEA and to the experimental tests of the fabricated $TaSi_2$-SiO_2 bimorph actuators.

The gradient stress throughout the thickness of a mono layer was shown to be responsible for bending of beams and membranes. A linear analytical model was proposed to account temperature dependent bending due to gradient stress.

Today's micromachining technology is limited merely by two dimensional IC process technologies. To overcome this limitation, a powerful technique, *reshaping* was introduced. With this technology, 3D structures, actuators, even more complex systems can be created out of the 2D IC world. Different setups for reshaping

process were proposed. As an example, three different types of surface micromachined polycrystalline structures were reshaped and 3D actuators were formed. It was found that elastic deformation inserted in the polycrystalline structure could be annealed with a current density of $3x10^4 A/cm^2$ in as low as 4 seconds. The effects of process time, input power and annealing current on the reshaping were investigated in details.

A micromirror, which made use of reshaped out-of-plane actuators were designed, fabricated and characterized. The micromirror, which can be driven with combined thermal and electrostatic excitation, was found to be a good candidate as a microscanner in a proposed barcode reader system with its wide laser beam scan angle of 22°, resonance frequency of 1 kHz, and the system quality factor Q of 2.5.

APPENDIX A

NEWTON-RAPHSON PROCEDURE

A.1 Mathematical Method

The purpose of this appendix is to present the Newton-Raphson method to solve general nonlinear equations. There are some other methods to solve nonlinear equations, but all of them have the same first step: The problem has to be brought into the standard form f(x)=0. Then to solve the problem, the zeros of the function are determined.

Newton-Raphson method uses the tangent line of f(x) at a point as the model for f(x). Although the search for the zeros of a function using this method has the potential of rapid convergence, there is also the possibility of overlooking zeros and not converging at all. The method starts with an assumption of the zero. At each step, the function is approximated with a straight line of the form

$$f_i = a_i x + b_i \tag{A.1}$$

having the same value and slope as f(x) at $x = x_i$, then the constants a_i and b_i satisfy

$$\begin{aligned} f_i(x_i) &= a_i x_i + b_i = f(x_i) \\ a_i &= f_i'(x_i) = f'(x_i) \\ b_i &= f(x_i) - f'(x_i)x_i \end{aligned} \tag{A.2}$$

where

$$f' = \frac{df}{dx} \tag{A.3}$$

The zero crossing using this straight-line approximation occurs at

$$a_i x + b_i = 0$$
$$x = -\frac{b_i}{a_i} = x_i - \frac{f(x_i}{f'(x_i)} \quad (A.4)$$

And this is a good choice for the next trial value of x, x_{i+1}. Then

$$x_{x+1} = x_i - \frac{f(x_i}{f'(x_i)} \quad (A.5)$$

The result in equation A.5 can be arrived at geometrically by examining Figure A.1, where at each step the slope of the function at the point of evaluation is used to give the next value of the variable to be used. [77]

This algorithm will converge to a zero of a function very rapidly, if it can. However, neither it is possible to guarantee the convergence, nor there is a guaranteed convergence test. Yet one must stop iterations according to a reliable convergence test. There are three basic reasons for stopping an iteration: [78]

The problem is solved or nearly so. Either f(x)=0 or the kth iterate has $f(x_k)$=0 very small.

The iteration has converged or nearly so. If the values x_k stop changing, there is no point in continuing the iteration. Specific tests one could use include:

$$x_{k+1} = x_k$$
$$|x_{k+1} - x_k| \leq Tolerance$$
$$|x_{k+1} - x_k| - |x_k - x_{k-1}| \leq Tolerance \quad (A.6)$$

where *Tolerance* is a parameter set by the user, and errors less than *Tolerance* are acceptable.

The iteration has gone on too long or the results are unreasonable. Every iteration should have a fixed limit unless one knows that it converges in all cases.

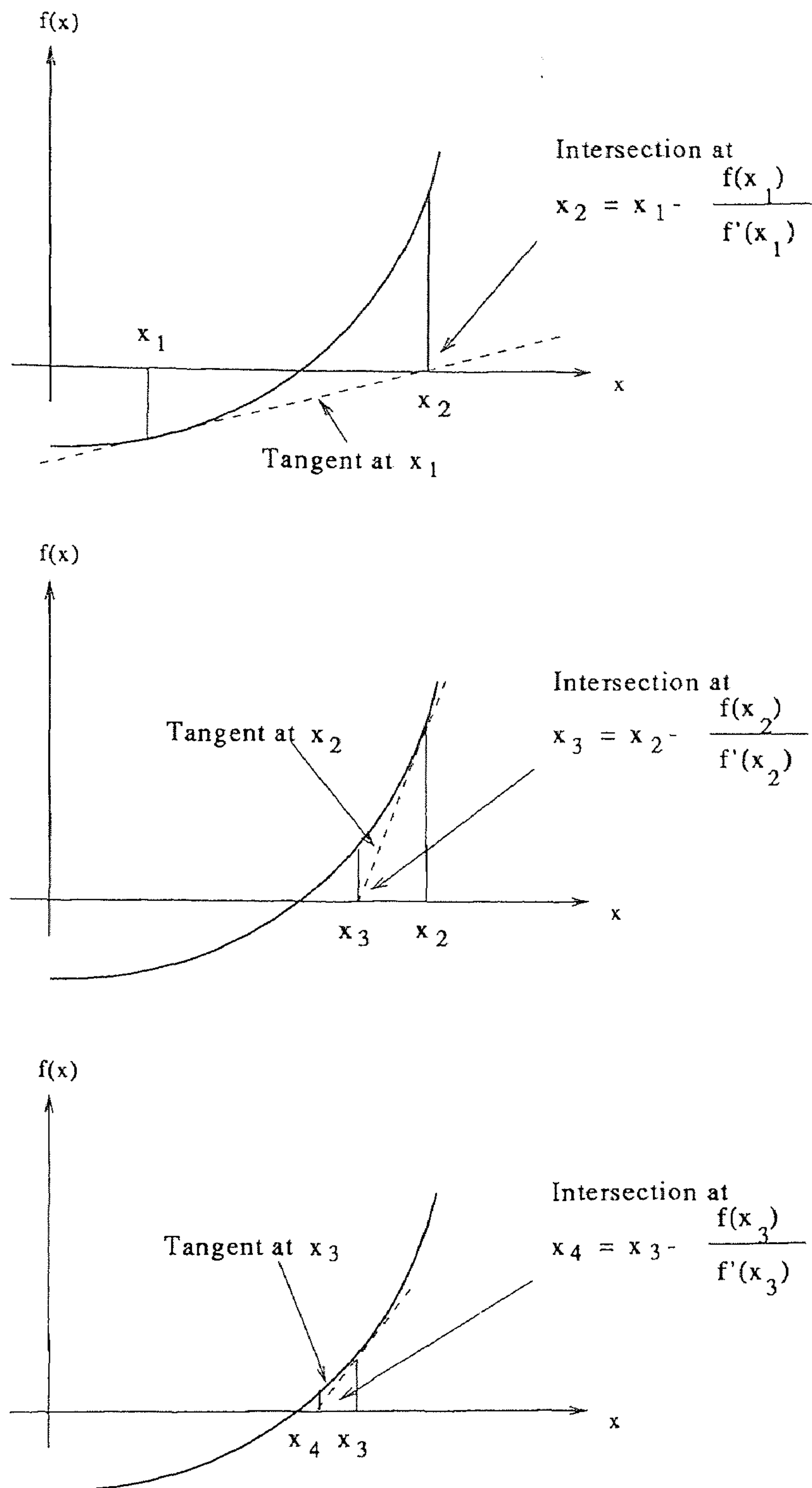

Figure A.1 Newton-Raphson method of iterative locating zeros.

There are usually bounds on the solution so that some values for $f(x_k)$ or x_k are unreasonable for that particular problem. This means that the iteration has gone astray. Tests that one could use include

$$\begin{aligned}|k| &\geq KLimit \\ |f(x_k)| &\geq FHuge \\ |x_k| &\geq XHuge \\ |a - x_k| + |x_k - b| &\geq |b - a| \quad (x_k \; not \; in \; [a,b])\end{aligned} \tag{A.7}$$

where *KLimit, FHuge,* and *XHuge* are specific values, which are not always easy to choose and depend on the problem at hand as well as the machine parameters.

A.2 Finite Element Analysis

The finite element discretization process yields a set of simultaneous equations:

$$[K]\{u\} = \{F^a\} \tag{A.8}$$

where $[K]$ is the coefficient matrix, $\{u\}$ is the vector of unknown DOF (degree of freedom) values, and $\{F^a\}$ is the vector of applied loads. If the coefficient matrix $[K]$ is itself a function of the unknown DOF values (or their derivatives) then equation equation A.8 is a nonlinear equation. The Newton-Raphson method is an iterative process of solving the nonlinear equations and can be written as:

$$[K_i^T]\{\Delta u_i\} = \{F^a\} - \{F_i^{nr}\} \tag{A.9}$$

$$\{u_{i+1}\} = \{u_i\} + \{\Delta u_i\} \tag{A.10}$$

where $[K_i^T]$ is the Jacobian matrix (tangent matrix), i is the subscript representing the current equilibrium iteration, and $\{F_i^{nr}\}$ is the vector of restoring loads corresponding to the element internal loads.

Both $[K_i^T]$ and $\{F_i^{nr}\}$ are evaluated based on the values given by $\{u_i\}$. The right hand side of equation equation A.9 is the residual or out-of-balance load vector;i.e., the amount the system is out of equilibrium. A single solution iteration is depicted graphically in Figure A.2 for a one DOF model. In a structural analysis, $[K_i^T]$ is the tangent stiffness matrix, $\{u_i\}$ is the displacement vector and $\{F_i^{nr}\}$ is the restoring force vector calculated from the element stresses.

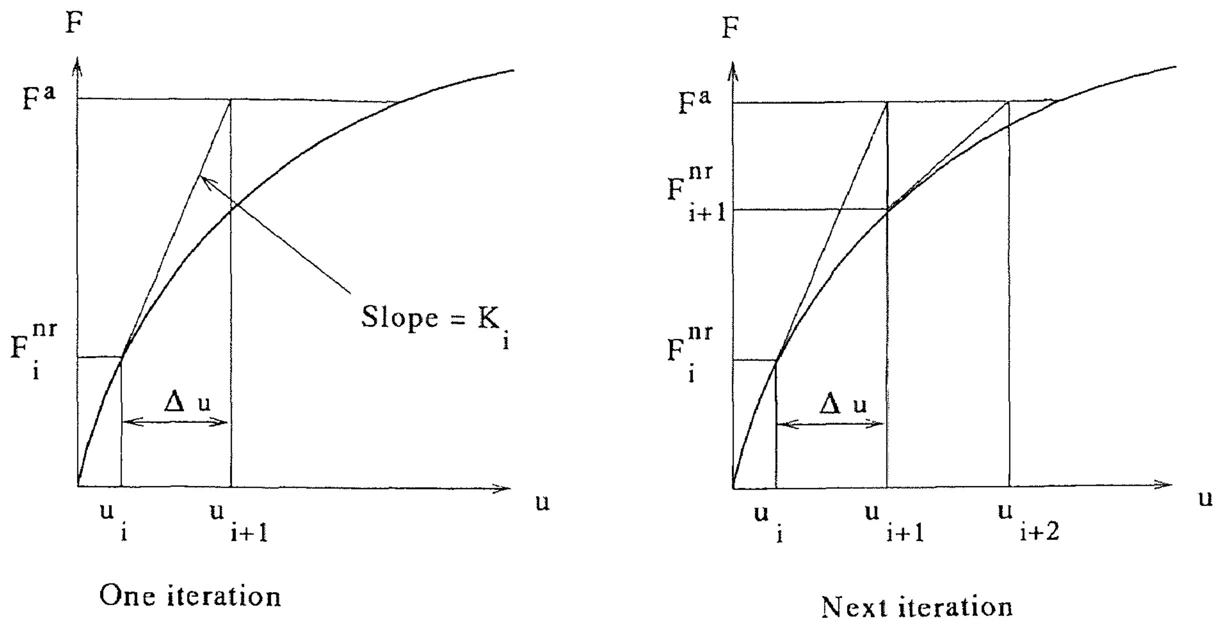

Figure A.2 FEA Newton-Raphson Solution.

As seen in Figure A.2, more than one Newton-Raphson iteration is needed to obtain a converged solution. The general algorithm proceeds as follows:

- Assume $\{u_o\}$. $\{u_o\}$ is usually the converged solution from the previous time step. On the first time step, $\{u_o\} = \{0\}$.
- Compute the updated tangent matrix $[K_i^T]$ and the restoring load $\{F_i^{nr}\}$ from configuration $\{u_i\}$.
- Calculate $\{\Delta u_i\}$ from equation equation A.9.

- Add $\{\Delta u_i\}$ to $\{u_i\}$ in order to obtain the next approximation $\{u_{i+1}\}$ (equation equation A.10).
- Repeat steps 2 to 4 until convergence is obtained.

Figure A.2 shows the solution of the ith and (i+1)th iterations. The subsequent iterations would proceed in a similar manner. The solution obtained at the end of the iteration process would correspond to load level $\{F^a\}$. The final converged solution would be in equilibrium, such that the restoring load vector $\{F_i^{nr}\}$ (computed from the current stress state) would equal the applied load vector $\{F^a\}$ (or at least to within some tolerance. None of the intermediate iteration solutions would be in equilibrium.

The Newton-Raphson procedure guarantees convergence if and only if the solution at any iteration $\{u_i\}$ is "near" the exact solution. Therefore, even without a path-dependent nonlinearity (such as plasticity), the incremental approach (i.e. applying the loads in increments) is sometimes required in order to obtain a solution corresponding to the final load level. [79]

APPENDIX B

PROCESS STEPS OF MICROSTRUCTURES DISCUSSED IN THIS THESIS

B.1 Inchworm Actuator

01- Wafer cleaning	
02- Wet oxidation	(3000 Å, 1 h, 1050°C)
03- Si_3N_4 LPCVD	(3000 Å, 50 min, 725°C)
04- LTO deposition	(2 μm, 20 h, 425°C)
05- Si_3N_4 LPCVD	(3000 Å, 50 min, 725°C)
06- Polysilicon LPCVD	(1 μm, 10 h, 600°)
07- Polysilicon doping	(Phosphorus, 2 h, 950°) $R_\square \leq 10\Omega/\square$
08- Photolithography	
09- Polysilicon RIE	
10- Si_3N_4 RIE	
11- Au sputtering	
12- Photolithography	
13- Au wet etch	
14- Sacrificial oxide etch	(49% HF, 8 min.)

B.2 Out-of-Plane Actuator

01- Wafer cleaning	
02- Wet oxidation	(3000 Å, 1 h, 1050°C)
03- Si_3N_4 LPCVD	(2000 Å, 50 min, 725°C)
04- Aluminum sputtering	(1 μm, 75°C)
05- LTO deposition	(0.9 μm, 10 h, 425°C)
06- $TaSi_2$ sputtering	(0.6 μm, 125°C)
07- Photolithography	
08- $TaSi_2$ RIE	
09- LTO RIE	
10- Sacrificial aluminum etch	

B.3 $TaSi_2$ Micromirror

01- Wafer cleaning	
02- Wet oxidation	(3000 Å, 1 h, 1050°C)
03- Si_3N_4 LPCVD	(2000 Å, 50 min, 725°C)
04- Aluminum sputtering	(1 μm, 75°C)
05- LTO deposition	(0.9 μm, 10 h, 425°C)
06- LTO Photolithography	(Bimorph Layer # 1 and micromirror platform)
07- LTO RIE	
08- $TaSi_2$ sputtering	(0.6 μm, 125°C)
09- Photolithography	(Bimorph Layer # 2)
10- $TaSi_2$ RIE	
11- Sacrificial aluminum etch	

B.4 Reshaped Actuator - A

01- Wafer cleaning	
02- Wet oxidation	(3000 Å, 1 h, 1050°C)
03- Si_3N_4 LPCVD	(3000 Å, 50 min, 725°C)
04- LTO deposition	(2 μm, 20 h, 425°C)
05- LTO anneal	(N_2, 1 h, 950°C)
06- Polysilicon LPCVD	(1.6 μm, 12 h, 600°)
07- Polysilicon doping	(Phosphorus, 2 h, 950°), $R_\square \leq 10\Omega/\square$
08- Photolithography	
09- Polysilicon RIE	
10- Sacrificial oxide etch	(49% HF, 8 min.)

B.5 Reshaped Actuator - B

01- Wafer cleaning	
02- Wet oxidation	(3000 Å, 1 h, 1050°C)
03- Si_3N_4 LPCVD	(3000 Å, 50 min, 725°C)
04- LTO deposition	(2 μm, 20 h, 425°C)
05- LTO anneal	(N_2, 1 h, 950°C)
06- Polysilicon LPCVD	(1.6 μm, 12 h, 600°)
07- Polysilicon doping	(Phosphorus, 2 h, 950°), $R_\square \leq 10\Omega/\square$
08- Polysilicon annealing	(N_2, 1 h, 1100°)
09- Photolithography	
10- Polysilicon RIE	
11- Sacrificial oxide etch	(49% HF, 8 min.)

B.6 Reshaped Actuator - C

01- Wafer cleaning	
02- Wet oxidation	(3000 Å, 1 h, 1050°C)
03- Si_3N_4 LPCVD	(3000 Å, 50 min, 725°C)
04- LTO deposition	(2 μm, 20 h, 425°C)
05- LTO anneal	(N_2, 1 h, 950°C)
06- Polysilicon LPCVD	(1.6 μm, 12 h, 600°C)
07- Polysilicon doping	(Phosphorus, 2 h, 950°C), $R_\square \leq 10\Omega/\square$
08- Photolithography	
09- Polysilicon RIE	
10- Si_3N_4 LPCVD	(2000 Å, 35 min, 725°C)
11- Photolithography	
12- Si_3N_4 RIE	
13- Sacrificial oxide etch	(49% HF, 8 min.)

APPENDIX C

MATLAB CODE FOR ELECTROMECHANICAL CALCULATIONS OF PULL-IN VOLTAGE FOR OUT-OF-PLANE ACTUATOR USING NEWTON-RAPHSON METHOD

```
% Save this file as cbeam.m .

cs=input('New case ? (1=yes or 0=no): '); if cs==1

clear;

d = input('Enter discretization number (50 to 100 range is suggested): ');

N = d+4;

Z = input('Enter newton iteration number (5 to 10 range is suggested): ');

L = 1e-6*input('Enter length in um: ');

w = 1e-6*input('Enter width in um: ');

t = 1e-6*input('Enter thickness in um: ');

g = 1e-6*input('Enter gap in um: ');

E = 1e9*input('Enter youngs modulus in GPa: ');

step = 1e-6*input('Enter step height in um: ');

dsdy = 1e12*input('Enter transverse stress gradient (MPa/um): ');

end

tip = d+2;

e = 8.8541878e-12;

h = L/(d-1);

if dsdy =0

Radius = E/dsdy;

mxphi = g/L + L/(2*Radius);

else

mxphi = g/L;

end
```

```
w1 = w;
I = t^3/36 * (w^2+4*w*w1+w1^2)/(w+w1);
k = 2*E*t^3/(3*L^4);
V-pull-in-estimate = (8*k*g^3/(27*e))^0.5
g1 = 0.28;
c1 = 0.42;
V-pull-in-HH = real((g1*E*t^3*g^3/(e*L^4*(1+c1*g/w)))^0.5)
y = g*ones(N,1);
y-old = y;
phi-old = 0;
r = zeros(N,1);
A = zeros(N,N);
C = zeros(N,1);
y4p = zeros(N,1);
con = zeros(N,1);
if dsdy  = 0
for i = 1:N
con(i) = Radius - sign(Radius)*(Radius^2-((i-3)*h)^2)^0.5;
end
else
con = zeros(N,1);
end
A(1,3) = 1;
A(2,2) = -1;
A(2,4) = 1;
A(N-1,N-3) = 1;
A(N-1,N-2) = -2;
```

```
A(N-1,N-1) = 1;
A(N,N-4) = -1;
A(N,N-3) = 2;
A(N,N-1) = -2;
A(N,N) = 1;
mode=input('Normal Mode or Pull-In Mode ? (1=Normal or 0=Pull-In): ');
if mode == 1
% BEGIN MODE 1 = NORMAL
V = input('Enter voltage: ');
b = -e*V^2*w/(2*E*I);
c = 0.65*b/w;
phi = 0;
count = 0;
r(tip) = 1;
while abs(r(tip)/y(tip)) > 1e-5
for i=3:N-2
y4p(i) = (y(i-2)-4*y(i-1)+6*y(i)-4*y(i+1)+y(i+2))/h^4;
A(i,i-2) = 1;
A(i,i-1) = -4;
A(i,i) = 6+2*h^4/(y(i)+con(i))*(y4p(i)-c/(2*(y(i)+con(i))));
A(i,i+1) = -4;
A(i,i+2) = 1;
C(i) = h^4*(b/(y(i)+con(i))^2-y4p(i)+c/(y(i)+con(i)));
end
r=A\ C;
if count > Z
y=y+(r/(count)^0.5);
```

```
else
y=y+r;
end
y(N-2);
count = count + 1;
if step  = 0
Mo = (y(4)-2*y(3)+y(2))/(h^2)*E*I;
phi = -Mo*(step)/(E*I);
y1p3 = -(y(4) - y(2))/(2*h);
C(2) = -2*h*(phi - y1p3);
end
end
% END OF NEWTON ITERATIONS FOR MODE 1
y=(y+con);
cap = 0;
for i=4:N-2
f = w/y(i);
cap = cap+(e*w*h/y(i))*4*((4/(pi*f))^(3/20)+pi/4*f+(1+
        4/(pi*f))^(-1/2)*atanh((1+4/(pi*f))^(-1/2)))/(pi*f);
end
Capacitance = cap
plot(1e6*y);
axis([0 105 0 10]);
xlabel('Discretization in x');
ylabel('Gap (um)');
Tip-gap = y(tip)
Error = r(tip)/y(tip)
```

```
% END OF MODE 1 = NORMAL
else
% BEGIN MODE 2 = PULLIN
VMIN = 0;
VMAX = 500*V-pull-in-HH;
V = 0.01*VMAX;
phi = 0;
% BEGIN BINARY SEARCH FOR PULLIN VOLTAGE
while abs(VMAX-VMIN) > 0.001
b = -e*V^2*w/(2*E*I);
c = 0.65*b/w;
% BEGIN NEWTON ITERATIONS FOR VOLTAGE = V
r(tip) = 0.5;
err = 1;
count = 1;
lim = 2*floor((log(VMAX/(VMAX-VMIN)))) + Z;
while (((abs(r(tip)) < err & count <= lim)—(count < Z))&(phi>=0)&(phi<=mxphi))
if (count < 5)
err = abs(r(tip));
end
for i=3:N-2
y4p(i) = (y(i-2)-4*y(i-1)+6*y(i)-4*y(i+1)+y(i+2))/h^4;
A(i,i-2) = 1;
A(i,i-1) = -4;
A(i,i) = 6+2*h^4/(y(i)+con(i))*(y4p(i)-c/(2*(y(i)+con(i))));
A(i,i+1) = -4;
A(i,i+2) = 1;
```

```
C(i) = h^4*(b/(y(i)+con(i))^2-y4p(i)+c/(y(i)+con(i)));
end
r=A\ C;
if count > 10
y=y+(r/(count)^0.5);
else
y=y+r;
end
count = count + 1;
if step  = 0
Mo = (y(4)-2*y(3)+y(2))/(h^2)*E*I;
phi = -Mo*(step)/(E*I);
y1p3 = -(y(4) - y(2))/(2*h);
C(2) = -2*h*(phi - y1p3);
end
end
% END NEWTON ITERATIONS FOR VOLTAGE = V
V-pull-in = V
Tip-gap = y(tip)+con(tip)
if step  = 0
rotation = phi
end
Error = r(tip)/y(tip)
iterations = count-1
if ((abs(Error)>1e-4)—(y(tip)<-con(tip))—(y(tip)>g)—(phi<0)—(phi>mxphi))
VMAX = V;
V = (VMIN+V)/2;
```

```
y = y-old;
phi = phi-old;
C(2) = 0;
else
VMIN = V;
V = (VMAX+V)/2;
y-old = y;
phi-old = phi;
end
end
% END BINARY SEARCH FOR PULLIN VOLTAGE
cap = 0;
for i=4:N-2
f = w/y(i);
cap = cap+(e*w*h/y(i))*4*((4/(pi*f))^(3/20)+pi/4*f+(1+4/(pi*f))^(-1/2)*
            atanh((1+4/(pi*f))^(-1/2)))/(pi*f);
end
Capacitance = cap
plot(y*1e6);
axis auto
xlabel('Discretization in x');
ylabel('Gap (um)');
end
cs2=input('Again? (yes=1 or no=0:)');
if cs2==1; run cbeam; end
```

APPENDIX D
NUMERICAL MODELING AND SIMULATION OF MEMS

Today, the microsensors and actuators are getting more and more complicated, and it is very well known, that it is very difficult (and most of the time impossible) to obtain an analytical equation, even if the model and boundary conditions are simplified drastically.

Due to the very high prototyping costs, simulation plays an important role in microsystem domain as much as it does in microelectronics domain. The modeling and simulation of microsystems follows a logical development flow:

- **layout and design** : Mask editors and design rule checkers (DRCs).
- **process simulation** : Semiconductor process simulation and etch simulation.
- **device simulation** : Field solvers (FEM, BEM), equivalent circuits, HDL.
- **system simulation** : Equivalent circuit, HDLs , analog simulators.
- **verification and measurement** : Validation of simulation.
- **global simulation** : Iterative execution of the above steps (optimization).

CAD systems for MEMS require the 3D and coupled physics modeling and the planar mask layout and circuit simulation of integrated circuits. Seamless data transfer between the levels is required to accelerate development time and extend the usefulness of simulation. Challenges include geometric construction from mask and process data, 3D coupled field simulation, construction of lumped macro models, and computer aided insertion of those macro models into dynamical simulators [80]. The study of the dynamic behavior of a microsystem is complex as most transducers are nonlinear, involving at least two energy domains and often executing large motions which introduce geometric nonlinearities into the problem. The system-level is increasingly becoming important in the design of market-driven MEMS [81].

D.1 Finite Element Method and CAD Tools

Finite element method is not new. It has been used throughout centuries for evaluating certain quantities (particularly area and volume) by adding or counting well-defined geometric figures (elements). Today's understanding of the finite element method, however, is finding an approximate solution to a boundary and initial value problem by assuming that the domain is divided into well defined subdomains (elements), and that the unknown function of the *state variable* is defined approximately within each element. With these individually defined functions matching each other at the element nodes or at certain points at the interfaces, the unknown function is approximated over the entire domain. [82]

Since the entire domain is divided into numerous elements and the function is approximated in terms of its values at certain points (nodes), it is inevitable that the evaluation of such a function will require solution of simultaneous equations. Because of this, the finite element methods were not widely used until the middle of this century, at which time the computer became a powerful computational tool.

The most important requirement for a MEMS designer is that the CAD system be able to analyze realistic 3D structures, whose geometry is either provided directly by the designer, or is derived from simulation of the fabrication process using a process flow and mask description. Most of the time, a combined analysis (e.g. thermo-structural, electrostatic-thermal-structural) is needed to simulate the performance of the sensor or actuator. To be able to include the very important dependence of material properties on process conditions is another very important requirement.

Despite of many improvements over the last 2 decades, the available finite element packages (e.g. ANSYS, IDEAS), which were designed to solve general mechanical or civil engineering problems, haven't been appropriate to handle MEMS' problems. In 80's, the need for a new kind of CAD system for microelectromechanical

devices and systems was identified [83], and the development of dedicated MEMS device analysis programs began. One of them is MEMCAD, which was the result of the systematic approach to create a CAD tool for MEMS design in MIT [58]. Since 1993, MEMS design and simulation tools have been available, and tremendous improvements have been done.

D.2 Modeling Internal Stress

Internal stress needs to be introduced at the next step. Internal stress exists in almost all thin films used in MEMS process, so applying internal stress as a boundary condition must be as easy as applying other boundary conditions. Unfortunately, this is not the case with the conventional FEA software packages. Two of the most popular and commercially available CAD tools, IntelliCAD and MEMCAD, have recently had the internal stress as a load in their latest releases. However, both of them failed to converge to a solution for the highly nonlinear inchworm problem. The author believes, that this is because of the FE solver, ABAQUS/Standard. In most of the Finite Element Modeling oriented CAD tools, mechanical analysis is performed using ABAQUS/Standard, which is a general purpose finite element analysis program with special emphasis on linear and nonlinear structural engineering and heat transfer applications. In the latest release, ABAQUS includes a package ABAQUS/Explicit, which is a transient dynamics program designed specifically to serve advanced nonlinear structural analysis needs. The program includes element formulations for beams, shells, and continuum elements[1]. The use of ABAQUS/Explicit may have the above mentioned CAD tools be able to solve the inchworm problem with internal stresses applied as a load.

[1]More information about ABAQUS can be obtained from http://www.hks.com

REFERENCES

1. K. J. Gabriel, "Engineering microscopic machines," *Scientific American*, pp. 118–121, 1995.

2. W. Menz, W. Bacher, M. Hermening, and A. Michel, "The LIGA technique - a novel concept for microstructures and the combination with Si-technologies by injection molding," in *Proc. IEEE MEMS Workshop*, pp. 69–73, 1991.

3. H. Guckel, K. J. Skrobis, T. R. Christenson, J. Klein, S. Han, B. Choi, and E. G. Lowell, "Fabrication of assembled micromechanical components via deep x-ray lithography," in *Proc. IEEE MEMS Workshop*, pp. 74–79, 1991.

4. X. Sun, T. Masuzawa, and M. Fujino, "Micro ultrasonic machining and self-aligned multilayer machining/assembly technologies for 3D micromachines," in *Proc. IEEE MEMS Workshop*, pp. 312–316, 1996.

5. A. Pisano, "Resonant-structure micromotors," in *Proc. 2nd IEEE MEMS Workshop*, pp. 44–48, 1989.

6. H. Guckel, J. Klein, T. Christenson, and K. Skrobis, "Thermo-magnetic metal flexure actuators," in *Proc. IEEE MEMS Workshop*, pp. 73–75, 1992.

7. B. Wagner, M. Kreutzer, and W. Benecke, "Electromagnetic microactuators with multiple degrees of freedom," in *Proc. Transducers '91*, pp. 614–617, 1991.

8. S. F. Bart and J. H. Lang, "An analysis of electroquasistatic induction motors," *Sensors and Actuators*, vol. 20, pp. 97–106, 1989.

9. M. Mehregany, P. Nagarkar, S. D. Santuria, and J. H. Lang, "Operation of microfabricated harmonic and ordinary side-drive motors," in *Proc. IEEE MEMS Workshop*, pp. 1–8, 1990.

10. M. Sakata, Y. Hatazawa, A. Omodaka, T. Kudoh, and H. Fujits, "An electrostatic top motor and its characteristics," *Sensors and Actuators*, vol. A21-A23, pp. 168–172, 1990.

11. W. C. Tang, T. Nguyen, and R. T. Howe, "Laterally driven polysilicon resonant microstructures," *Sensors and Actuators*, vol. 20, pp. 25–32, 1989.

12. R. Mahadevan, M. Mehregany, and K. J. Gabriel, "Application of electric microactuators to micromechanics," *Sensors and Actuators*, vol. A21-A23, pp. 219–225, 1990.

13. S. Akamine, T. R. Albrecht, M. J. Zdeblick, and C. F. Quate, "A planar process for microfabrication of integrated scanning tunneling microscops," *Sensors and Actuators*, vol. A21-A23, pp. 964–970, 1990.

14. H. Toshiyoshi, T. Ueda, and H. Fujita, "A piezoelectrically operated optical chopper by quartz micromachining," *IEEE J. Microelectromech. Systems*, vol. 5, pp. 3–9, 1995.

15. A. Walker and K. J. Gabriel, "Thin-film processing of TiNi shape memory alloy," *Sensors and Actuators*, vol. A21-A23, pp. 243–246, 1990.

16. C. G. Keller and R. T. Howe, "Nickel-filled hexsil thermally actuated tweezers," in *Proc. Solid State Sensors and Actuators and Eurosensors IX*, Stockholm, Sweden, pp. 376–379, 1995.

17. W. Benecke and W. Riethmuller, "Applications of silicon-microactuators based on bimorph structures," in *Proc. IEEE MEMS Workshop*, pp. 116–120, 1989.

18. M. J. Zdeblick, R. Anderson, B. Kline-Schoder, R. Miles, and W. Weber, "Thermopneumatically actuated microvalves and integrated electro-fluidic circuits," in *Proc. Solid State Sensor and Actuator Workshop*, pp. 251–255, 1994.

19. J. A. Folta, N. F. Raley, and E. W. Hee, "Design, fabrication and testing of a miniature peristaltic membrane pump," in *Proc. Solid-State Sensor and Actuator Workshop*, pp. 186–189, 1992.

20. G. K. Fedder, J. C. Chang, and R. T. Howe, "Thermal assembly of polysilicon microactuators with narrow-gap electrostatic comb-drive," in *Proc. Solid-State Sensor and Actuator Workshop*, pp. 63–68, 1992.

21. A. D. Johnson and E. J. Shahoian, "Recent progress in thin film shape memory microactuators," in *Proc. IEEE MEMS Workshop*, pp. 216–220, 1995.

22. S. M. Bobbio, M. D. Kellam, B. W. Dudly, S. Goodwin-Johnasson, S. K. Jones, J. D. Jacobson, F. M. Tranjan, and T. D. DuBois, "Integrated force arrays," in *Proc. IEEE MEMS Workshop*, pp. 149–154, 1993.

23. M. Minami, S. Kawamura, and M. Esashi, "Distributed electrostatic micro actuator (DEMA)," in *Proc. Transducers '93*, pp. 2–3, 1993.

24. M. Ataka, A. Omodaka, N. Takeshima, and H. Hujita, "Polyimide bimorph actuators for a ciliary motion system," *IEEE J. of Microelectromach. Systems*, vol. 2, pp. 146–150, 1993.

25. S. Konishi and H. Fujita, "A conveyance system system using air flow based on the concept of distributed micromotion systems," *IEEE J. Microelectromech. Systems*, vol. 4, pp. 54–58, 1994.

26. K. Petersen, "Micromechanical light modulator array fabricated on silicon," *Applied Physics Letters*, vol. 31, p. 521, 1977.

27. M. Kiang, O. Solgaard, R. S. Muller, and K. Y. Lau, "Micromachined polysilicon microscanner for barcode readers," *IEEE Photonics Technology Letters*, vol. 8, pp. 1707–1709, 1996.

28. W. D. Cowan and V. M. Bright, "Vertical thermal actuators for micro-opto-electro-mechanical systems," *Proc. SPIE*, vol. 3226, pp. 137–146, 1997.

29. J. Younse, "Mirrors on a chip," *IEEE Spectrum*, pp. 27–31, Nov. 1993.

30. M. Kiang, O. Solgaard, R. S. Muller, and K. Y. Lau, "Silicon micromachined micromirrors with integrated high-precision actuators for external-cavity semiconductor lasers," *IEEE Photonics Technology Letters*, vol. 8, pp. 95–97, 1996.

31. S. M. Sze, *Semiconductor Sensors*, pp. 131–2, John Wiley and Sons Inc., New York, NY, 1994.

32. M. Ohring, *The Materials Science of Thin Films*, pp. 403–451, Academic Press, San Diego, CA, 1992.

33. J. N. Cernica, *Strength of Materials*, pp. 133–141, Holt, Rinehart and Winston, Inc., New York, NY, 1966.

34. T. A. Kneckt, "Bonding techniques for solid-state pressure sensors," in *Proc. Transducers '91*, p. 95, 1991.

35. V. L. Spiering, S. Bouwstra, R. M. F. J. Spiering, and M. Elwenspoek, "On-chip decoupling zone for package-stress reduction," in *Proc. Transducers '91*, p. 982, 1991.

36. H. L. Offereins, H. Sandmeier, B. Folkmer, U. Steger, and W.Lang, "Stress free assembly technique for a silicon based pressure sensor," in *Proc. Transducers '91*, p. 986, 1991.

37. G. G. Stoney, "Stress and strain in materials," in *Proc. Roy. Soc.*, vol. A82, p. 172, 1909.

38. W. Buckel, "Internal stresses," in *J. Vac. Sci. Tech.*, vol. 6, p. 606, 1969.

39. P. Krulevitch, G. C. Johnson, and R. T. Howe, "Stress and microstructure in LPCVD polycrystalline silicon films: Experimental results and closed form modeling of stresses," in *Material Res. Soc. Symp. Proc.*, vol. 239, pp. 13–18, 1992.

40. M. Tamura and H. Sunami, "Generation of dislocations by chemical vapor deposited Si_3N_4 films on silicon," in *Japanese J. Appl. Phys.*, vol. 11, p. 1097, 1972.

41. A. G. Noscov, E. B. Gorokhov, G. A. Sokolova, E. M. Trukhanov, and S. I. Stenin, "Correlation between stress and structure in CVD silicon nitride films," in *Thin Solid Films*, vol. 162, p. 129, 1988.

42. M. Sekimoto, H. Yoshihara, and T. Ohkuba, "Silicon nitride single-layer x-ray mask," in *J. Vac. Sci. Technol.*, vol. 21, p. 1017, 1982.

43. S. P. Murarka and T. F. Retajczyk, "Effect of phosphorus doping on stress in silicon and polycrystalline silicon," *J. Appl. Phys.*, vol. 54, pp. 2069–2072, 1983.

44. D. Maier-Schneider, A. Koprululu, S. Ballhausen, and E. Obermeier, "Elastic properties and microstructure of LPCVD polysilicon films," *J. Micromech. Microeng.*, vol. 6, pp. 436–446, 1996.

45. M. Kawata and T. Katoda, "Characterization of stress generated in polycrystalline silicon during thermal oxidation by laser Raman spectroscopy," *J. of Applied Physics*, vol. 75, pp. 7456–7459, 1994.

46. M. Furtsch, M. Offenberg, H. Muenzel, and J. R. Morante, "Comprehensive study of processing parameters influencing the stress and strain gradient of thick polysilicon layers," in *Proc. SPIE*, vol. 3223, pp. 130–141, 1997.

47. T. Suzuki, A. Mimura, and T. Ogawa, "The deformation of polycrystalline-silicon deposited on oxide-covered single crystal silicon substrates," *J. of Electrochemical Soc.*, vol. 57, pp. 1776–1780, 1977.

48. H. Guckel, T. Randazzo, and D. W. Burns, "A simple technique for the determination of mechanical strain in thin films with applications to polysilicon," *J. of Applied Physics*, vol. 57, pp. 1671–1675, 1985.

49. R. Mutikainen and M. Orpana, "Silicon surface micromachined structures for the stress measurement of thin films," *Material Research Soc. Symp. Proc.*, vol. 308, pp. 153–158, 1993.

50. K. Najafi and K. Suzuki, "A novel technique and structure for the measurement of intrinsic stress and young's modulus of thin films," in *Proc. IEEE MEMS Workshop*, pp. 96–7, 1989.

51. H. C. Nathanson, W. E. Newell, R. A. Wickstrom, and J. R. Davis, "The resonant gate transistor," *IEEE Transactions on Electron Devices*, vol. ED-14, pp. 117–133, 1967.

52. R. Legtenberg, E. Berenschot, M. Elwenspoek, and J. Fluitman, "Electrostatic curved electrode actuators," in *Proc. IEEE MEMS Workshop*, pp. 37–42, 1995.

53. E. J. Garcia and J. J. Sniegowski, "Surface micromachined microengine," *Sensors and Actuators*, vol. A 48, pp. 203–214, 1995.

54. E. J. Garcia and J. J. Sniegowski, "The design and modeling of a comb-drive-based microengine for mechanism drive application," in *Proc. Transducers '93*, pp. 763–766, 1993.

55. J. H. Comtois, V. M. Bright, and M. W. Phipps, "Thermal microactuators for surface-micromachining processes," in *Proc. SPIE*, vol. 2642, pp. 10–21, 1995.

56. W. Riethmuller and W. Benecke, "Thermally excited silicon microactuators," *IEEE Transactions on Electron Devices*, vol. 35 no.6, pp. 758–762, 1988.

57. C. M. A. Ashruf, P. J. French, C. de Boer, and P. M. Sarro, "Strain effects in multi-layers," in *Proc. SPIE*, vol. 3223, pp. 149–159, 1997.

58. S. D. Senturia, R. M. Harris, B. P. Johnson, S. Kim, K. Nabors, M. A. Shulman, and J. K. White, "A computer-aided design system for microelectromechanical systems (MEMCAD)," *IEEE J. Microelectromechanical Systems*, vol. 1, no.1, pp. 3–13, 1992.

59. G. X. Li, R. J. Gutteridge, D. N. Koury, Z. L. Zhang, and R. M. Roop, "Stress-induced warpage and the compensation in a composite micro-accelerometer," in *Proc. SPIE*, vol. 2882, pp. 147–151, 1996.

60. W. C. Young, *Roarks Formulas for Stress and Strain*, pp. 93–120, McGraw-Hill, NY, NY, 1989.

61. F. Ericson, S. Greek, J. Soderkvist, and J. Schweitz, "High sensitive internal film stress measurement by an improved micromachine indicator structure," in *Proc. Transducers '95*, pp. 84–87, 1995.

62. X. Sun, X. Gu, and W. N. Carr, "Lateral in-plane displacement microactuators with combined thermal and electrostatic drive," in *Proc. Solid-State Sensor and Actuator Workshop*, pp. 152–155, 1996.

63. T. Zhuang, A. Zhang, and L. Huang, *IC Manufacturing Technology; Principle and Practice (in Chinese)*, p. 440, Electronics Industry Press, Inc., Beijing, China, 1986.

64. C. Doring, T. Grauner, J. Marek, M. S. Mettner, H. Trah, and M. Willmann, "Micromachined thermoelectrically driven cantilever structures for fluid jet deflection," in *Proc. IEEE MEMS Workshop*, pp. 12–18, 1992.

65. W. Chu, M. Mehregany, and R. L. Mullen, "Analysis of tip deflection and force of a bimetallic cantilever microactuator," *J. Micromech. Microeng.*, vol. 3, pp. 4–7, 1993.

66. P. M. Osterberg, R. K. Gupta, J. R. Gilbert, and S. D. Senturia, "Quantitative models for the measurement of residual stress, Poisson's ratio and Young's

modulus using electrostatic pull-in of beams and diaphragms," in *Proc. Solid-State Sensor and Actuator Workshop*, pp. 184–188, 1994.

67. F. R. Morgenthaler, "Theoretical studies of microstrip antennas, vol 1: General design techniques and analysis of single and coupled elements," Tech. Rep. Federal Aviation Administration Report No. FAA-EM 79-11, U.S. Dept. of Transportation, 1979.

68. Y. Fukuta, D. Collard, T. Akiyama, E. H. Yang, and H. Fujita, "Microactuated self-assembling of 3D polysilicon structures with reshaping technology," in *Proc. IEEE MEMS Workshop*, pp. 477–481, 1997.

69. C. D. Ouwens and H. Heijingligers, "Recrystallization processes in polycrystalline silicon," *Applied Physics Letters*, vol. 26, pp. 569–571, 1975.

70. F. J. Humphreys, "Modeling mechanisms and microstructures of recrystallization," *Materials Science and Technology*, vol. 8, pp. 135–143, 1992.

71. G. Harbeke, L. Krausbauer, E. F. Steigmeier, A. E. Widmer, H. F. Kapper, and G. Neugebauer, "LPCVD polycrystalline silicon: Growth and physical propoerties of in-situ phosphorus doped and undoped films," *RCA Review*, vol. 44, pp. 287–312, June 1983.

72. M. Yoshioka, "Plastically deformed region around indentations on Si single crystal," *J. Applied Physics*, vol. 76, pp. 7790–7796, 1994.

73. S. R. Wilson, R. B. Gregory, W. M. Paulson, S. J. Krause, J. D. Gressett, A. H. Hamdi, F. D. McDaniel, and R. G. Downing, "Properties of ion-implanted polycrystalline Si layers subjected to rapid termal annealing," *Journal of Electrochemical Soc.*, vol. 132, pp. 922–929, Apr. 1983.

74. S. M. Garrison, R. C. Cammarata, C. V. Thompson, and H. I. Smith, "Surface-energy-driven grain growth during rapid thermal annealing (<10s) of thin silicon films," *Journal of Applied Physics*, vol. 61, pp. 1652–1655, Feb. 1987.

75. J. J. Grob and A. Grob, "Rapid thermal annealing-induced epitaxy of ion-implanted amorphous layers on <100> silicon," *Journal of Applied Physics*, vol. 62, pp. 1788–1791, sep 1987.

76. V. M. Bright, J. H. Comtois, D. E. Sene, J. R. Reid, S. C. Gustavson, and E. A. Watson, "Realizing micro-opto-electro-mechanical devices through a commercial surface-micromachining process," in *Proc. SPIE*, vol. 2687, pp. 34–46, 1996.

77. G. H. Hostetter, M. S. Santina, and P. D'Carpio-Montalvo, *Analytical, numerical, and computational methods for science and engineering*, ch. 9, pp. 412–477, Prentice Hall, New York, NY, 1991.

78. J. R. Rice, *Numerical methods, software and analysis*, pp. 220–230, McGraw-Hill, New York, NY, 1983.

79. ANSYS Inc., *ANSYS Theory Reference*, ch. 15.9, pp. 15.28–15.40, SAS IP, Inc., Houston, PA, 1997.

80. S. D. Senturia, "CAD for microelectromechanical systems," in *Proc. Solid State Sensors and Actuators and Eurosensors IX*, Stockholm, Sweden, pp. 21–24, 1995.

81. K. D. Mueller-Glaser, "CAD of microsystems - a challenge for systems engineering," in *Proc. European Design Automation Conference with EURO-VHDL'96 and Exhibition*, Geneva, Switzerland, pp. 280–281, 1996.

82. H. Kardestuncer, *Finite Element Handbook*, ch. 3, pp. 2.75–2.190, McGraw-Hill, NY, NY, 1987.

83. S. D. Senturia, "Microfabricated structures for the measurement of mechanical properties and adhesion of thin films," in *Proc. Transducers '87*, pp. 11–16, 1987.